Title
Tuning Sensing and Signaling in the H-NOX Family of Heme Proteins

Author
Winter, Michael B

Publication Date
2011

Peer reviewed|Thesis/dissertation

Tuning Sensing and Signaling in the H-NOX Family of Heme Proteins

By

Michael B. Winter

A dissertation submitted in partial satisfaction of the

requirements for the degree of

Doctor of Philosophy

in

Chemistry

in the

Graduate Division

of the

University of California, Berkeley

Committee in charge:

Professor Michael A. Marletta, Chair
Professor Matthew B. Francis
Professor James M. Berger

Fall 2011

Tuning Sensing and Signaling in the H-NOX Family of Heme Proteins

by Michael B. Winter

Abstract

Tuning Sensing and Signaling in the H-NOX Family of Heme Proteins

by

Michael B. Winter

Doctor of Philosophy in Chemistry

University of California, Berkeley

Professor Michael A. Marletta, Chair

Nitric oxide (NO) signaling in mammals occurs through activation of the soluble isoform of guanylate cyclase (sGC), which results in diverse physiological processes such as blood vessel dilation and neurotransmission. sGC is a heterodimeric heme protein that has evolved to be a specific sensor for NO. Although sGC contains the same histidyl-ligated porphyrin as the globins, it has no measureable affinity for oxygen (O_2) and does not oxidize in air. These unusual features facilitate selective and robust activation by NO in aerobic cellular contexts. Questions regarding the mechanism of ligand discrimination in sGC led to the identification of sGC heme domain homologues in many different organisms where these proteins function as NO and/or O_2 sensors for gas-mediated signaling pathways. The members of the protein family have been subsequently termed Heme Nitric oxide/OXygen binding (H-NOX) domains due to their divergent ligand-binding properties. Functional characterization of H-NOX domains from prokaryotes has provided important clues about the structural features that control ligand discrimination across the H-NOX family. However, additional fundamental questions remain about the influence of protein structure on heme chemistry.

Extensive studies on the globins, as model heme proteins, have established the functional importance of heme protein topological features in modulating gas diffusion to and from the heme site. In globins, deep gas pockets around the porphyrin transiently capture and release O_2, tuning O_2 affinity for transport, delivery, and storage in diverse physiological environments. Although mechanisms of gas binding in H-NOX proteins have been a subject of intense investigation, there is little knowledge regarding the functional role of protein structure in modulating gas diffusion. Using X-ray crystallography with xenon and kinetic measurements, a tunnel network that extends between the solvent and interior heme site was mapped in a prokaryotic H-NOX domain. Hindering gas diffusion through the tunnels has important consequences on diatomic gas affinity. This suggests that protein tunnels in H-NOX proteins may play functional roles in tuning gas-mediated signaling.

Unlike isolated H-NOX domains, mammalian sGC is a structurally more complex, multi-domain protein. The ability of the sGC heme to resist oxidation in air is

unique among histidyl-ligated heme proteins and essential for maximal NO-induced activation. Speculations have been made about how the sGC heme resists oxidation, but no study has systemically addressed the structural and electronic factors that contribute to this critical property. To probe the accessibility of O_2 to the heme site, we sought to substitute the native heme of sGC with an unnatural porphyrin displaying emission that is quenched by O_2. Using an expression-based methodology, a phosphorescent Ru porphyrin was incorporated in sGC constructs of varying lengths. Emission quenching results suggest that O_2 diffusion to the full-length sGC heme site is significantly hindered compared to smaller sGC constructs. Limited O_2 accessibility, combined with heme electronic factors, appear to serve as important evolutionary solutions in sGC to protect the heme cofactor under aerobic conditions.

Originally to probe sGC function, the strategies used to generate O_2-sensing proteins have been applied to create a new family of H-NOX–based molecular sensors. Substitution of the native heme in bacterial H-NOX proteins with unnatural porphyrins has proven to be a promising strategy to develop stable protein agents for biological imaging applications. Heme proteins are highly tunable frameworks that coordinate porphyrins with high fidelity and specificity. These properties have been exploited to design heme protein-based sensors with tailored functionalities for enhancing porphyrin bioavailability. Initial work on making optical O_2 sensors has evolved into recent efforts to generate H-NOX–based MRI contrast agents with high relaxivities for future use in deep-tissue imaging. Thus, through substitution of the native heme group with unnatural porphyrins, new sensing properties have been built into the H-NOX family.

TABLE OF CONTENTS

LIST OF FIGURES

LIST OF TABLES

LIST OF ABBREVIATIONS

BIS-TRIS	bis(2-hydroxyethyl)amino-tris(hydroxymethyl)methane
BLAST	basic local alignment search tool
BME	β-mercaptoethanol
CaM	calmodulin
Cat	catalase
CC	coiled-coil domain
CO	carbon monoxide
cGMP	cyclic guanosine monophosphate
Cyt	cytochrome
DEA	diethanolamine
DMF	dimethylformamide
DMSO	dimethyl sulfoxide
DPBS	Dulbecco's phosphate buffered saline
DTT	dithiothreitol
EDTA	ethylenediamine-N,N,N',N'-tetraacetic acid
eNOS	endothelial nitric oxide synthase
ESI	electrospray ionization
GdPP	gadolinium(III) protoporphyrin IX
GTP	guanosine triphosphate
Hb	hemoglobin
HEPES	4-(2-hydroxyethyl)piperazine-1-ethanesulfonic acid
H-NOX	Heme Nitric oxide/OXygen binding
ICP-OES	inductively coupled plasma-optical emission spectroscopy
iNOS	inducible nitric oxide synthase
IPTG	isopropyl β-D-1-thiogalactopyranoside
Mb	myoglobin
MnPP	manganese(III) protoporphyrin IX
MRI	magnetic resonance imaging
MS	mass spectrometry
NADPH	nicotinamide adenine dinucleotide phosphate
NHA	N-hydroxy-L-arginine
nNOS	neuronal nitric oxide synthase
NO	nitric oxide
NOS	nitric oxide synthase
Ns H-NOX	H-NOX protein from *Nostoc sp.*
NTA	nitrilotriacetic acid
O_2	oxygen

ODQ	1H-(1,2,4)oxadiazolo(4,3-a)quinoxalin-1-one
PAS	Per, Arnt, Sim domain
PCR	polymerase chain reaction
PdMP	palladium(II) mesoporphyrin IX
PDB	protein data bank
PDT	photodynamic therapy
PEG	polyethylene glycol
PET	positron emission tomography
QD	quantum dot
RMSD	root mean square deviation
ROS	reactive oxygen species
RuMP	ruthenium(II) CO mesoporphyrin IX
sGC	soluble guanylate cyclase
SHE	standard hydrogen electrode
SOD	superoxide dismutase
TEA	triethanolamine
TB	terrific broth
TFA	trifluoroacetic acid
Tof	time-of-flight
Tris	tris(hydroxymethyl)aminomethane
Tt H-NOX	H-NOX protein from *Thermoanaerobacter tengcongensis*
UV	ultraviolet
vis	visible
WT	wild-type

ACKNOWLEDGEMENTS

There are many people who deserve thanks for their guidance and support during my time at Berkeley.

First and foremost, I would like to thank my advisor Michael Marletta. I first met Michael when I was an undergraduate student in his lab visiting for the summer from Kalamazoo College. Michael gave me my first opportunity to do science in a research-focused setting and later supported me in applying to graduate school. He took a chance in me and had faith. For that, I am grateful. Captured by both the science and his personality, I joined Michael's lab as a graduate student in April 2007. I have particularly enjoyed and appreciated Michael's mentoring style over the years. Michael gives students the freedom to pursue their own research interests, which I think is critical in developing scientists who are independent thinkers. Michael has incredible instincts in tackling scientific questions, and I can only hope that some of these instincts have rubbed off on me. As I approach the next stage of my scientific career, I will apply many of the lessons I have learned from him.

I would like to thank my undergraduate advisor Regina Stevens-Truss at Kalamazoo College. Regina gave me the opportunity to work in her lab and first sparked my interest in chemistry. Without Regina, I likely would have applied to medical school, which would have been a terrible fate indeed. Regina was a constant source of support and worldly wisdom in college. She sensed an early passion in me for science, and I am very thankful for it.

I have been blessed by having numerous great mentors over the years in the Marletta lab. In particular, I would like to thank Steve Reece who always encouraged me to think about my project in new and deeper ways. I have appreciated Steve's entrepreneurial spirit, drive to "making things happen," and willingness to never be satisfied. I would like to thank Nathaniel Martin who instilled in me his attention to detail and his knowledge of chemical synthesis. Nathaniel and I shared many great conversations about life and science both outside Lewis Hall and on his back porch. I would like to thank Josh Woodward who was my mentor in the Marletta lab when I was an undergraduate student. Josh encouraged me to apply to Berkeley and taught me that it is possible to do great science without being so uptight. I would like to thank Emily Weinert for the scientific discussions in our bay and teaching me that "graduate school is a marathon, not a race." I would like to thank Emily Derbyshire for taking the time to mentor me as a young graduate student and helping me develop my project. Finally, I would like to thank Eric Underbakke for the continued discussions about sGC as well as his constant willingness to share his talents in Illustrator and in writing.

I have had many great collaborators who made the work in this dissertation possible. I would like to thank Mark Herzik in the Marletta lab for providing his talents in structural biology and being willing to help see our collaborative project to the end. I would like to thank Emily McLaurin in Dan Nocera's lab at MIT for sharing her knowledge about physical inorganic chemistry and O_2 sensing. I would like to thank Charlotte Whited in Harry Gray's lab at Caltech for providing her expertise in laser photolysis. I would like to thank Charlie Olea and Christine Phillips-Piro in the Marletta lab for also providing their talents in structural biology. Finally, I would like to thank Piper Klemm in Ken Raymond's lab at Berkeley for sharing her knowledge about MRI contrast agents as well as her business acumen.

I would also like to thank current members of the Marletta lab – Alexander Nierth, Brian Smith, Basak Surmeli, Will Beeson, Chuck Hespen, Chris Phillips, Lars Plate, and Minxi Rao – and former members of the Marletta lab – Jungjoo Yoon, Theo Agapie, Katy Barglow, Sarah Bissonnette, Loes Bevers, Nate Fernhoff, Rosalie Tran, Lily Chao, Hans Carlson, Henry Chang, Shirley Huang, Liz Boon, Mark Price, Doug Mitchell, Jacquin Niles, Kaya Erbil, Stephen Cary, and Jon Winger – in addition to those whom I have already mentioned, for the discussions, encouragement, and adventures we have shared.

Lastly, I would like to thank my parents, extended family, and friends for their continued love and support.

CHAPTER 1

INTRODUCTION

Motivation and Approach

Heme proteins are ubiquitous in biology and carry out numerous, diverse functions with the same heme cofactor. Protein-bound heme groups are involved in wide-ranging processes such as electron transfer, oxygen (O_2) activation, and stable gas binding (1-3). Heme protein frameworks are exquisitely tuned to support these essential biological roles. For example, electron transfer proteins, such as cytochrome c, supply coordinating axial heme ligands to maintain a constant redox potential (1). Enzymes, such as the P450s, provide a proximal heme ligand that stabilizes high-valent iron-oxo species for oxidative chemistry on small molecules (2). Gas-binding proteins, such as the globins, have a heme pocket architecture that modulates reversible O_2 binding for transport, delivery, and storage (3).

Although heme proteins that reversibly bind diatomic gases have been studied extensively in the context of the globins, more diverse roles of these proteins continue to be uncovered. Heme proteins with divergent folds and novel architectures have evolved to "sense" diatomic gases and mediate essential biological pathways with diverse signaling outputs. This dissertation describes work on elucidating how a recently discovered family of proteins involved in nitric oxide (NO) and O_2 signaling senses and responds to gaseous stimuli. A central focus of this work is on understanding how the structures of heme proteins modulate gas-binding properties by controlling the diffusion of diatomic gases. Strategies developed initially to study gas diffusion through heme proteins are applied to generate a new family of heme protein-based agents with applications for biological imaging. The central theme of this work takes its inspiration from Nature – heme protein structure can be used to tailor porphyrin properties for sensing in diverse biological contexts.

Chapter 1 provides historical insight into the discovery of the Heme Nitric oxide/OXygen binding (H-NOX) family of gas-sensing proteins, which are the subject of this dissertation. Initial efforts to elucidate NO signaling in mammals led to the discovery of the H-NOX family and a broader role for H-NOX–mediated signaling in biology. Following a discussion of H-NOX signaling pathways, this chapter describes our current understanding for how H-NOX proteins have evolved to selectively bind gaseous ligands. An expression-based methodology is then introduced for the incorporation of unnatural porphyrins into heme proteins. This strategy is implemented to probe the functional roles of gas diffusion through H-NOX proteins. In addition, the approach is used to build H-NOX–based molecular sensors for biological imaging.

Mammalian Nitric Oxide Signaling

Overview of mammalian NO signaling. NO is a highly reactive and toxic gas that was regarded primarily as an atmospheric pollutant until the 1980s (4). However, during that decade, NO was discovered to have important physiological roles as both a cytotoxic agent (5) and an important signaling molecule (6). NO is produced *in vivo* by the P450-type heme protein nitric oxide synthase (NOS) (7). Macrophages, as part of the innate immune system, harness the toxicity of NO via the inducible isoform of NOS (iNOS) that generates high levels of NO (μM) to combat invading microorganisms (8). NO is also used as a paracrine signaling agent in the cardiovascular and nervous systems. During paracrine signaling, the constitutively-expressed endothelial and neuronal isoforms of NOS (eNOS and nNOS, respectively) are controlled by calcium (Ca^{2+}) and calmodulin (CaM) to produce lower quantities of NO (nM) that diffuse to adjacent cells (9). There, NO targets an NO-specific heme protein receptor termed soluble guanylate cyclase (sGC) (**Figure 1.1**) (10). This tightly regulated signaling event mediates diverse physiological processes such as vasodilation and neurotransmission (9).

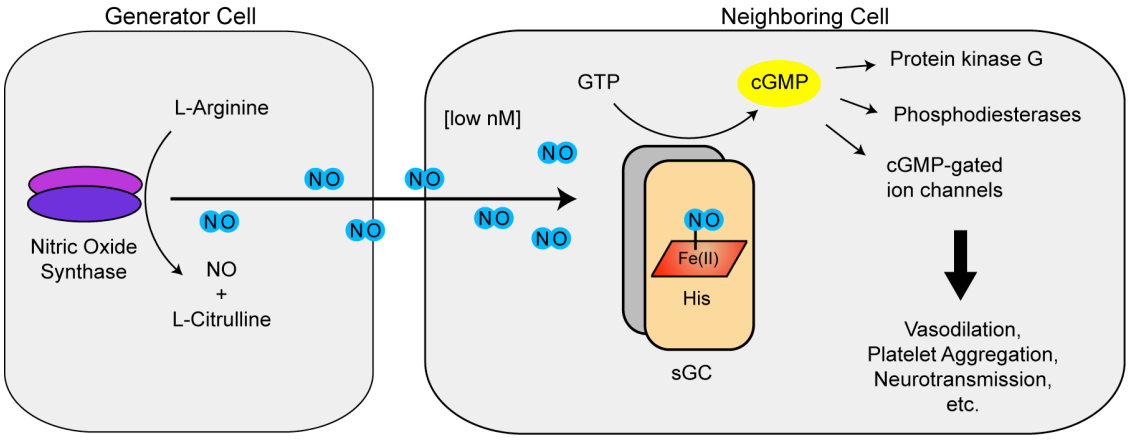

Figure 1.1 Overview of the NOS/sGC/cGMP signaling pathway in mammals (figure courtesy of E. S. Underbakke).

Mammalian NOS is a complex, multi-cofactor enzyme that produces NO from a five-electron oxidation of L-arginine, using O_2 and NADPH as co-substrates (11). Electron transfer occurs from NADPH and flavins in the reductase domain to the heme domain, where O_2 activation and substrate oxidation take place (11). Ca^{2+}-bound CaM binds to all three isoforms of NOS and is required for electron transfer between the reductase and heme domains (12, 13). The NOS-catalyzed reaction is carried out in two sequential steps – hydroxylation of L-arginine to N-hydroxy-L-arginine (NHA), followed by the three-electron oxidation of NHA to L-citrulline and NO (11). The first step is believed to occur through a P450-type oxygen rebound mechanism, whereas the second step is unprecedented in biology and is the subject of continued investigation (11, 14).

In macrophages, iNOS transcription and expression are up-regulated as part of a pro-inflammatory response induced by phagocytosis of invading gram-positive bacteria

(8). The iNOS isoform produces high levels of NO *in vivo* because it is irreversibly bound to CaM. The NO produced by iNOS reacts with O_2 and superoxide to generate reactive nitrogen and oxygen species that damage DNA, metal centers (e.g. Fe-S clusters), and proteins in the invading microorganisms (8).

During NO signaling in the vasculature, Ca^{2+} flux into the cytosol of endothelial cells stimulates the reversible binding of CaM to eNOS (9). This transient response results in the production of a lower level of NO, which then diffuses to adjacent smooth muscle cells and activates sGC (9). Activation of sGC results in smooth muscle relaxation and subsequent lowering of blood pressure (9). Dysfunction in NO signaling in the cardiovascular system leads to hypertension and atherosclerosis. Therefore, the NO signaling pathway has emerged as an important target for the treatment of cardiovascular disease (15). In neurons, NO produced by nNOS acts as a neurotransmitter where it signals vasodilation in surrounding smooth muscle cells (9). This leads to peristaltic movements in the gastrointestinal tract (16) as well as penile erection (17). Thus, NO signaling has emerged as an important target for the treatment of erectile dysfunction with the development of drugs, such as Viagra®, that inhibit downstream repressors of the pathway (18).

Activation of sGC during NO signaling results in vasodilation due to the increased production and cellular accumulation of cyclic guanosine monophosphate (cGMP). In the absence of NO, sGC exhibits a low basal activity of cGMP production (19). The binding of NO to the sGC heme cofactor increases basal activity by several hundred fold (19). The cGMP produced by sGC acts as a second messenger and directly activates protein kinase G, ion channels, and phosphodiesterases (20) (**Figure 1.1**). This process initiates interconnected, downstream signaling pathways that ultimately result in an increase in myosin phosphorylation. The phosphorylation of myosin produces smooth muscle relaxation by causing myosin to dissociate from cytoskeletal actin (21).

Molecular architecture of sGC. sGC is a heterodimeric protein that is most commonly comprised of two homologous subunits termed α1 and β1 (~600 amino acids each) (10). Although the structure of sGC has not been elucidated, it is known that heme binding occurs at the N-terminus of the β1 subunit in the conserved H-NOX domain (22). Additionally, conversion of guanosine triphosphate (GTP) to cGMP occurs at a C-terminal catalytic site composed of both subunits (**Figure 1.2**) (23). Heme binding is mediated through the coordination of the heme iron to a proximal histidine residue (β1H105) (24) as well as hydrogen bonding between the heme propionate groups and a conserved Y/S/R motif in the heme pocket (25). The residues responsible for nucleotide binding and catalysis in sGC have been identified by homology with adenylate cyclases. Two conserved aspartate residues in the sGC active site bind two Mg^{2+} ions (26, 27). One of the Mg^{2+} ions coordinates the β and γ phosphoryl groups of GTP, whereas the other Mg^{2+} ion activates its 3' hydroxyl group for the intramolecular cyclization reaction to form cGMP (26, 27).

Crystal structures have been reported for sGC domain homologues from other organisms (26-32). However, there is little understanding of how these domains are arranged to form the overall sGC quaternary structure. NO binding to the H-NOX domain of sGC results in an increase in catalytic activity. Therefore, a conformational change is predicted to be communicated between the N-terminal H-NOX domain and C-terminal catalytic site. Due to the extensive sequence space between these domains, it has been proposed that full-length sGC folds into a closed (as opposed to extended) conformation. This hypothesis has been validated recently by several biochemical approaches (23, 33, 34).

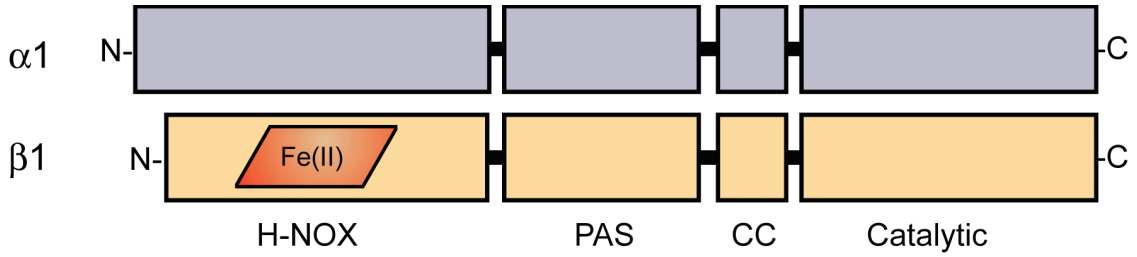

Figure 1.2 Domain architecture of the full-length sGC heterodimer. sGC contains a single Heme Nitric oxide/OXygen binding (H-NOX) domain at the N-terminus of the β1 subunit. The Per Arnt Sim (PAS), coiled-coil (CC), and catalytic domains are homologous between subunits (figure courtesy of E. S. Underbakke).

Mechanism of sGC activation. Extensive kinetic studies have provided insight into the mechanism of sGC activation. Initial spectroscopic work characterizing the binding of NO to the sGC heme indicated that NO coordinates with the ferrous (Fe^{II}) heme at a nearly diffusion-limited rate (35). This results in the formation of a transient six-coordinate complex that rapidly converts to a five-coordinate complex following dissociation of the proximal histidine ligand (**Figure 1.3**) (35). Rupture of the Fe-histidine bond in the NO-bound enzyme is the key molecular switch that converts sGC from a low activity to high activity state (35).

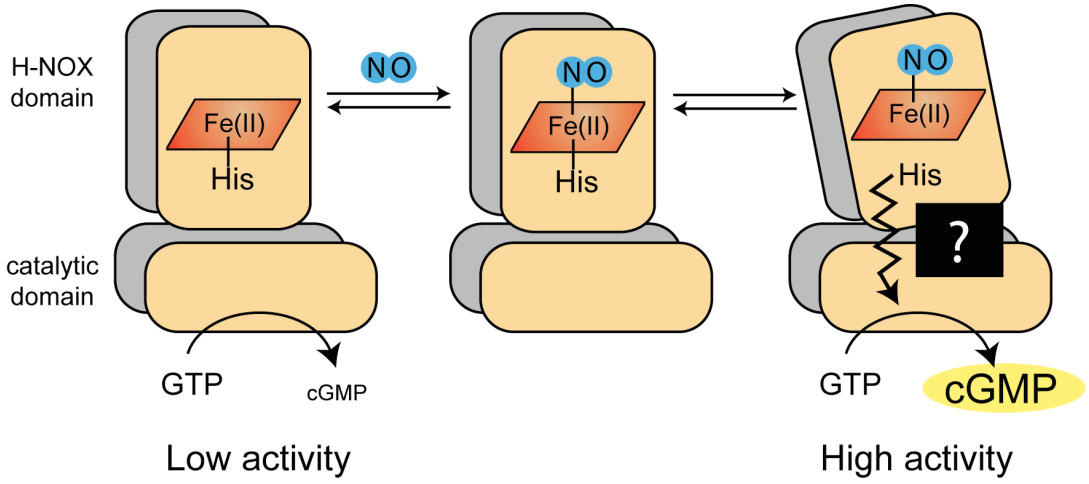

Figure 1.3 Activation mechanism of sGC by NO. (figure courtesy of E. S. Underbakke).

Early biochemical studies carried out with excess NO suggested that sGC has a binary mechanism of activation (i.e. "on" or "off"). However, more recent work has confirmed that sGC undergoes a complex three-state activation process (36, 37). One equivalent of NO binds stochiometrically and tightly (pM affinity) to the sGC heme, rupturing the Fe-histidine bond (36). This results in a partially activated form of the enzyme (~10% of the full NO-stimulated activity) (36). Full sGC activation occurs in the presence of excess NO, which is predicted to bind to non-heme site(s) (36). This effect was born out in early NO binding experiments in which the rate of iron-histidine bond cleavage demonstrated an unexpected dependence on NO concentration (35, 38).

Efforts to identify the molecular basis for this "excess NO" effect in sGC have suggested that NO undergoes an addition reaction with cysteine residue(s) in the protein (39). NO commonly reacts with protein thiols in an oxidative addition termed S-nitrosation (RSNO). However, sGC activation by NO was found to proceed without electron transfer and independently of RSNO formation (39). A direct addition complex (e.g., RS–NO^-) has been proposed to be the key activating species, although this or similar complexes have yet to be observed directly (39). Identification of the site(s) of NO addition has been an analytical challenge because sGC has 34 cysteine residues, and pure, recombinantly-expressed sGC cannot be generated in large amounts (39). The proposed addition complex exhibits a short half-life (seconds) compared to the five-coordinate heme complex (minutes) (36, 40). This provides rapid temporal control for acute sGC activation (36).

NO-specific sensing in sGC. sGC has the remarkable ability to selectively bind NO with no measurable affinity for O_2 even though the protein has the same histidyl-ligated porphyrin as the globins (10, 41). This specificity is critical *in vivo* because O_2 is present at ~1000-fold higher concentrations than signaling amounts of NO (nM vs. μM) (41). The ability of sGC to discriminate against O_2 binding at the heme eliminates direct competition between NO and O_2. Additionally, this discrimination prevents NO dioxygenation chemistry that commonly occurs in the globins as a result of NO combining with the heme Fe^{II}–O_2 complex (42). The NO dioxygenation reaction results in the production of ferric heme (42), which in sGC weakly binds NO but is not fully activated (43). In addition to rigorously excluding O_2 binding, sGC is unique among histidyl-ligated heme proteins because it exhibits no measurable oxidation in air (19, 44). Protection of the ferrous heme ensures full activity in aerobic cellular environments. However, under conditions of oxidative stress, the sGC heme could become oxidized. Ferric sGC is implicated in cardiovascular disease and tolerance to therapy involving NO donors (15, 45-47). Therefore, the oxidized enzyme has emerged as a promising drug target (15, 45-47).

Discovery of the H-NOX Family of Heme Proteins

Overview of H-NOX proteins. Interest in elucidating the molecular basis for ligand discrimination in mammalian sGC led to an effort to define the minimal heme-

binding region of the protein for ease of biochemical study. The N-terminal fragment of the sGC β1 subunit (residues 1-194) was found to stably bind heme and have identical ligand-binding properties to the full-length enzyme (22). A BLAST search performed on this heme-binding region identified heme domain homologues in many different organisms (48). These homologues were found in prokaryotes, either fused or adjacent to signaling proteins, as well as eukaryotes, such as *Caenorhabditis elegans* and *Drosophila melanogaster*, as a domain in novel soluble guanylate cyclases (48-50). In prokaryotes, the heme domains were identified both in obligate anaerobes where they were fused to methyl-accepting chemotaxis proteins as well as in facultative anaerobes where they were located in the same operon as histidine kinases and diguanylate cyclases (48, 51, 52). *In vivo* functional studies have confirmed that the H-NOX protein family plays a broad role in diverse gas-mediated signaling pathways (49, 52, 53).

Ligand discrimination in H-NOX proteins. Early biochemical characterization of the heme domain homologues from prokaryotes indicated that they have divergent ligand-binding properties (48). The heme domains from facultative anaerobes displayed selectivity similar to sGC, whereas those from obligate anaerobes were found to bind both NO and O_2 like the globins (48). The protein family subsequently was termed H-NOX (Heme Nitric oxide/OXygen binding) domains to encompass its diverse gas-binding properties (48). To identify a molecular basis for O_2 binding in the H-NOX family, a crystal structure was solved of the H-NOX domain from *Thermoanaerobacter tengcongensis* (*Tt* H-NOX) bound to O_2 (**Figure 1.4**) (29). The structure showed that the protein has a network of hydrogen-bonding residues distal to the heme. In the crystal structure, a tyrosine residue (Y140) appeared to provide the principle H-bonding interaction with the O_2 ligand (**Figure 1.4**). Multiple sequence alignments indicated that non-O_2-binding H-NOX proteins have a nonpolar residue at the homologous position, suggesting that the presence of a distal pocket tyrosine could be a key molecular

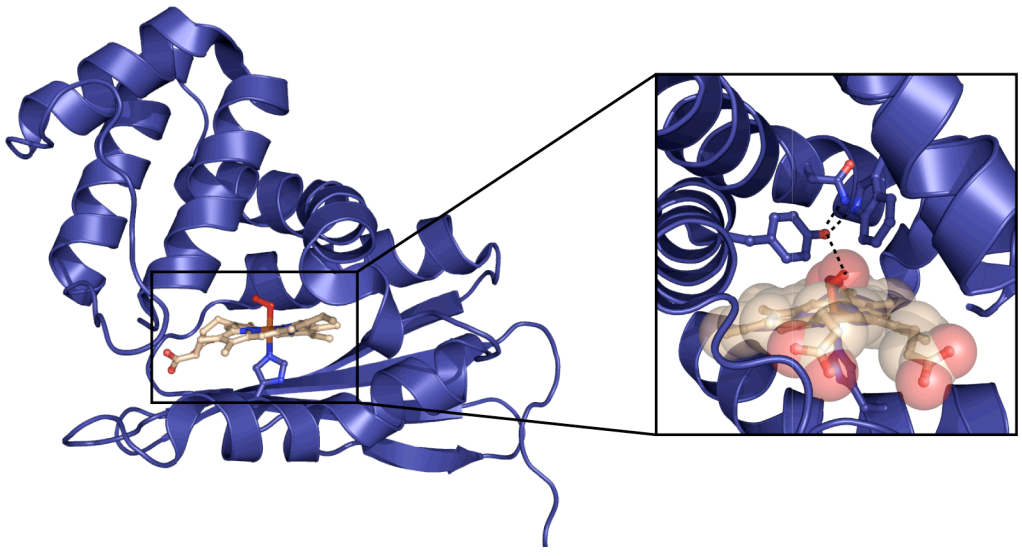

Figure 1.4 Crystal structure of Fe^{II}–O_2 *Tt* H-NOX at 1.77 Å resolution (PDB 1U55, molecule A). **(Inset)** *Tt* H-NOX heme site with H-bonding interactions shown. Y140, N74, and W9 residues as well as the H102 and O_2 heme ligands are represented in ball and stick.

determinant for O_2 binding (54). To test the influence of H-bonding residues on O_2 affinity, a structure-guided mutagenesis study was conducted (54). In line with the prediction, replacement of the H-bonding network in *Tt* H-NOX with nonpolar residues eliminated O_2 binding, whereas introduction of a tyrosine residue at the conserved position was sufficient to confer O_2 binding in an NO-selective H-NOX domain (54). Kinetics analysis indicated that the conserved tyrosine stabilizes O_2 at the heme principally through slowing the rate of O_2 dissociation (54).

Engineering O_2 binding in sGC. The presence of a distal pocket tyrosine has proven to be a reliable predictor for O_2 binding in the H-NOX family. However, efforts to convert sGC into a protein that stably binds O_2 have suggested that the complete mechanism for ligand discrimination is likely more complex (55). Although introduction of a tyrosine residue to the conserved position (I145Y) in an H-NOX–containing sGC construct resulted in the formation of a weak O_2 complex (54), the tyrosine mutation had no effect on O_2 binding in the full-length enzyme (55). Recently, incorporation of a potential H-bonding network (I145Y/I149Q) in sGC was found to result in apparent O_2 binding (56). However, complex formation was transient and associated with rapid heme oxidation (56). Taken together, these studies suggest that numerous structural and electronic features are responsible for modulating ligand binding in the H-NOX family.

Tuning H-NOX ligand binding. Recent structure-guided mutagenesis studies on *Tt* H-NOX have provided significant insight into the influence of additional heme pocket structural features on ligand binding. One of the most striking aspects of the *Tt* H-NOX crystal structure is the highly distorted porphyrin (**Figure 1.4**) (29). In *Tt* H-NOX, the heme is in van der Waals contact with a conserved proline residue (P115) that appears to contribute to heme distortion (29). Mutagenesis of the proline to an alanine resulted in a significantly more planar porphyrin in the crystal structure of the P115A mutant (57). This protein had a dramatically decreased reduction potential (-4 vs 167 mV) and increased O_2 affinity (21 nM vs 90 nM) without appreciable changes to the heme pocket environment (57). This suggested that heme conformation may play a broad role in modulating ligand affinity in H-NOX proteins.

In addition to porphyrin distortion, significant efforts have been carried out to probe the role of heme pocket steric bulk on *Tt* H-NOX O_2-binding properties. Phenylalanine residues have been introduced individually and in combinations in place of smaller nonpolar residues at numerous positions around the heme (58, 59). In crystal structures of these *Tt* H-NOX variants, the protein is in an extended conformation, presumably due to steric strain imparted by the introduction of bulky residues in the relatively constricted heme pocket (58, 59). These mutations were found to increase O_2 association and dissociation rates, resulting in a net weakening of O_2 affinity (58, 59). The changes are consistent with a more solvent-exposed heme site and weakened H-bonding interactions. Together these data highlight the importance of the global H-NOX conformation in controlling ligand-binding kinetics.

Modifying Heme Protein Properties with Porphyrin Substitution

Functional studies examining ligand binding in the H-NOX family point to the powerful role of structure-guided mutagenesis in probing heme protein properties. However, amino acid substitution provides a limited repertoire of chemical functionality. In heme proteins, synthetic porphyrins with tailored chemical properties can be introduced in place of the native heme cofactor. This strategy allows for new avenues of experimentation by introducing diverse and novel chemical functionality at the heme site.

In spite of the utility of this approach, porphyrin substitution is an under-utilized strategy for probing heme protein function. Traditional methods for the incorporation of unnatural porphyrins into heme proteins rely on harsh, denaturing conditions to remove the native heme (60). This has greatly diminished the number of viable protein constructs. To address this issue, an expression-based method for porphyrin substitution has been developed by our laboratory in which incorporation of the unnatural porphyrin occurs under biological conditions (61) (**Figure 1.5**). The approach employs the RP523 strain of *Escherichia coli* to facilitate porphyrin uptake and limit native heme incorporation (61). The RP523 strain is a heme auxotroph (due to deletion of the hemB gene) and has an uncharacterized mutation rendering it porphyrin-permeable (61). Initial efforts to incorporate unnatural porphyrins into diverse heme proteins suggested that the expression-based approach is viable strategy for porphyrin substitution that preserves the native protein structure (61). However, this methodology represents a largely untapped resource for studying heme protein properties.

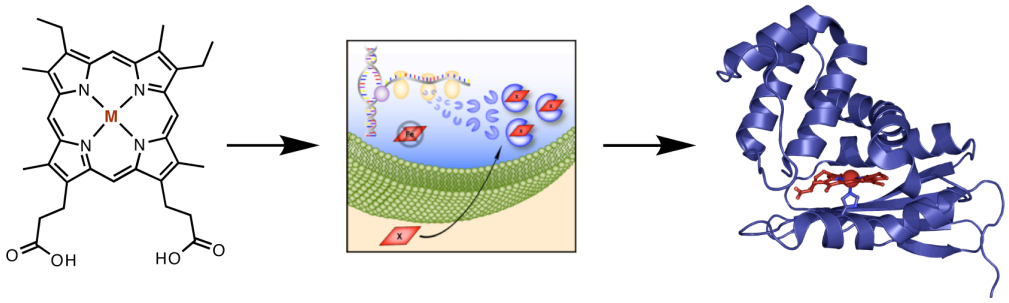

Figure 1.5 Expression-based method for unnatural porphyrin incorporation into heme proteins using the RP523 *E. coli* strain (central panel adapted from J. J. Woodward).

Focus of This Research

Previous efforts to examine the structural features that modulate ligand binding in H-NOX proteins have focused largely on the influence of heme pocket architecture. However, architectural features outside the heme site can have important consequences on heme chemistry. In this dissertation, the functional influence of H-NOX structure on the diffusion of gaseous ligands is tested in the H-NOX family. Initially, X-ray crystallography with xenon is used to map discrete pathways for ligand diffusion in an H-NOX domain (**Chapter 2**). Structure-guided mutagenesis is then employed to hinder gas diffusion through these pathways and establish their functional role in modulating heme ligand-binding kinetics (**Chapter 2**). The revelation that H-NOX structure controls gas migration inspired an investigation into the functional role of higher-order domain

architecture in tuning the unusual heme properties of sGC. As discussed, sGC is unique among histidyl-ligated heme proteins because it does not oxidize in air, which facilitates full NO activation in aerobic conditions. To provide a structural basis for this finding, we sought to measure O_2 diffusion near the sGC heme site by incorporating a synthetic porphyrin that can detect O_2 via emission quenching. To our initial surprise, preliminary studies to test this methodology in a prokaryotic H-NOX domain suggested that the protein has promising properties for biological O_2-sensing applications. The development and evaluation of a new class of H-NOX–based O_2 sensors is discussed (**Chapter 3**) prior to using porphyrin substitution to probe O_2 diffusion in sGC (**Chapter 4**). The promising features of the H-NOX–based optical agents evolved into an interest to improve their properties for biological sensing through the incorporation of new synthetic porphyrins that support other imaging strategies. **Chapter 5** reports recent progress in developing H-NOX–based contrast agents for magnetic resonance imaging (MRI) technology.

References

1. Battistuzzi G, Borsari M, Cowan JA, Ranieri A, & Sola M (2002) Control of cytochrome C redox potential: axial ligation and protein environment effects. *J Am Chem Soc* 124: 5315-5324.
2. Meunier B, de Visser SP, & Shaik S (2004) Mechanism of oxidation reactions catalyzed by cytochrome p450 enzymes. *Chem Rev* 104: 3947-3980.
3. Olson JS & Phillips GN (1997) Myoglobin discriminates between O_2, NO, and CO by electrostatic interactions with the bound ligand. *J Inorg Biochem* 2: 544-552.
4. Buchan WE & Charlson RJ (1968) Urban haze: the extent of automotive contribution. *Science* 159: 192-194.
5. Marletta MA, Yoon PS, Iyengar R, Leaf CD, & Wishnok JS (1988) Macrophage oxidation of L-arginine to nitrite and nitrate: nitric oxide is an intermediate. *Biochemistry* 27: 8706-8711.
6. Palmer RM, Ashton DS, & Moncada S (1988) Vascular endothelial cells synthesize nitric oxide from L-arginine. *Nature* 333: 664-666.
7. White KA & Marletta MA (1992) Nitric oxide synthase is a cytochrome P-450 type hemoprotein. *Biochemistry* 31: 6627-6631.
8. MacMicking J, Xie QW, & Nathan C (1997) Nitric oxide and macrophage function. *Annu Rev Immunol* 15: 323-350.
9. Moncada S, Palmer RM, & Higgs EA (1991) Nitric oxide: physiology, pathophysiology, and pharmacology. *Pharmacol Rev* 43: 109-142.
10. Derbyshire ER & Marletta MA (2009) Biochemistry of soluble guanylate cyclase. *Handb Exp Pharmacol*: 17-31.
11. Marletta MA, Hurshman AR, & Rusche KM (1998) Catalysis by nitric oxide synthase. *Curr Opin Chem Biol* 2: 656-663.
12. Gribovskaja I, Brownlow KC, Dennis SJ, Rosko AJ, Marletta MA, & Stevens-Truss R (2005) Calcium-binding sites of calmodulin and electron transfer by inducible nitric oxide synthase. *Biochemistry* 44: 7593-7601.

13. Stevens-Truss R, Beckingham K, & Marletta MA (1997) Calcium binding sites of calmodulin and electron transfer by neuronal nitric oxide synthase. *Biochemistry* 36: 12337-12345.
14. Woodward JJ, Chang MM, Martin NI, & Marletta MA (2009) The second step of the nitric oxide synthase reaction: evidence for ferric-peroxo as the active oxidant. *J Am Chem Soc* 131: 297-305.
15. Stasch JP, Pacher P, & Evgenov OV (2011) Soluble guanylate cyclase as an emerging therapeutic target in cardiopulmonary disease. *Circulation* 123: 2263-2273.
16. Stark ME & Szurszewski JH (1992) Role of nitric oxide in gastrointestinal and hepatic function and disease. *Gastroenterology* 103: 1928-1949.
17. Burnett AL, Lowenstein CJ, Bredt DS, Chang TS, & Snyder SH (1992) Nitric oxide: a physiologic mediator of penile erection. *Science* 257: 401-403.
18. Dorsey P, Keel C, Klavens M, & Hellstrom WJ (2010) Phosphodiesterase type 5 (PDE5) inhibitors for the treatment of erectile dysfunction. *Expert Opin Pharmacother* 11: 1109-1122.
19. Stone JR & Marletta MA (1994) Soluble guanylate cyclase from bovine lung: activation with nitric oxide and carbon monoxide and spectral characterization of the ferrous and ferric states. *Biochemistry* 33: 5636-5640.
20. Ignarro LJ, Cirino G, Casini A, & Napoli C (1999) Nitric oxide as a signaling molecule in the vascular system: an overview. *J Cardiovasc Pharmacol* 34: 879-886.
21. Somlyo AP & Somlyo AV (1994) Signal transduction and regulation in smooth muscle. *Nature* 372: 231-236.
22. Karow DS, Pan D, Davis JH, Behrends S, Mathies RA, & Marletta MA (2005) Characterization of functional heme domains from soluble guanylate cyclase. *Biochemistry* 44: 16266-16274.
23. Winger JA & Marletta MA (2005) Expression and characterization of the catalytic domains of soluble guanylate cyclase: interaction with the heme domain. *Biochemistry* 44: 4083-4090.
24. Zhao Y, Schelvis JP, Babcock GT, & Marletta MA (1998) Identification of histidine 105 in the beta1 subunit of soluble guanylate cyclase as the heme proximal ligand. *Biochemistry* 37: 4502-4509.
25. Schmidt PM, Schramm M, Schroder H, Wunder F, & Stasch JP (2004) Identification of residues crucially involved in the binding of the heme moiety of soluble guanylate cyclase. *J Biol Chem* 279: 3025-3032.
26. Winger JA, Derbyshire ER, Lamers MH, Marletta MA, & Kuriyan J (2008) The crystal structure of the catalytic domain of a eukaryotic guanylate cyclase. *BMC Struct Biol* 8: 42.
27. Rauch A, Leipelt M, Russwurm M, & Steegborn C (2008) Crystal structure of the guanylyl cyclase Cya2. *Proc Natl Acad Sci U S A* 105: 15720-15725.
28. Ma X, Sayed N, Baskaran P, Beuve A, & van den Akker F (2008) PAS-mediated dimerization of soluble guanylyl cyclase revealed by signal transduction histidine kinase domain crystal structure. *J Biol Chem* 283: 1167-1178.

29. Pellicena P, Karow DS, Boon EM, Marletta MA, & Kuriyan J (2004) Crystal structure of an oxygen-binding heme domain related to soluble guanylate cyclases. *Proc Natl Acad Sci U S A* 101: 12854-12859.
30. Ma X, Beuve A, & van den Akker F (2010) Crystal structure of the signaling helix coiled-coil domain of the beta1 subunit of the soluble guanylyl cyclase. *BMC Struct Biol* 10: 2.
31. Ma X, Sayed N, Beuve A, & van den Akker F (2007) NO and CO differentially activate soluble guanylyl cyclase via a heme pivot-bend mechanism. *EMBO J* 26: 578-588.
32. Erbil WK, Price MS, Wemmer DE, & Marletta MA (2009) A structural basis for H-NOX signaling in *Shewanella oneidensis* by trapping a histidine kinase inhibitory conformation. *Proc Natl Acad Sci U S A* 106: 19753-19760.
33. Haase T, Haase N, Kraehling JR, & Behrends S (2010) Fluorescent fusion proteins of soluble guanylyl cyclase indicate proximity of the heme nitric oxide domain and catalytic domain. *PLoS One* 5: e11617.
34. Underbakke E (2011) Unpublished results.
35. Zhao Y, Brandish PE, Ballou DP, & Marletta MA (1999) A molecular basis for nitric oxide sensing by soluble guanylate cyclase. *Proc Natl Acad Sci U S A* 96: 14753-14758.
36. Cary SP, Winger JA, & Marletta MA (2005) Tonic and acute nitric oxide signaling through soluble guanylate cyclase is mediated by nonheme nitric oxide, ATP, and GTP. *Proc Natl Acad Sci U S A* 102: 13064-13069.
37. Russwurm M & Koesling D (2004) NO activation of guanylyl cyclase. *EMBO J* 23: 4443-4450.
38. Ballou DP, Zhao Y, Brandish PE, & Marletta MA (2002) Revisiting the kinetics of nitric oxide (NO) binding to soluble guanylate cyclase: the simple NO-binding model is incorrect. *Proc Natl Acad Sci U S A* 99: 12097-12101.
39. Fernhoff NB, Derbyshire ER, & Marletta MA (2009) A nitric oxide/cysteine interaction mediates the activation of soluble guanylate cyclase. *Proc Natl Acad Sci U S A* 106: 21602-21607.
40. Winger JA, Derbyshire ER, & Marletta MA (2007) Dissociation of nitric oxide from soluble guanylate cyclase and heme-nitric oxide/oxygen binding domain constructs. *J Biol Chem* 282: 897-907.
41. Boon EM & Marletta MA (2005) Ligand specificity of H-NOX domains: from sGC to bacterial NO sensors. *J Inorg Biochem* 99: 892-902.
42. Gardner PR, Gardner AM, Brashear WT, Suzuki T, Hvitved AN, Setchell KD, & Olson JS (2006) Hemoglobins dioxygenate nitric oxide with high fidelity. *J Inorg Biochem* 100: 542-550.
43. Zhao Y, Brandish PE, DiValentin M, Schelvis JP, Babcock GT, & Marletta MA (2000) Inhibition of soluble guanylate cyclase by ODQ. *Biochemistry* 39: 10848-10854.
44. Derbyshire ER, Winter MB, Ibrahim M, Deng S, Spiro TG, & Marletta MA (2011) Probing domain interactions in soluble guanylate cyclase. *Biochemistry* 50: 4281-4290.

45. Priviero FB & Webb RC (2010) Heme-dependent and independent soluble guanylate cyclase activators and vasodilation. *J Cardiovasc Pharmacol* 56: 229-233.
46. Gladwin MT (2006) Deconstructing endothelial dysfunction: soluble guanylyl cyclase oxidation and the NO resistance syndrome. *J Clin Invest* 116: 2330-2332.
47. Evgenov OV, Pacher P, Schmidt PM, Hasko G, Schmidt HH, & Stasch JP (2006) NO-independent stimulators and activators of soluble guanylate cyclase: discovery and therapeutic potential. *Nat Rev Drug Discov* 5: 755-768.
48. Karow DS, Pan D, Tran R, Pellicena P, Presley A, Mathies RA, & Marletta MA (2004) Spectroscopic characterization of the soluble guanylate cyclase-like heme domains from *Vibrio cholerae* and *Thermoanaerobacter tengcongensis*. *Biochemistry* 43: 10203-10211.
49. Gray JM, Karow DS, Lu H, Chang AJ, Chang JS, Ellis RE, Marletta MA, & Bargmann CI (2004) Oxygen sensation and social feeding mediated by a C. elegans guanylate cyclase homologue. *Nature* 430: 317-322.
50. Huang SH, Rio DC, & Marletta MA (2007) Ligand binding and inhibition of an oxygen-sensitive soluble guanylate cyclase, Gyc-88E, from *Drosophila*. *Biochemistry* 46: 15115-15122.
51. Price MS, Chao LY, & Marletta MA (2007) *Shewanella oneidensis* MR-1 H-NOX regulation of a histidine kinase by nitric oxide. *Biochemistry* 46: 13677-13683.
52. Carlson HK, Vance RE, & Marletta MA (2010) H-NOX regulation of c-di-GMP metabolism and biofilm formation in *Legionella pneumophila*. *Mol Microbiol*.
53. Wang Y, Dufour YS, Carlson HK, Donohue TJ, Marletta MA, & Ruby EG (2010) H-NOX-mediated nitric oxide sensing modulates symbiotic colonization by *Vibrio fischeri*. *Proc Natl Acad Sci U S A* 107: 8375-8380.
54. Boon EM, Huang SH, & Marletta MA (2005) A molecular basis for NO selectivity in soluble guanylate cyclase. *Nat Chem Biol* 1: 53-59.
55. Martin E, Berka V, Bogatenkova E, Murad F, & Tsai AL (2006) Ligand selectivity of soluble guanylyl cyclase: effect of the hydrogen-bonding tyrosine in the distal heme pocket on binding of oxygen, nitric oxide, and carbon monoxide. *J Biol Chem* 281: 27836-27845.
56. Derbyshire ER, Deng S, & Marletta MA (2010) Incorporation of tyrosine and glutamine residues into the soluble guanylate cyclase heme distal pocket alters NO and O_2 binding. *J Biol Chem* 285: 17471-17478.
57. Olea C, Boon EM, Pellicena P, Kuriyan J, & Marletta MA (2008) Probing the function of heme distortion in the H-NOX family. *ACS Chem Biol* 3: 703-710.
58. Weinert EE, Plate L, Whited CA, Olea C, Jr., & Marletta MA (2010) Determinants of ligand affinity and heme reactivity in H-NOX domains. *Angew Chem Int Ed Engl* 49: 720-723.
59. Weinert EE, Phillips-Piro CM, Tran R, Mathies RA, & Marletta MA (2011) Controlling conformational flexibility of an O_2-binding H-NOX domain. *Biochemistry* 50: 6832-6840.
60. Teale F (1959) Cleavage of the haem-protein link by acid methylethylketone. *Biochim Biophys Acta* 35: 543.

61. Woodward JJ, Martin NI, & Marletta MA (2007) An *Escherichia coli* expression-based method for heme substitution. *Nat Methods* 4: 43-45.

CHAPTER 2

A TUNNEL NETWORK MODULATES LIGAND FLUX IN A PROKARYOTIC H-NOX DOMAIN*

Summary

In this chapter, a tunnel network in an H-NOX protein is found to serve as a molecular pathway for ligand diffusion between the solvent and interior heme site. X-ray crystallography with xenon is used to map the tunnel network, and structure-guided mutants, in combination with kinetic measurements, provide a functional understanding of how hindering diffusion through the tunnels modulates heme ligand-binding properties. Together, the data suggest that H-NOX proteins have discrete ligand migration pathways that are functionally important for tuning gas-mediated signaling.

Introduction

Protein scaffolds are exquisitely tuned to carry out essential processes in biology. The structures of enzyme active sites, for example, have evolved to both catalyze and lend specificity to numerous chemical transformations. In addition to structural features that directly participate in active site chemistry, proteins often have interior cavities that provide spatial and temporal regulation. These structural features guide small molecule entry and exit as well as link intermediates between reactive centers. For example, channels for gas transport have been identified in enzymes utilizing O_2 (e.g. oxidases and oxygenases) (1, 2), N_2 (nitrogenases) (3), and H_2 (hydrogenases) (4) for critical biological redox reactions. In enzymes with multiple active sites, tunnel networks shunt oftentimes volatile or reactive intermediates between reactive centers for processes such as bacterial carbon fixation (5) and the biosynthesis of essential cofactors (6) and amino acids (7, 8).

Interior structural features have evolved in heme proteins to facilitate diverse types of chemistry with an identical heme cofactor. Historically, globins have served as a model system for understanding how ligand flux through heme protein scaffolds controls gas-binding properties. Over the past 50 years, studies on myoglobin have utilized X-ray crystallography (9), time-resolved absorption techniques (10), CO photolysis of protein crystals (11, 12), and computational methods (13, 14) to provide a detailed molecular picture of ligand migration through the globin fold. Experimental approaches have implicated a histidine residue, the "His(E7) gate" (15), as the primary route for ligand

*The worked described in this chapter was done in collaboration with Mark A. Herzik, Jr. in Prof. Michael A. Marletta's laboratory (UC Berkeley) and Prof. John Kuriyan (UC Berkeley). M.A.H. collected diffraction data and solved the crystal structures. This work led to the following publication: Winter MB, Herzik MA, Jr., Kuriyan J, & Marletta MA (2011) Tunnels Modulate Ligand Flux in a Heme Nitric Oxide/Oxygen Binding (H-NOX) Domain. *Proc Natl Acad Sci USA* 108: 17577-17578, E881-E889.

entry and exit, in contrast to computational studies which have identified multiple ligand migration pathways (14). Internal cavities around the porphyrin in globins transiently hold O_2 as it migrates to and from the heme iron. These structural features work in concert with residues directly involved in ligand coordination to efficiently capture and release O_2 for gas transport, storage, and delivery in desired physiological contexts (16, 17).

Recent structural studies conducted on non-canonical globins have greatly expanded our knowledge of how globins function (18-23). Alternate topological features such as interior gas tunnels in truncated hemoglobins, for example, have been shown to be mechanistically important for modulating ligand migration (18, 19). However, further studies are needed to fully understand how these related protein frameworks within the globin family contribute to variations in ligand-binding properties. In addition, little is known about how ligand diffusion affects reversible gas binding within a broader spectrum of heme proteins.

H-NOX (Heme Nitric oxide / OXygen binding) domains are a newly discovered family of gas-sensing heme proteins with a novel fold found in organisms from bacteria to humans (24). The best characterized H-NOX-containing protein is soluble guanylate cyclase (sGC), which is the principle mammalian receptor for NO and a central regulator of NO/cGMP-dependant signaling pathways (24). Members of the H-NOX family exhibit divergent ligand-binding properties within the identical protein fold. Some H-NOX domains bind NO, O_2, and CO like the globins, whereas others (including sGC) discriminate against O_2 binding, allowing them to serve as specific NO sensors even under aerobic conditions (24). The presence of a distal pocket tyrosine residue has been shown to be important for stabilizing O_2 binding in the H-NOX family (25). However, it is apparent that additional structural and electronic features contribute to ligand binding properties (25-30).

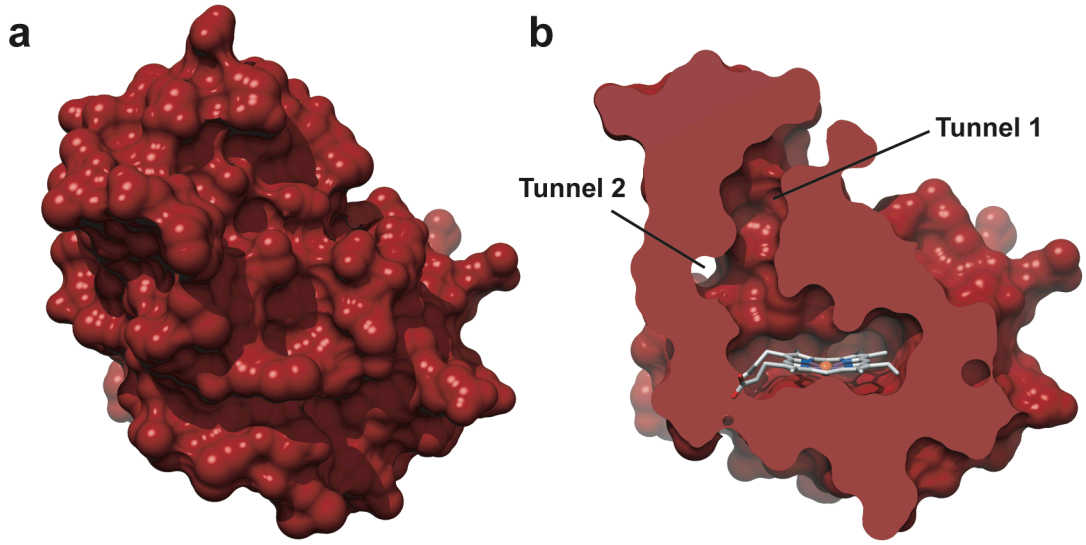

Figure 2.1 Surface representations of WT *Ns* H-NOX depicting **(a)** the protein exterior and **(b)** a cross-sectional view where putative channels between the solvent and heme pocket are evident.

Surface representations of available H-NOX crystal structures (31, 32) indicate that unlike globins, the heme in H-NOX domains is completely buried within the protein matrix (**Figure 2.1A**). Close inspection of a non-O_2-binding H-NOX domain, however, reveals a putative tunnel network (**Figure 2.1B**) that extends between the solvent and interior heme site (33). This tunnel network is comprised of shorter (~15 Å) and longer (~22 Å) branches that are lined by well-conserved, hydrophobic residues and appear to be void of ordered solvent molecules (32). This indicates that the apparent tunnels may serve as potential conduits for gas diffusion. The tunnels are not evident in O_2-binding H-NOX domains, suggesting that differential ligand flux through H-NOX scaffolds could be important for divergent functions (33).

In the present study, direct experimental evidence is provided for the existence of a tunnel network in H-NOX proteins. High-resolution crystal structures were obtained of the non-O_2-binding H-NOX domain from *Nostoc sp*. (*Ns* H-NOX) (32) pressurized with xenon, establishing a molecular route for ligand diffusion between the solvent and heme site. Structure-guided mutagenesis in combination with time-resolved absorption techniques were employed to probe the functional role of the tunnel network in modulating ligand-binding kinetics at the heme. Together, the data has led to an unexpected mechanism for how ligand diffusion regulates ligand-binding properties in the H-NOX family – marking the first time that the effect of tunnels on reversible gas binding has been elucidated in a non-globin fold. This work provides fundamental insights into the functional role of protein scaffolds in controlling the flux of biological molecules.

Experimental Procedures

Plasmids for protein expression. The gene for *Ns* H-NOX (residues 1-189) from *Nostoc sp* PCC 7120 (32) was purchased codon-optimized in the pUC vector from GenScript. The gene was PCR amplified and cloned into the pCW plasmid. DNA primers for PCR amplification and site-directed mutagenesis were synthesized by Integrated DNA Technologies. Sequencing of all *Ns* H-NOX variants was carried out by Elim Biopharmaceuticals, Inc. The gene for untagged *Tt* H-NOX (residues 1-188 of *Tt*Tar4H from *Thermoanaerobacter tengcongensis*) (44) and the construct with a C-terminal His_6 tag (26) were used as described previously.

Protein expression. *Ns* H-NOX constructs were transformed into the RP523 strain of *E. coli* (45). Expression cultures were grown at 37 °C in TB media in the presence of 30 μg/mL hemin (~200X stock in DMSO) and 75-100 μg/mL ampicillin. Expression was induced with 1 mM IPTG, and induction was allowed to occur for 18-22 h at room temperature. *Tt* H-NOX constructs were expressed as described previously (26).

Protein purification. All *Ns* H-NOX variants were purified using anion exchange chromatography followed by size-exclusion chromatography. Proteins were isolated in the Fe^{II}–unligated state (Soret maxima of 429-430 nm). *Tt* H-NOX constructs were

purified as described previously (26) (45) and isolated in the Fe^{II}–O_2 ligation state (Soret maximum of ~416 nm).

For all *Ns* H-NOX variants, cell pellets (from 1-2 L of *E. coli* expression) were slowly thawed on ice and re-suspended in ~100 mL of buffer A (50 mM DEA, pH 8.5, 25 mM NaCl, 5% glycerol, 5 mM DTT, 1 mM benzamidine hydrochloride), which also contained 1 mM Pefabloc. The resuspended cells were lysed 3 times with an EmulsiFlex-C5 homogenizer (Avestin, Inc.) at 4 °C between 5,000 and 15,000 psi. The lysate underwent centrifugation with an Optima XL-100K ultracentrifuge (Beckman Coulter, Inc.) for 1 h at 42,000 rpm. The supernatant was applied at 1.2-1.5 mL/min to a Toyopearl SuperQ-650M anion exchange column (Tosoh Bioscience GmbH) that had been equilibrated with buffer A. The protein was eluted with a NaCl gradient from 0% to 100% buffer B (50 mM DEA, pH 8.5, 500 mM NaCl, 5% glycerol, 5 mM DTT) over 800 mL at 1.2-1.5 mL/min while 5 mL fractions were collected. Fractions containing *Ns* H-NOX were pooled and concentrated to less than 3 mL using a 5,000 or 10,000 MWCO spin concentrator. Finally, the concentrated protein underwent size-exclusion chromatography with a HiLoad 16/60 Superdex 75 column (GE Healthcare) that had been equilibrated with buffer C (50 mM TEA, pH 7.5, 150 mM NaCl, 5% glycerol, 5 mM DTT). The protein was separated with an isocratic flow of buffer C at 1 mL/min while 2 mL fractions were collected. Fractions containing the highest purity *Ns* H-NOX were pooled and concentrated with a 5,000 or 10,000 MWCO spin concentrator. Purity was estimated to be >90% by Coomassie stain following SDS-PAGE.

UV–visible spectral characterization. Heme-ligand complexes were generated as described previously using established methods (44). Briefly, UV–visible spectra of various *Ns* H-NOX heme-ligand complexes were acquired in buffer D (50 mM HEPES, 7.4, 50 mM NaCl) at room temperature on a Cary 3E spectrophotometer. Briefly, proteins were fully reduced with ~10 mM dithionite in an anaerobic chamber (Coy) for 5 min at room temperature. Dithionite was subsequently removed using a PD10 column (GE Healthcare). All spectra were acquired under anaerobic conditions in a septum-sealed 1 cm pathlength quartz cuvette. Fe^{II}–CO complexes were generated by sparging the headspace of a cuvette containing ferrous protein with CO (99.99%; Praxair, Inc.) for 5 min. Fe^{II}–NO complexes were generated by adding 4 μM DEA NONOate (Caymen Chemical Company) to ferrous protein via a gastight syringe.

Protein crystallization. WT *Ns* H-NOX and the L66W/L67W mutant were used as purified for crystallization. L66W and L67W were incubated with ~10 mM dithionite for 5-10 minutes in an anaerobic chamber (Coy) to ensure full reduction. All *Ns* H-NOX variants were exchanged into buffer E (5 mM Tris, pH 7.5, 100 mM NaCl, 1 mM DTT) using a PD-10 column. The proteins were crystallized at 20 °C using sitting drop vapor diffusion in which 1 μL of the protein was mixed with 1 μL of reservoir solution and equilibrated against a 700 μL reservoir. For WT *Ns* H-NOX, 15 or 30 mg/mL protein was equilibrated against 1.8 M DL-malic acid (pH 7.0) with and without 100 mM BIS-TRIS propane (pH 7.0). For L66W and L67W, 45 mg/mL protein was equilibrated against 1.9-2.0 M malonic acid (pH 7.0). For L66W/L67W, 10 mg/mL protein was equilibrated against 1.9-2.1 M malonic acid (pH 7.0).

Untagged *Tt* H-NOX was used as purified in the Fe^{II}–O_2 ligation state. Protein was exchanged into crystallization buffer F (20 mM TEA, pH 7.5) using a PD-10 column. Crystals were grown using sitting drop vapor diffusion in which 1 μL of the protein (30 or 60 mg/mL) was mixed with 1 μL of reservoir solution and equilibrated against a 700 μL reservoir of 20% to 28% (w/v) PEG 2000 and 200 mM to 250 mM sodium acetate at 20 °C.

All crystals appeared within 12 h. Cryoprotection was achieved by transferring the crystals stepwise into mother liquor solutions containing 5%, 10%, and 15% glycerol for *Ns* H-NOX variants and 5%, 10%, 15%, and 20% for *Tt* H-NOX. The crystals for native data sets were flash frozen in liquid N_2 for storage without further manipulation.

Xenon derivatization. Crystals were derivatized with xenon (research grade; Praxair, Inc.) using a Xenon Chamber (Hampton Research) apparatus following standard protocols (46). Briefly, the wick in the provided Mini-Vial/Wick system was saturated with cryoprotectant, and an additional ~75 μL of cryoprotectant was added to the bottom of the vial to prevent crystal dehydration. The cryoprotectant in the Mini-Vial/Wick system was pre-equilibrated with xenon by pressurizing the chamber 3 times at each xenon pressure to be subsequently used for crystal derivatization. Crystals underwent cryoprotection as described above and were immediately pressurized in the chamber with 1 atm to 8 atm xenon for 0.5, 1, 5, 10, 15, or 30 min. Following derivatization, the chamber was rapidly depressurized (<10 s), and the crystals were immediately frozen (~5 s) in liquid N_2 for storage.

X-ray data collection and structure refinement. For native crystals, X-ray data were collected using synchrotron radiation at beamlines 5.0.2 or 8.3.1 at the Advanced Light Source, Lawrence Berkeley National Laboratory (Berkeley, CA). Diffraction images were collected at 100 K with exposure times of 0.1 s to 1 s and 0.35º to 1º oscillations per frame at a wavelength of λ = 1.1158 Å. Data integration and scaling were performed using the HKL2000 (47) suite, and structure solution was performed using Phaser (48) with *Ns* H-NOX (PDB ID 2O09) or *Tt* H-NOX (PDB ID 1U55) as the search model. Rebuilding of the model was performed using ARP/wARP (49) following molecular replacement, and manual model rebuilding was performed using Coot (38). Iterative model refinement was performed using PHENIX (50) with TLS refinement parameters incorporated. Refinement statistics are listed in **Tables A.1 to A.3**. Stereochemical properties were assessed by MOLPROBITY (51) and PROCHECK (52).

For xenon-derivatized crystals, diffraction images were collected using inverse beam geometry at a wavelength of λ = 1.3776 Å to maximize xenon anomalous signal (Xe f'' = 5.8), and reflection intensities were scaled with anomalous flags selected. Structure solution was performed using rigid body refinement of the native structure against the scaled xenon intensities since the crystals were isomorphous. The location of xenon sites was determined by peak analysis from an anomalous difference map by selecting peaks greater than 4s that corresponded to peaks in the F_o–F_c map and did not

overlap with Fe (f'' = 2.6) or S (f'' = 0.5) atoms. For initial placement of each xenon atom, the B factor was set to the average of non-hydrogen protein atoms within 5 Å, and the occupancy was set to a value of 0.5. The occupancy and B-factor of each xenon atom were then iteratively refined using restrained refinement until there was no further positive electron density in the F_o–F_c map. Iterative model refinement and assessment of model correctness was carried out as described for the native structures.

Coordinates are deposited in the RCSB Protein Data Bank as entries **3TF8** (WT *Ns* H-NOX), **3TF9** (WT *Ns* H-NOX under 1 atm Xe), **3TFA** (WT *Ns* H-NOX under 6 atm Xe), **3TFD** (L66W), **3TFE** (L66W under 6 atm Xe), **3TFF** (L67W), and **3TFG** (L66W/L67W), **3TF0** (WT *Tt* H-NOX), and **3TF1** (WT *Tt* H-NOX under 6 atm Xe).

Stopped flow spectroscopy. CO association rate constants (k_{on}) were determined for ferrous *Ns* H-NOX (WT, L66W, L67W, L66W/L67W, T48W, and I9W) and ferrous WT *Tt* H-NOX (His_6) at 20 °C using a HiTech KinetAsyst stopped flow instrument equipped with a diode array detector. Ferric-unligated *Tt* H-NOX was prepared by first oxidizing the protein with excess potassium ferricyanide for 5 min at room temperature in an anaerobic chamber. Ferricyanide was then removed with a PD10 column by desalting the protein into buffer D. Both *Ns* and *Tt* H-NOX (~1 μM) were fully reduced with ~10 mM dithionite in an anaerobic chamber. CO binding experiments were conducted in the presence of ~10 mM dithionite to prevent *Tt* H-NOX from partially binding O_2 (K_D = 90 nM) during subsequent sample manipulation on the stopped flow. CO binding rates were found to be dithionite independent. Saturated CO stock solutions (950 μM) were prepared by sparging ~3 mL buffer in a septum-sealed Reacti-Vial (Pierce) with CO (99.99%; Praxair, Inc.) for >30 min at room temperature. Dilutions of CO (24, 48, 95, and 143 μM) were generated directly on the stopped flow in gas-tight syringes by mixing the saturated CO stock solution via a three-way joint with anaerobic buffer. Reactions were initiated by rapid, equal mixing of the ferrous protein (~1 μM) and CO solutions. UV–visible spectra were recorded for 450 ms (300 scans, 1.5 ms integration time) from 400-700 nm using the Kinetic Studio program (TgK Scientific). The spectral transition was fit to a two-state model using the SPECFIT Global Analysis System (version 3.0.14). Replicate CO titrations (N = 3-5) were carried out on different days utilizing protein from different preparations whenever possible. Average observed rates (k_{obs}) for each CO concentration are reported for >30 sample shots on the stopped flow.

For CO dissociation rate constants, ferrous-CO protein (2 μM) was mixed with an NO (99.5%; Praxair, Inc.) trap as described previously (40, 42). *Ns* H-NOX variants were fully reduced with ~10 mM dithionite in an anaerobic chamber. Dithionite was subsequently removed by desalting the proteins into buffer D using a PD10 column. *Tt* H-NOX (His_6) samples were oxidized prior to reduction as described above. Ferrous protein (~2 μM) was placed in a septum-sealed tonometer connected via a three-way joint to a syringe containing anaerobic buffer. The headspace of the tonometer was subsequently sparged with 1 atm CO gas (950 μM CO in solution) to prepare the protein Fe^{II}–CO complexes. Saturated NO solutions (2 mM) for NO traps were generated by sparging ~3 mL anaerobic buffer in a septum-sealed Reacti-Vial for >15 min at room

temperature with NO (99.5%; Praxair, Inc.) that had been passed through 10 M KOH. The saturated NO solution was removed from the Reacti-Vial with a gas-tight syringe that was then connected via a three-way joint to a syringe containing anaerobic buffer. Prior to sample delivery into the stopped flow, the stopped flow syringes were deoxygenated with an anaerobic dithionite solution. All dithionite was subsequently removed by flushing the stopped flow syringes with anaerobic buffer via the three-way joints described above. Reactions were initiated by rapid, equal mixing of the Fe^{II}–CO protein and NO trap. UV–visible spectra were recorded for 4.5 s from 350-700 nm using the Kinetic Studio program as above. The difference in absorbance (424 and 416 nm) versus time was fit to a single exponential equation using Igor Pro (version 5.01). Measurements were recorded from ≥3 samples on different days and represent ≥18 sample shots on the stopped flow. CO dissociation rates were verified to be independent of NO trap concentration as long as an excess of trap was used. To confirm trap independence, ferrous protein solution containing either 10 or 20 μM CO was mixed with traps containing 200 μM and 2 mM NO.

Flash photolysis. CO association rate constants were also determined using transient absorption spectroscopy at the Beckman Institute Laser Resource Center (California Institute of Technology, Pasadena, CA) with an experimental set-up that has been described previously (53). Proteins were reduced with dithionite in a glove box and desalted into spectral buffer D using a PD10 column to remove the dithionite. The anaerobic proteins were subsequently sparged with 1 atm CO in a sealed 1 cm pathlength quartz cuvette and incubated under a CO atmosphere overnight at 4 °C with gentle rocking to ensure full sample equilibration prior to data acquisition. The protein Fe^{II}–CO bond was photolyzed using 560 nm irradiation from a Nd:YAG laser (8 ns pulse). Data were collected at 20 °C over 10 ms at 415 and 440 nm from 2 samples on different days. Traces were fit to a single exponential equation using Igor Pro.

Results

Probing gas migration in the predicted tunnels with xenon. X-ray diffraction utilizing xenon is a powerful structural tool to observe gas diffusion through proteins (34). Xenon has a similar polarity and van der Waals radius to diatomic gases (2.16 Å versus 1.50-1.55 Å for O_2, CO, and NO) (35), is freely diffusible in protein crystals, and weakly interacts with protein molecules (34). Importantly, xenon also possesses an appreciable anomalous signal, allowing for unambiguous localization of xenon atoms in protein crystal structures (34). Although xenon has high polarizability, which can bias interactions toward regions in proteins with more polarizable side chains (36), numerous studies have confirmed that the locations of xenon binding sites correlate well with areas that are favorable for diatomic gas migration (12, 13).

Crystals of ferrous-unligated *Ns* H-NOX were obtained for xenon pressurization via sitting drop vapor diffusion. A 2.13 Å structure of the native protein was solved by molecular replacement using the previously published structure of ferrous-unligated *Ns* H-NOX (PDB ID 2O09) (32), which was obtained under different crystallization

conditions, as the search model (**Table A.1**). The *Ns* H-NOX crystal structure solved here was at a similar resolution (2.13 Å vs. 2.10 Å) in the identical space group ($P2_13$) and had comparable unit cell dimensions (a = b = c = 123.7 Å vs. 123.4 Å) as the previous structure (32). The two structures were found to superimpose well with an rmsd of 0.197 Å (C_α–C_α alignment).

To map the putative tunnels in *Ns* H-NOX, native *Ns* H-NOX crystals were subsequently exposed to 1-6 atm of xenon for various times using a xenon pressurization chamber (Hampton Research). A crystal structure of *Ns* H-NOX pressurized with 1 atm of xenon is reported to 2.59 Å resolution (**Table A.1**). As shown in **Figure 2.2A**, 1 xenon atom (blue mesh) was observed per protein molecule at this pressure. The xenon atom is located at the intersection of the apparent tunnels near the distal face of the heme where diatomic ligands bind. The presence of xenon is indicated by spherical electron density in the $2mF_o–DF_c$ map generated for *Ns* H-NOX (**Figure 2.2A**) and unambiguously confirmed by the presence of xenon electron density in the anomalous difference map at the same position (**Figure A.1**). The xenon-binding cavity is formed by several hydrophobic contacts. These include the faces of the porphyrin macrocycle and W74 indole ring, the V5 and L148 side chains, the M1 and M144 sulfur atoms, as well as the F70 phenyl ring edge (**Figure A.2**).

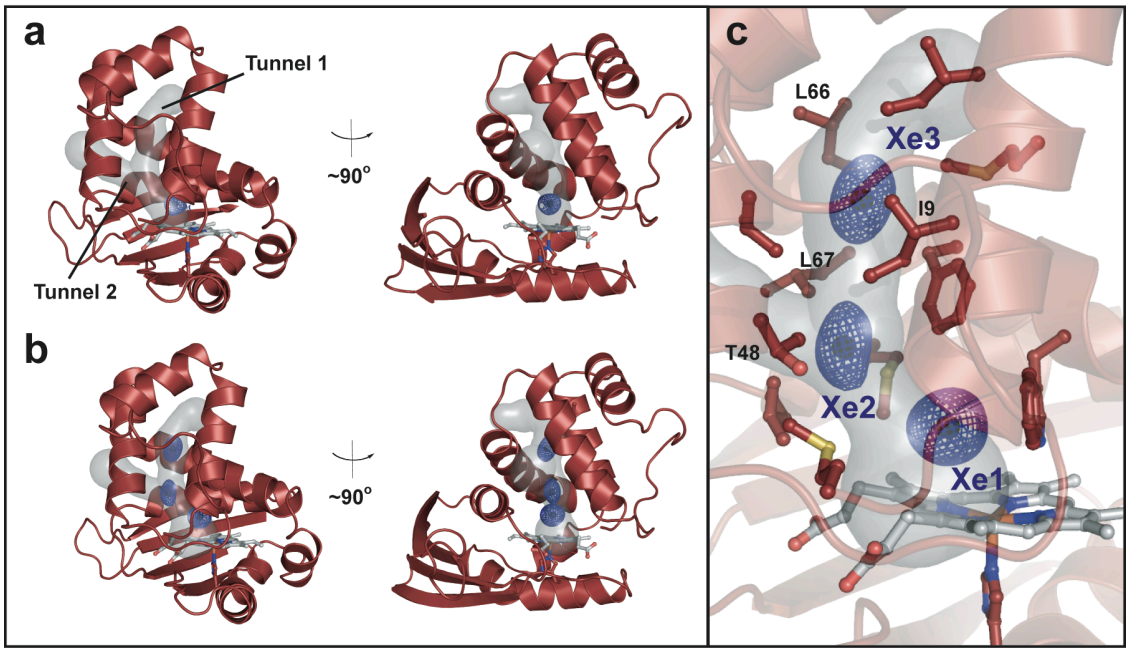

Figure 2.2 Crystal structures of WT *Ns* H-NOX following xenon pressurization. Structures are reported for crystals pressurized with **(a)** 1 atm of xenon for 1 min and **(b)** 6 atm of xenon for 1 min. $2mF_o–DF_c$ maps (mesh surface) for xenon atoms are contoured at 1σ (see **Figure A.1** for anomalous xenon density). **(c)** A detailed view of the 6 atm crystal structure showing numerous residues that line the tunnel network. Key residues that were selected for structure-based rational mutagenesis are indicated. See **Figure A.2** for views of the individual xenon-binding sites (Xe1, Xe2, and Xe3). The tunnel network was modeled using CAVER with the heme iron as the point of origin and a probe radius of 1.5 Å.

To test if *Ns* H-NOX has other accessible xenon-binding sites, a crystal structure of *Ns* H-NOX under 6 atm of xenon was obtained (**Table A.1**). The structure was solved to 2.27 Å resolution and found to align well with the native structure (0.127 Å C_α rmsd). At this higher pressure, three xenon atoms were observed that extend between the heme and the end of tunnel 1 near the solvent interface. The presence of xenon at these locations is evident from electron density in the $2mF_o–DF_c$ map (**Figures 2.2B and 2.2C**) and the superposition of xenon electron density in the anomalous difference map (**Figure A.1**). Xenon binding in the site identified at lower pressure (herein referred to as "Xe1") is still observed and occurs with higher occupancy in the 6 atm structure (occupancy of 0.6 vs. 0.3 in molecule A). The newly identified sites (referred to as "Xe2" and "Xe3") are also predominately composed of hydrophobic residues (**Figure 2.2C**). For the Xe2 site, the side chains of V5, I9, L67, and L141 as well as the T48 methyl group and face of the F70 aromatic ring contribute to form the xenon-binding pocket. For the Xe3 site at the end of tunnel 1, the binding pocket opens into solvent and is formed at its base by the side chains of I9, M12, I13, V52, and L66, as well as the face of the F70 aromatic ring (**Figure A.2**). Notably, no xenon occupancy was observed in tunnel 2. This smaller channel is predicted to be accessible to diatomic gases in the crystal structure based on molecular modeling (37). However, it may be too narrow to effectively accommodate xenon and/or may lack sufficient contacts to stabilize xenon binding.

The crystallographic data suggest a dynamic picture for xenon movement in the tunnels. Xenon flux is supported by anisotropic electron density at the Xe2 and Xe3 sites (**Figure 2.2C**) and residual density that bridges these sites in the $2mF_o–DF_c$ map for the structure at lower contour levels. Xenon flux in the structure is correlated to xenon occupancy, which decreases from 0.6 to 0.3 to 0.4 for Xe1, Xe2, and Xe3, respectively (using molecule A) (**Table A.1**). Together, the data indicate that xenon moves most dynamically in the tunnel near the protein exterior and more stably interacts with the protein distal to the heme at the Xe1 site. Based on these observations, the tunnels appear to funnel gases between the solvent and protein interior where they are preferentially trapped in the heme distal pocket.

To compare to O_2-binding H-NOX proteins, which do not appear to display a tunnel network (**Figure A.3**) (33), crystals of the H-NOX protein from *Thermoanaerobacter tengcongensis* (*Tt* H-NOX) were pressurized with 6 atm of xenon. The resulting crystal structure of *Tt* H-NOX was solved to 2.03 Å resolution (**Table A.3**) and found to overlay well with the native structure (0.129 Å C_α rmsd). Under these pressurization conditions, two xenon atoms were bound to each protein molecule (**Figure A.3**). However, unlike *Ns* H-NOX, a continuous pathway could not be traced in *Tt* H-NOX, either between the xenon atoms or to the heme pocket. This finding supports the prediction that gas diffusion in O_2-binding H-NOX domains may not occur through discrete, preformed tunnels.

Structure-guided design of mutations to block the tunnel network. To examine the role of the *Ns* H-NOX tunnels in modulating ligand migration, structure-guided mutants were designed in an attempt to block each branch of the tunnel network. Although numerous positions are potentially available for mutagenesis, two candidates (L66W to block tunnel 1 and L67W to block tunnel 2) were selected following modeling of allowed side chain rotamers (38) (**Figure 2.2C**). Leucine-to-tryptophan mutations were chosen principally to provide sufficient steric bulk to interact tightly with surrounding tunnel residues. Additionally, these mutations are predicted to maintain the hydrophobicity of the site (leucine and tryptophan partition coefficients differ by only 0.07) (39). The L66W, L67W, and L66W/L67W variants were generated using standard protocols and purified in a manner analogous to WT *Ns* H-NOX. Ferrous complexes (Fe^{II}–unligated, Fe^{II}–CO, and Fe^{II}–NO) of the isolated proteins were characterized with steady-state UV–visible spectroscopy. UV–visible spectra of the mutants were very similar to those of WT *Ns* H-NOX (**Table A.4**), indicating that incorporation of tryptophan residues in the selected positions did not significantly alter the electronic properties of the heme.

Crystal structures of predicted tunnel-blocking tryptophan mutants. High-resolution crystal structures of the *Ns* H-NOX variants were pursued to establish the effectiveness of the tryptophan residues in blocking the tunnels. Crystals of L66W, L67W, and the L66W/L67W double mutant were obtained in similar conditions to the WT protein (see **Experimental Procedures**). The structures were solved to 1.96 Å, 1.94 Å, and 1.90 Å resolution, respectively (**Figure 2.3**). Notably, the structures were obtained

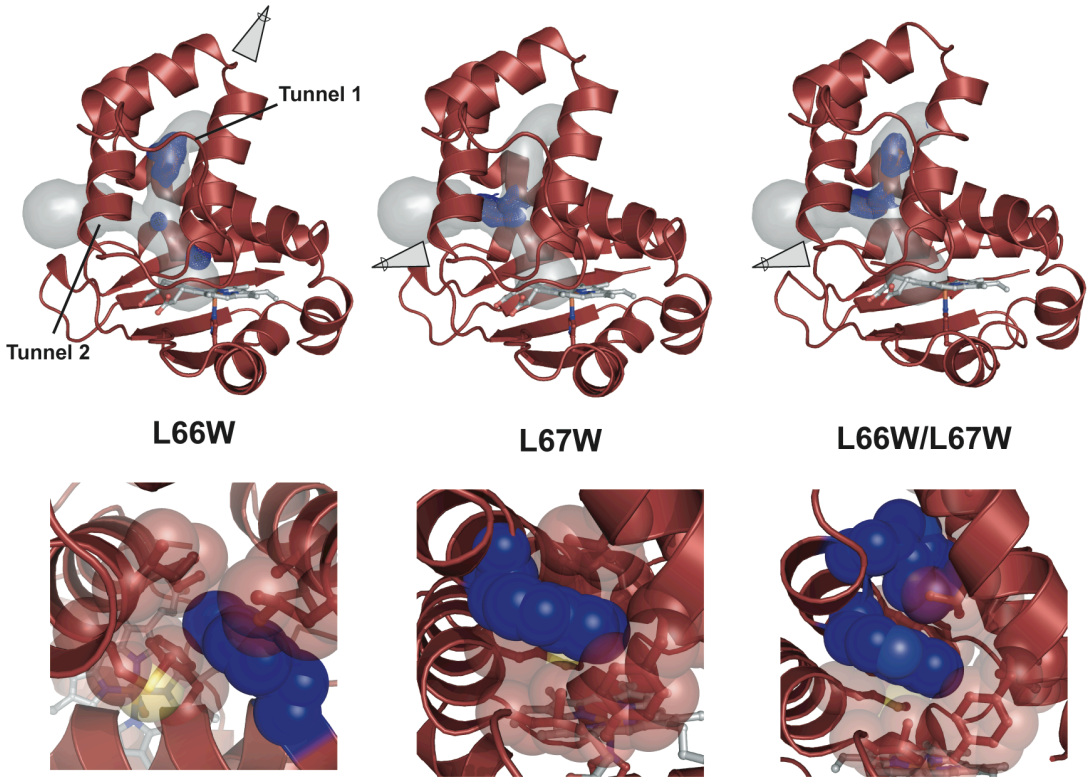

Figure 2.3 Crystal structures of tunnel-blocking variants in *Ns* H-NOX. Structures of L66W (pressurized with 6 atm of xenon for 1 min), L67W, and L66W/L67W are shown. L66W blocks tunnel 1 and L67W blocks tunnel 2. Zoom-in views looking from the solvent to heme pocket depict van der Waals contacts with surrounding tunnel residues: I9, M12, I13, V52, A55, L59, L67, and F70 (for L66W) and T48, V52, F70, L141, M144, Y49 (for L67W). Simulated-annealing composite omit maps (mesh surface) are shown for the tryptophan side chains. $2mF_o$–DF_c maps (mesh surface) for xenon atoms are contoured at 1σ (see **Figure A.1** for anomalous xenon density). The tunnel network was modeled with CAVER using the WT *Ns* H-NOX structure.

in the same space group and found to have nearly identical unit cell dimensions as WT *Ns* H-NOX (**Table A.2**), providing initial evidence that introduction of the tryptophan residues did not significantly alter the native fold. The final crystal structures were found to superimpose well with the WT protein (**Figure A.4**). C_α rmsd values of 0.273, 0.286, and 0.158 Å were obtained for L66W, L67W, and L66W/L67W, respectively (using molecule A of each structure).

Closer inspection of the tryptophans in each crystal structure show that the side chains were incorporated within the tunnel network as expected. Simulated-annealing composite omit maps for the L66W and L67W side chains show unambiguous electron density from the tryptophan indole rings (**Figure 2.3**). These side chains make tight van der Waals contact with the surrounding, predominately hydrophobic residues in the tunnels. The tryptophan indole ring in the L66W single mutant is packed tightly by I9, M12, I13, V52, A55, L59, L67, and F70 at the top of tunnel 1. The tryptophan indole ring in the L67W single mutant is tightly contacted by T48, V52, F70, and L141 as well as the sulfur atom of M144 and the face of the Y49 phenol ring. Notably, the large tryptophan

side chains appear to fit into the open space in the tunnel network and sterically seal tunnel 1 and tunnel 2. Decreased B-factors in the crystal structures at these sites support tight van der Waals contacts between the tryptophan side chains and tunnel residues and suggest that introduction of the tryptophan residues locally enhances conformational rigidity.

The tryptophan side chains in molecule A of the double mutant (L66W/L67W) are in the same orientation as the single mutants and contacts with surrounding residues in the tunnels are preserved (**Figure 2.3**). Additionally, the edge of the L66W residue is in van der Waals contact with the face of the L67W indole ring. In molecule B of the double mutant, the L66W side chain is in at least one different rotameric position than in molecule A but still functions to partially seal the tunnel (**Figure A.5**). The different observable rotamers of L66W suggest that this side chain has enhanced flexibility in the double mutant structure.

To examine the effect of blocking the tunnels on gas accessibility in *Ns* H-NOX, crystals of L66W were subsequently pressurized with xenon. L66W was selected as a representative mutant because it is predicted to block the main pathway (tunnel 1) for xenon diffusion between the solvent and protein interior. The structure of L66W under 6 atm of xenon was obtained for direct comparison to WT *Ns* H-NOX (**Table A.2**). As seen in the 1.99 Å resolution structure (0.071 Å C_α rmsd vs. native L66W), introduction of the tryptophan residue in tunnel 1 sterically blocks xenon binding at the former Xe3 position but preserves the Xe1 and Xe2 sites (**Figure 2.3** and **Figure A.1**). Retention of xenon binding in the single mutant reflects the ability of xenon to access the base of the channel through other pathway(s). This suggests that tunnel 2 could serve as a possible conduit for gases even though xenon occupancy remains to be observed in that tunnel directly.

Together the structural data indicate that the *Ns* H-NOX tunnel network was blocked by introducing tryptophan residues and that these residues sterically control gas migration in the protein interior. The ability to modify the protein without significant structural changes suggests that this approach represents a unique opportunity to systematically dissect the contribution of the H-NOX tunnels to ligand binding kinetics at the heme.

Blocking the tunnels affects the CO k_{on}. To examine how blocking the tunnel network affects ligand association rates, time-resolved absorption spectroscopies using CO gas were employed with the tryptophan variants. CO has several important advantages over NO as a spectroscopic tool to probe ligand migration in heme proteins: **(1)** CO reacts more slowly (~100-1000 fold) with ferrous heme (40), **(2)** CO has been previously shown to both bind to and dissociate from the *Ns* H-NOX heme in a simple 1-step process (40), and **(3)** CO does not participate in redox chemistry with proteins (41). Two likely outcomes were predicted for blocking the tunnels with respect to ligand binding. Blocking the tunnels could decrease CO association rate constants (k_{on} values or "on-rates") if diffusion into the heme pocket were dramatically slowed. Alternatively, on-rates could increase if ligand trapping in the heme pocket were enhanced (following

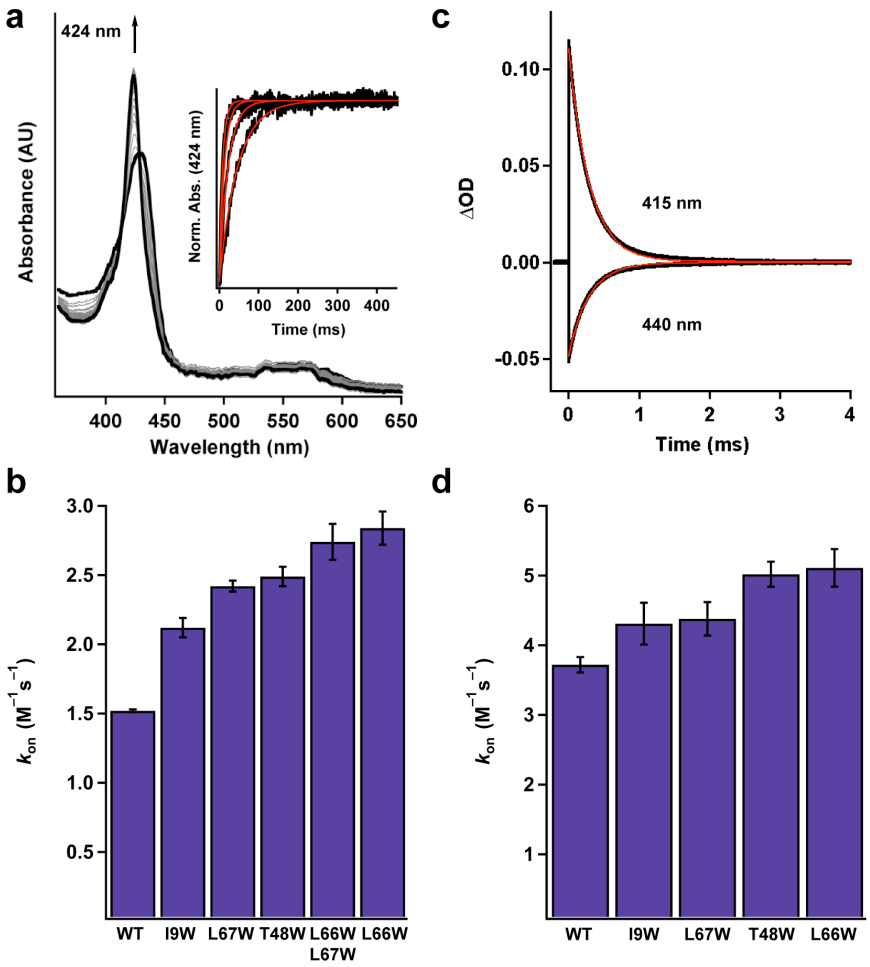

Figure 2.4 Determination of CO k_{on} values (x 10^6 $M^{-1}s^{-1}$) for the *Ns* H-NOX variants. **(a)** Time-resolved UV–visible spectra of CO binding to WT ferrous *Ns* H-NOX in a stopped flow spectrometer (11.9 μM CO data is shown). **(Inset, a)** Single wavelength stopped flow traces of the absorbance at 424 nm versus time for WT *Ns* H-NOX in the presence of varying CO concentrations. **(b)** Summary of CO k_{on} values for the *Ns* H-NOX variants determined with stopped flow spectroscopy (see **Figure A.6** for a plot of k_{obs} versus CO concentration). N = 3-5. Error represents the standard deviation. **(c)** Transient absorption traces of CO binding to WT ferrous *Ns* H-NOX under 1 atm of CO following laser photolysis. The trace at 440 nm represents the loss of the Fe^{II}–unligated species, and the trace at 415 nm represents the formation of the Fe^{II}–CO species. **(d)** Summary of CO k_{on} values for all the *Ns* H-NOX variants determined with laser photolysis. N = 2. Error represents the standard deviation.

ligand diffusion through the protein matrix) due to the blocking of route(s) for ligand escape.

CO on-rates for the tryptophan variants were measured with stopped flow spectroscopy in a manner similar to that described previously (40). Ferrous protein was rapidly mixed with increasing CO concentrations, and CO binding was followed using a diode array detector on a stopped flow instrument (**Figure 2.4A**). Plots of observed rate (k_{obs}) versus CO concentration (**Figure A.6**) were used to calculate k_{on} values from the slope of the linear fits. WT *Ns* H-NOX had a CO k_{on} of 1.52 x 10^6 $M^{-1}s^{-1}$, which is

comparable to the previously reported value (40). To our initial surprise, all the tunnel-blocking variants exhibited faster CO k_{on} values compared to the WT protein. The on-rate for L67W (blocking tunnel 2) increased by 50%, while the on-rates for L66W (blocking tunnel 1) and L66W/L67W increased by approximately 100% relative to the WT protein (**Figure 2.4B** and **Table 2.1**). These data indicate that even with blocking the tunnels, CO is still able to rapidly diffuse through the protein matrix, which likely occurs within the dead time of the stopped flow measurement (<1.5 ms). Therefore, CO on-rates determined with stopped flow spectroscopy appear to reflect CO binding following diffusion from both the solvent and protein scaffold. In agreement with the xenon pressurization data, the most significant changes in rate are observed upon blocking tunnel 1, which suggests that it is a more favorable ligand migration pathway.

Table 2.1 CO binding constants for *Ns* H-NOX and selected H-NOX proteins

Protein	CO k_{on} (x 10^6 $M^{-1}s^{-1}$)		CO k_{off} (s^{-1})	CO K_D[a] (μM)	*Ref.*[b]
	Laser Photolysis	Stopped Flow			
***Ns* H-NOX**					
Wild-type	3.7 ± 0.1	1.52 ± 0.01	6.73 ± 0.42	4.42 ± 0.28	
L67W	4.4 ± 0.2	2.42 ± 0.04	6.71 ± 0.15	2.78 ± 0.08	
L66W	5.1 ± 0.3	2.84 ± 0.12	7.36 ± 0.62	2.59 ± 0.24	
L66W/L67W	N/D	2.74 ± 0.13	5.36 ± 0.20	1.96 ± 0.12	
T48W	5.0 ± 0.2	2.49 ± 0.07	4.13 ± 0.54	1.66 ± 0.22	
I9W	4.3 ± 0.3	2.12 ± 0.07	7.00 ± 0.18	3.30 ± 0.14	
***Tt* H-NOX**	4.1 ± 0.2	2.18 ± 0.09	3.56 ± 0.42	1.63 ± 0.20	
sGC	N/D	0.0358 ± 0.0015	3.5 ± 0.5	98 ± 15	*(54)*

[a] Calculated from k_{off}/k_{on} using stopped flow data. [b] This work unless otherwise noted. N/D = not determined. Error (±) represents the standard deviation.

To confirm the increases observed in CO on-rates when the tunnels are blocked, tryptophan residues were also engineered at the I9 and T48 positions in the tunnel network. I9 and T48 are located on different α-helices than L66W and L67W (**Figure 2.2)**. Based on modeling of allowed tryptophan rotamers (38), the T48W side chain is predicted to be incorporated near the branch point between tunnel 1 and tunnel 2, and the I9W side chain is predicted to be incorporated further away from the heme in tunnel 1 in between the locations of T48W and L66W (**Figure A.7**). The I9W and T48W single mutants were generated as described above. As with the other variants, UV–visible spectra obtained for T48W and I9W heme-ligand complexes were very similar to the WT protein (**Table A.4**), again suggesting that the tryptophan residues did not greatly alter

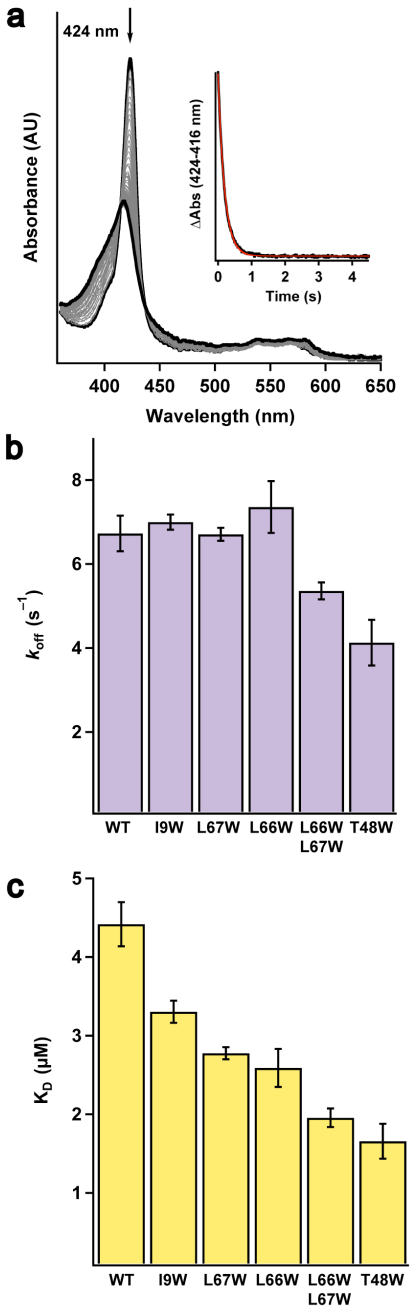

Figure 2.5 Determination of CO k_{off} and K_D values for the *Ns* H-NOX variants. **(a)** Time-resolved UV–visible spectra of CO dissociation from Fe^{II}–CO WT *Ns* H-NOX in the presence of an NO trap in a stopped flow spectrometer. **(Inset, a)** Absorbance at 424 nm vs. time for CO dissociation from WT *Ns* H-NOX. **(b)** Summary of CO k_{off} values. N ≥ 3. Error represents the standard deviation. **(c)** Summary of CO K_D values for all the *Ns* H-NOX variants. K_D values were obtained from k_{off}/k_{on}.

the electronic properties of the heme. Characterization of CO on-rates with stopped flow spectroscopy illustrated that the CO k_{on} values for I9W and T48W are faster than WT. The T48W variant in particular exhibited a greater increase in rate that is similar to L66W and the L66W/L67W double mutant (**Figure 2.4B** and **Table 2.1**). The increases in ligand on-rates across a broad panel of tunnel-blocking mutants suggest that the kinetic trend is a general phenomenon.

To eliminate the requirement for CO diffusion into the heme pocket during data acquisition, association kinetics were also evaluated in the tryptophan variants under a CO-equilibrated atmosphere using laser photolysis (42). Ferrous *Ns* H-NOX was incubated anaerobically overnight under 1 atm of CO to ensure full sample equilibration. Photolysis of the Fe^{II}–CO bond was carried out using 560 nm laser irradiation to transiently form the Fe^{II}–unligated heme. CO binding was subsequently followed over a 10 ms timescale (**Figure 2.4C**) (26, 42). A CO k_{on} value of 3.7 x 10^6 $M^{-1}s^{-1}$ was obtained for WT *Ns* H-NOX. This rate is somewhat faster than the CO on-rate (1.52 x 10^6 $M^{-1}s^{-1}$) observed in the stopped flow experiment, which could reflect different protein conformational changes formed upon photodissociation of the CO ligand. Importantly, the relative trend in CO on-rates for the tunnel-blocking variants obtained with laser photolysis parallels what was observed in the stopped flow experiment. WT *Ns* H-NOX exhibited the slowest on-rate, and the tunnel-blocking mutants exhibited faster rates with L66W showing the greatest increase (**Figure 2.4D** and **Table 2.1**). The lack of significant structural changes in the tryptophan variants suggests that the faster ligand on-rates are due to more efficient ligand

trapping in the protein interior. Blocking the tunnels both individually and together appears to eliminate routes of ligand diffusion from the protein to the solvent, increasing the effective CO concentration near the heme and the subsequent rate of CO binding to the iron.

Blocking the tunnels decreases the CO k_{off} and enhances CO binding affinity. To examine if increased ligand trapping in the heme pocket also affects CO dissociation kinetics, dissociation rate constants (k_{off} values or "off-rates") were measured for the *Ns* H-NOX variants using stopped flow spectroscopy in the presence of an NO trap (40, 42). An NO trap was utilized in order to limit CO rebinding following CO release from the heme. NO reacts quickly (~10^8 $M^{-1}s^{-1}$) with ferrous heme and binds with high affinity (K_D ~pM) such that CO is not able to displace NO once it is coordinated to the iron (40, 42). WT *Ns* H-NOX was found to have a CO k_{off} value of 6.73 s^{-1} (**Figure 2.5A**), which is comparable to that reported previously (40). Several of the single tryptophan tunnel-blocking mutants (I9W, L66W, and L67W) had no significant change in CO off-rate. However, the L66W/L67W double mutant and the T48W mutant exhibited slower rates than WT (**Figure 2.5B** and **Table 2.1**). It appears that blocking both tunnels is necessary to elicit an effect on CO k_{off} values. These tryptophan residues likely decrease the CO off-rate by increasing rapid CO recombination to the heme following transient dissociation.

Calculation of CO K_D values (k_{off}/k_{on}) shows that blocking the tunnels increases CO binding affinity up to ~2.5 fold or ~2.2 fold in the T48W mutant based on stopped-flow and photolysis data, respectively (**Figure 2.5C** and **Table 2.1**). The enhancement in ligand affinity is due to an increase in CO on-rate and decrease in CO off-rate, which appears to be associated with better ligand trapping in the heme pocket (**Figure 2.6**). Additionally, the enhanced ligand affinity in the smaller cavity is likely thermodynamically favorable due to a decreased entropic penalty associated with ligand binding (16). Together these data attest to the ability of H-NOX protein scaffolds to modulate ligand flux through the protein interior and implicates a role for protein tunnels in tuning ligand-binding properties in the H-NOX family.

Discussion

Extensive studies on the globins have provided a model for how heme protein scaffolds control ligand binding (16, 17). Myoglobin, for example, has a heme group surrounded by deep gas pockets that work to efficiently capture and release O_2 (16, 17). H-NOX protein scaffolds possess a novel fold and, unlike the globins, bind a heme cofactor that is completely buried within the protein interior. This framework appears to funnel gases toward the heme pocket and tune gas-sensing properties for involvement in diverse signaling pathways.

Much work has elucidated important determinants of ligand binding in the H-NOX family (25-30). However, the direct role of the protein scaffold in modulating ligand binding from sites beyond the heme pocket has not been previously addressed. Utilizing X-ray crystallography with xenon and kinetic measurements, a tunnel network has been mapped in a non-O_2-binding H-NOX protein (*Ns* H-NOX) that appears to be

conserved in H-NOX proteins with similar ligand-binding properties. The tunnel network consists of a Y-shaped, hydrophobic channel that serves as a pathway for gas diffusion to and from the heme (**Figure 2.2**). Blocking the tunnel network influences heme ligand-binding kinetics – increasing ligand on-rates and decreasing ligand off-rates. These changes appear to be due to better ligand trapping near the heme, which results from removing pathways for ligand escape to the solvent (**Figure 2.6**).

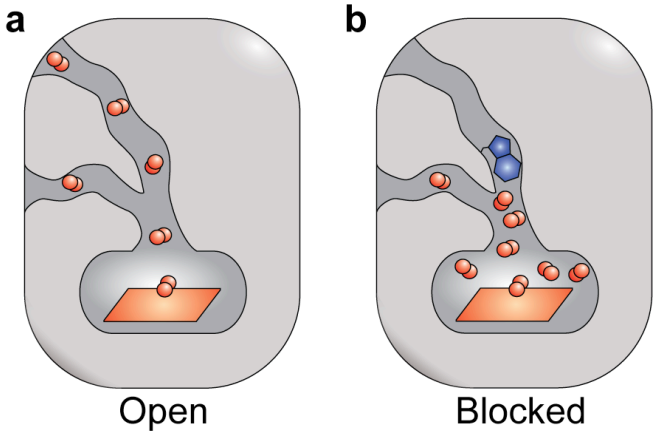

Figure 2.6 Tunnel-blocking mutants modulate heme ligand-binding properties in H-NOX proteins by altering ligand migration. **(a)** A native H-NOX protein and **(b)** an H-NOX protein with tunnel 1 blocked are shown. A tryptophan residue is shown in blue and diatomic ligands are shown in red. Blocking the tunnels individually (L66W and L67W mutants) and together (L66W/L67W mutant) in *Ns* H-NOX increases ligand trapping in the protein interior. This functions to both increase the CO k_{on} following CO diffusion through the protein scaffold and decrease the CO k_{off}. These kinetic trends appear to be due to the elimination of route(s) for ligand escape.

Although globins and H-NOX domains have unique interior routes for ligand diffusion, comparison between these protein families shows that divergent topological features may tune reversible ligand binding in parallel ways. Similar to *Ns* H-NOX, mutagenesis studies in myoglobin have found that mutations that vary the size and character of cavities affect affinity by modifying the occupation and migration of ligands (16, 17). This is reflected in O_2 photolysis experiments on short time scales (ns-µs) where blocking the gas pocket distal to the heme increases the fraction and rate of geminate ligand rebinding (16, 17). However, unlike *Ns* H-NOX, decreasing the interior cavity volume in myoglobin with structure-guided mutagenesis is associated with slowed ligand on-rates (16, 17). This is likely due to less efficient ligand capture in myoglobin's more open heme site where decreasing the interior cavity volume appears to preferentially favor ligand escape (16, 17).

To provide initial insight into ligand migration in H-NOX proteins, a molecular dynamics (MD) study was conducted (33). The results of the MD simulations are in agreement with the ligand diffusion pathways observed here. Additionally, the calculations show that the presence of preformed pathways in *Ns* H-NOX increases the rate of CO escape to solvent relative to *Tt* H-NOX, which does not have an open tunnel network (**Figure A.3**) (33). This observation is consistent with the experimentally

determined CO dissociation rates for both proteins reported in the present study (**Table 2.1**) and supports the hypothesis that blocking protein tunnels increases ligand capture.

Protein dynamics in H-NOX domains could work in concert with tunnels to control ligand diffusion to and from the heme pocket. A MD simulation carried out on *Tt* H-NOX, for example, led to the conclusion that the protein fluctuates near the heme edge to permit ligand flux (33). The potential role of transiently formed pathways in facilitating ligand access is particularly evident in *Ns* H-NOX when both tunnels are blocked. It is possible that the introduction of bulky residues could alter protein dynamics in a manner not evident in the structural data to form additional routes for ligand diffusion. Potential changes in dynamics in the mutants could also dampen our observed kinetic effects. Importantly, these transient pathways appear less important in the native *Ns* H-NOX scaffold where both computational and experimental data suggest that the open tunnel network represents the most favorable route for gas diffusion.

Differences in ligand flux between divergent classes of H-NOX proteins may influence ligand specificity. In H-NOX proteins that bind O_2, the absence of preformed tunnels could work in concert with H-bonding residues to trap O_2 at the heme iron and tighten O_2 affinity through enhancing ligand rebinding (33). Most bacterial O_2-binding H-NOX domains identified to date are in obligate anaerobes where a high O_2 affinity would be important to sense and respond to low amounts of environmental O_2 (24). In non-O_2-binding H-NOX proteins, the tunnel network appears to permit more ligand flux through the heme pocket. This could favor NO binding under aerobic conditions since NO binds to ferrous heme with higher intrinsic affinity than O_2 (42). The potential ability to tune ligand-binding properties with distinct interior architectures may reflect the co-evolution of ligand diffusion pathways and diverse H-NOX protein functions.

Internal topological features in numerous proteins are essential for controlling the capture and release of biomolecules. For example, in NiFe hydrogenase, tunnels have been shown to promote H_2 back-exchange with solvent but also facilitate the escape of inhibitory amounts of CO (4); in superoxide dismutase, a positively charged cleft steers O_2^- to the active site, enabling nearly diffusion-limited turnover rates (43); and in soybean lipoxygenase, the route of O_2 migration into the active site influences product regiochemistry (2). Results reported here show that a tunnel network in H-NOX heme sensor domains guides gases to the heme iron and also tunes reversible gas binding by establishing routes for ligand diffusion. Together, our findings reflect the tightly coordinated relationship between protein frameworks and protein function. Structural features are employed in proteins not only to directly participate in active site chemistry but also control the flux of biomolecules. A deeper understanding of this complex relationship is essential to unraveling protein mechanisms and predicting biochemical properties across diverse protein families.

References

1. Baron R, Riley C, Chenprakhon P, Thotsaporn K, Winter RT, Alfieri A, Forneris F, van Berkel WJ, Chaiyen P, Fraaije MW*, et al.* (2009) Multiple pathways guide oxygen diffusion into flavoenzyme active sites. *Proc Natl Acad Sci U S A* 106: 10603-10608.
2. Knapp MJ, Seebeck FP, & Klinman JP (2001) Steric control of oxygenation regiochemistry in soybean lipoxygenase-1. *J Am Chem Soc* 123: 2931-2932.
3. Igarashi RY & Seefeldt LC (2003) Nitrogen fixation: the mechanism of the Mo-dependent nitrogenase. *Crit Rev Biochem Mol Biol* 38: 351-384.
4. Leroux F, Dementin S, Burlat B, Cournac L, Volbeda A, Champ S, Martin L, Guigliarelli B, Bertrand P, Fontecilla-Camps J*, et al.* (2008) Experimental approaches to kinetics of gas diffusion in hydrogenase. *Proc Natl Acad Sci U S A* 105: 11188-11193.
5. Doukov TI, Iverson TM, Seravalli J, Ragsdale SW, & Drennan CL (2002) A Ni-Fe-Cu center in a bifunctional carbon monoxide dehydrogenase/acetyl-CoA synthase. *Science* 298: 567-572.
6. Manjasetty BA, Powlowski J, & Vrielink A (2003) Crystal structure of a bifunctional aldolase-dehydrogenase: sequestering a reactive and volatile intermediate. *Proc Natl Acad Sci U S A* 100: 6992-6997.
7. Lund L, Fan Y, Shao Q, Gao YQ, & Raushel FM Carbamate transport in carbamoyl phosphate synthetase: a theoretical and experimental investigation. *J Am Chem Soc* 132: 3870-3878.
8. Hyde CC, Ahmed SA, Padlan EA, Miles EW, & Davies DR (1988) Three-dimensional structure of the tryptophan synthase alpha 2 beta 2 multienzyme complex from *Salmonella typhimurium*. *J Biol Chem* 263: 17857-17871.
9. Tilton RF, Jr., Kuntz ID, Jr., & Petsko GA (1984) Cavities in proteins: structure of a metmyoglobin-xenon complex solved to 1.9 A. *Biochemistry* 23: 2849-2857.
10. Austin RH, Beeson KW, Eisenstein L, Frauenfelder H, & Gunsalus IC (1975) Dynamics of ligand binding to myoglobin. *Biochemistry* 14: 5355-5373.
11. Schlichting I, Berendzen J, Phillips GN, Jr., & Sweet RM (1994) Crystal structure of photolysed carbonmonoxy-myoglobin. *Nature* 371: 808-812.
12. Schotte F, Lim M, Jackson TA, Smirnov AV, Soman J, Olson JS, Phillips GN, Jr., Wulff M, & Anfinrud PA (2003) Watching a protein as it functions with 150-ps time-resolved x-ray crystallography. *Science* 300: 1944-1947.
13. Cohen J, Arkhipov A, Braun R, & Schulten K (2006) Imaging the migration pathways for O_2, CO, NO, and Xe inside myoglobin. Biophys J 91: 1844-1857.
14. Elber R (2010) Ligand diffusion in globins: simulations versus experiment. *Curr Opin Struct Biol* 20: 162-167.
15. Ringe D, Petsko GA, Kerr DE, & Ortiz de Montellano PR (1984) Reaction of myoglobin with phenylhydrazine: a molecular doorstop. *Biochemistry* 23: 2-4.
16. Olson JS, Soman J, & Phillips GN, Jr. (2007) Ligand pathways in myoglobin: a review of Trp cavity mutations. *IUBMB Life* 59: 552-562.
17. Scott EE, Gibson QH, & Olson JS (2001) Mapping the pathways for O_2 entry into and exit from myoglobin. *J Biol Chem* 276: 5177-5188.
18. Salter MD, Nienhaus K, Nienhaus GU, Dewilde S, Moens L, Pesce A, Nardini M, Bolognesi M, & Olson JS (2008) The apolar channel in *Cerebratulus lacteus* hemoglobin is the route for O_2 entry and exit. *J Biol Chem* 283: 35689-35702.

19. Milani M, Pesce A, Ouellet Y, Dewilde S, Friedman J, Ascenzi P, Guertin M, & Bolognesi M (2004) Heme-ligand tunneling in group I truncated hemoglobins. *J Biol Chem* 279: 21520-21525.
20. de Sanctis D, Dewilde S, Pesce A, Moens L, Ascenzi P, Hankeln T, Burmester T, & Bolognesi M (2004) Crystal structure of cytoglobin: the fourth globin type discovered in man displays heme hexa-coordination. *J Mol Biol* 336: 917-927.
21. Pesce A, Dewilde S, Nardini M, Moens L, Ascenzi P, Hankeln T, Burmester T, & Bolognesi M (2003) Human brain neuroglobin structure reveals a distinct mode of controlling oxygen affinity. *Structure* 11: 1087-1095.
22. Hargrove MS, Barry JK, Brucker EA, Berry MB, Phillips GN, Jr., Olson JS, Arredondo-Peter R, Dean JM, Klucas RV, & Sarath G (1997) Characterization of recombinant soybean leghemoglobin a and apolar distal histidine mutants. *J Mol Biol* 266: 1032-1042.
23. Vallone B, Nienhaus K, Matthes A, Brunori M, & Nienhaus GU (2004) The structure of carbonmonoxy neuroglobin reveals a heme-sliding mechanism for control of ligand affinity. *Proc Natl Acad Sci U S A* 101: 17351-17356.
24. Boon EM & Marletta MA (2005) Ligand discrimination in soluble guanylate cyclase and the H-NOX family of heme sensor proteins. *Curr Opin Chem Biol* 9: 441-446.
25. Boon EM, Huang SH, & Marletta MA (2005) A molecular basis for NO selectivity in soluble guanylate cyclase. *Nat Chem Biol* 1: 53-59.
26. Weinert EE, Plate L, Whited CA, Olea C, Jr., & Marletta MA (2009) Determinants of ligand affinity and heme reactivity in H-NOX domains. *Angew Chem Int Ed Engl* 49: 720-723.
27. Rothkegel C, Schmidt PM, Stoll F, Schroder H, Schmidt HH, & Stasch JP (2006) Identification of residues crucially involved in soluble guanylate cyclase activation. *FEBS Lett* 580: 4205-4213.
28. Martin E, Berka V, Bogatenkova E, Murad F, & Tsai AL (2006) Ligand selectivity of soluble guanylyl cyclase: effect of the hydrogen-bonding tyrosine in the distal heme pocket on binding of oxygen, nitric oxide, and carbon monoxide. *J Biol Chem* 281: 27836-27845.
29. Derbyshire ER, Deng S, & Marletta MA (2010) Incorporation of tyrosine and glutamine residues into the soluble guanylate cyclase heme distal pocket alters NO and O_2 binding. *J Biol Chem* 285: 17471-17478.
30. Olea C, Boon EM, Pellicena P, Kuriyan J, & Marletta MA (2008) Probing the function of heme distortion in the H-NOX family. *ACS Chem Biol* 3: 703-710.
31. Pellicena P, Karow DS, Boon EM, Marletta MA, & Kuriyan J (2004) Crystal structure of an oxygen-binding heme domain related to soluble guanylate cyclases. *Proc Natl Acad Sci U S A* 101: 12854-12859.
32. Ma X, Sayed N, Beuve A, & van den Akker F (2007) NO and CO differentially activate soluble guanylyl cyclase via a heme pivot-bend mechanism. *EMBO J* 26: 578-588.
33. Zhang Y, Lu M, Cheng Y, & Li Z (2010) H-NOX domains display different tunnel systems for ligand migration. *J Mol Graph Model* 28: 814-819.
34. Marassio G, Prange T, David HN, Sopkova-de Oliveira Santos J, Gabison L, Delcroix N, Abraini JH, & Colloc'h N (2011) Pressure-response analysis of

anesthetic gases xenon and nitrous oxide on urate oxidase: a crystallographic study. *FASEB J* 25: 2266-2275.
35. Bondi A (1964) van der Waals Volumes and Radii. J. Phys. Chem. 68: 441-451.
36. Quillin ML, Breyer WA, Griswold IJ, & Matthews BW (2000) Size versus polarizability in protein-ligand interactions: binding of noble gases within engineered cavities in phage T4 lysozyme. *J Mol Biol* 302: 955-977.
37. Beneš P, Chovancová E, Kozlíková B, Pavelka A, Strnad O, Brezovský J, Šustr V, Klvaňa M, Szabó T, Gora A*, et al.* (2010) CAVER 2.1, software.
38. Emsley P & Cowtan K (2004) Coot: model-building tools for molecular graphics. *Acta Crystallogr D Biol Crystallogr* 60: 2126-2132.
39. Abraham DJ & Leo AJ (1987) Extension of the fragment method to calculate amino acid zwitterion and side chain partition coefficients. *Proteins* 2: 130-152.
40. Tsai AL, Berka V, Martin F, Ma X, van den Akker F, Fabian M, & Olson JS (2010) Is *Nostoc* H-NOX a NO sensor or redox switch? *Biochemistry* 49: 6587-6599.
41. Tannenbaum SR & White FM (2006) Regulation and specificity of S-nitrosylation and denitrosylation. *ACS Chem Biol* 1: 615-618.
42. Rohlfs RJ, Mathews AJ, Carver TE, Olson JS, Springer BA, Egeberg KD, & Sligar SG (1990) The effects of amino acid substitution at position E7 (residue 64) on the kinetics of ligand binding to sperm whale myoglobin. *J Biol Chem* 265: 3168-3176.
43. Getzoff ED, Cabelli DE, Fisher CL, Parge HE, Viezzoli MS, Banci L, & Hallewell RA (1992) Faster superoxide dismutase mutants designed by enhancing electrostatic guidance. *Nature* 358: 347-351.
44. Karow DS, Pan D, Tran R, Pellicena P, Presley A, Mathies RA, & Marletta MA (2004) Spectroscopic characterization of the soluble guanylate cyclase-like heme domains from *Vibrio cholerae* and *Thermoanaerobacter tengcongensis*. *Biochemistry* 43: 10203-10211.
45. Winter MB, McLaurin EJ, Reece SY, Olea C, Jr., Nocera DG, & Marletta MA (2010) Ru-porphyrin protein scaffolds for sensing O_2. *J Am Chem Soc* 132: 5582-5583.
46. Soltis SM, Stowell MHB, Wiener MC, Phillips GN, & Rees DC (1997) Successful flash-cooling of xenon-derivatized myoglobin crystals. *J Appl Crystallogr* 30: 190-194.
47. Otwinowski A & Minor W (1997) Processing of X-ray diffraction data collected in oscillation mode. *Methods Enzymol* 276: 307-326.
48. McCoy AJ, Grosse-Kunstleve RW, Storoni LC, & Read RJ (2005) Likelihood-enhanced fast translation functions. *Acta Crystallogr D Biol Crystallogr* 61: 458-464.
49. Lamzin VS, Perrakis A, & Wilson KS (2001) in International Tables for Crystallography, eds. Rossmann MG & Arnold E (Kluwer Academic Publishers, Dordrecht, Netherlands), pp. 720-722.
50. Adams PD, Grosse-Kunstleve RW, Hung LW, Ioerger TR, McCoy AJ, Moriarty NW, Read RJ, Sacchettini JC, Sauter NK, & Terwilliger TC (2002) PHENIX: building new software for automated crystallographic structure determination. *Acta Crystallogr D Biol Crystallogr* 58: 1948-1954.

51. Davis IW, Leaver-Fay A, Chen VB, Block JN, Kapral GJ, Wang X, Murray LW, Arendall WB, 3rd, Snoeyink J, Richardson JS*, et al.* (2007) MolProbity: all-atom contacts and structure validation for proteins and nucleic acids. *Nucleic Acids Res* 35: W375-383.
52. Laskowski RA, MacArthur MW, Moss DS, & Thornton JM (1993) PROCHECK: A program to check the stereochemical quality of protein structures. *J Appl Crystallogr* 26: 283-291.
53. Dempsey JL, Winkler JR, & Gray HB (2010) Kinetics of electron transfer reactions of H2-evolving cobalt diglyoxime catalysts. *J Am Chem Soc* 132: 1060-1065.
54. Stone JR & Marletta MA (1995) The ferrous heme of soluble guanylate cyclase: Formation of hexacoordinate complexes with carbon monoxide and nitrosomethane. *Biochemistry* 34: 16397-16403.
55 Stone JR & Marletta MA (1994) Soluble guanylate cyclase from bovine lung: Activation with nitric oxide and carbon monoxide and spectral characterization of the ferrous and ferric states. *Biochemistry* 33: 5636-5640.

CHAPTER 3

DEVELOPING LUMINESCENT PORPHYRIN-SUBSTITUTED H-NOX PROTEINS FOR BIOLOGICAL O_2 SENSING*

Summary

To probe the influence of O_2 accessibility on sGC function, a strategy is developed in this chapter to incorporate O_2-sensing porphyrins into heme proteins. To our initial surprise, the proteins displayed promising O_2-sensing properties for use in future biological imaging applications. Therefore, the development of these protein agents is discussed here within the broader context of detecting O_2 in biology.

Introduction

Motivation for biological O_2 sensing. The ability to determine physiological O_2 levels in real-time is important for profiling the metabolism of tissues and cells (1, 2). Measuring O_2 levels is critical for assessing patient health during rapid blood gas monitoring (3) and examining cellular responses to hypoxia in order to better understand mechanisms of physiological O_2 regulation (4). In addition, determining O_2 levels in tumors is also critical for advancing cancer diagnosis and therapy (2). The heterogeneous, dynamic O_2 gradients in tumors, for example, complicate the implementation of current treatment strategies, which function optimally at different amounts of O_2. A detailed knowledge of changing local O_2 levels throughout all stages of tumor development is therefore needed to assist in establishing the appropriate therapeutic window (2).

Traditional methods for sensing O_2 such as electrodes (5) or positron emission tomography (PET) (6) are invasive, expensive, and/or lack sufficient spatio-temporal resolution to profile real-time changes in O_2 levels in complex physiological environments. Quenching of small molecule luminescence by O_2 provides a platform for low cost, non-invasive imaging of *in vivo* O_2 concentrations (7). In addition, small molecule luminescence has been utilized for photodynamic therapy (PDT) to treat certain

*The worked described in this chapter was done in collaboration with Emily J. McLaurin, Ph.D. in Prof. Daniel G. Nocera's laboratory (MIT) and Charles Olea, Jr., Ph.D. in Prof. Michael A. Marletta's laboratory (UC Berkeley). E.J.M. measured emission lifetimes and conducted quantum dot experiments. C.O. collected X-ray diffraction data and solved the Ru *Tt* H-NOX crystal structure. Studies on Pd *Tt* H-NOX at UC Berkeley were carried out with the assistance of Karla M. Ramos-Torres, a visiting undergraduate from the University of Puerto Rico, as part of the Amgen Scholars Program. Our initial work on the Ru-containing proteins led to the following publication: Winter MB, McLaurin, EJ, Olea C, Jr., Reece SY, Nocera DG, Marletta MA (2010) Ru-Porphyrin Protein Scaffolds for Sensing O_2. *J Am Chem Soc* 132: 5582-5583.

cancers by sensitizing the production of cytotoxic reactive oxygen species (ROS) (8). Small molecule luminescence therefore serves as a dual means to both detect O_2 in tumors and kill tumor cells. Unfortunately, the utility of luminescent small molecules, such as porphyrins, for biological applications has been hampered by lack of targetable delivery, non-specific binding, self-aggregation, and limited photophysical properties (8, 9). Incorporation of luminescent porphyrins into hemoprotein scaffolds provides a novel platform to address these issues.

Protein-based O_2 sensors as solution. Proteins that natively bind heme are under-utilized scaffolds for porphyrin-based tools in biology (10, 11). Porphyrins have broad applications, ranging from dyes in solar cells (12) to sensitizers for radiotherapy (13) to frameworks for catalysis (14). Traditional methods for unnatural porphyrin incorporation into hemoproteins have limited their utility as biological tools. Harsh, denaturing conditions are typically required to remove native heme from proteins (15), dramatically decreasing the number of viable protein constructs (16). The Marletta laboratory recently reported a novel method for incorporation of unnatural porphyrins into hemoproteins during protein expression (16). Here, this expression-based method is used to develop protein-based sensors, in which the native heme cofactor of different hemoprotein scaffolds has been substituted with luminescent porphyrins for O_2 sensing within biological contexts.

Experimental Procedures

Preparation of RuMP and PdMP. Synthesis and all subsequent manipulations of Ru^{II}(CO) mesoporphyrin IX (RuMP) (17) and Pd^{II} mesoporphyrin IX (PdMP) (18) were carried out in low light. RuMP and PdMP were prepared through modification of published methods. For RuMP, $Ru_3(CO)_{12}$ (180 mg, 0.282 mmol) and mesoporphyrin IX dihydrochloride (60 mg, 0.094 mmol) were refluxed, under N_2, in ~30 mL glacial acetic acid for 24-36 h. For PdMP, $PdCl_2$ (80 mg, 0.45 mmol) and mesoporphyrin IX dihydrochloride (100 mg, ~0.15 mmol) were refluxed, under N_2, in ~10 mL DMF for several hours. Reaction progress was monitored by UV-vis spectroscopy. Products were cooled in an ice bath, precipitated through the dropwise addition of chilled ddH_2O, and collected on Whatman grade 42 filter paper (55 mm, Whatman International Ltd.). The products then were washed with several volumes of chilled ddH_2O or ether and dried overnight under house vacuum. ESI-MS Calcd. (Found): $[M - H]^-$ 693.2 (693.2) and 669.2 (669.2) for RuMP and PdMP, respectively.

Plasmids for protein expression. The gene for *Tt* H-NOX (residues 1-188 of *Tt*Tar4H from *Thermoanaerobacter tengcongensis*) was PCR amplified from an expression plasmid for insertion into the pCW vector. The construct for Pd *Tt* H-NOX contained a C-terminal His_6 tag. The mouse Mb construct in the pCW plasmid was used as described previously (16). Sequencing of all constructs was carried out by Elim Biopharmaceuticals, Inc.

Protein expression and incorporation of RuMP and PdMP. A modified method for unnatural porphyrin incorporation was used to express *Tt* H-NOX and Mb (16). Overnight cultures of RP523 *E. coli* cells were grown anaerobically in Hungate tubes (Bellco Glass, Inc.) as described,[5] except antibiotic selection was carried out with 75 μg/mL ampicillin. TB media (9 L) containing ampicillin was sparged overnight in a 10 L fermentor vessel with house N_2 gas that had been passed through a 0.22 μm filter (Millipore). Sterile 0.2% D-(+)-glucose was added to the media immediately prior to inoculation with the overnight culture. The expression culture was grown at 37 ^{o}C to an OD_{600} of 0.8-1.0 in the fermentor vessel while being continuously sparged with N_2. The media was then cooled to 25 ^{o}C and the fermentor was covered in aluminum foil before the addition of 3-6 μg/mL porphyrin (from a ~200X stock in DMSO). Expression was induced with 1 mM IPTG, and induction was allowed to occur for 18-22 h at room temperature while the culture was continuously sparged with N_2. *E. coli* pellets were harvested in the dark and either stored at –80 ^{o}C following centrifugation or lysed directly for protein purification.

Purification of Ru Tt H-NOX, Pd Tt H-NOX His$_6$, and Ru Mb His$_6$. Purification of *Tt* H-NOX (19) and Mb (16) were carried out as described previously but with some modifications. All manipulations of Ru *Tt* H-NOX and Ru Mb during the purification were performed in the dark and/or behind aluminum foil.

For Ru *Tt* H-NOX, cell pellets (from 9 L of *E. coli* expression) were slowly thawed using warm water and re-suspended in ~100 mL of buffer A (50 mM TEA, pH 7.5, 50 mM NaCl), which also contained 1 mM Pefabloc and DNase I. The resuspended cells were lysed 3 times with an EmulsiFlex-C5 homogenizer (Avestin, Inc.) at 4 ^{o}C between 50,000 and 150,000 psi. The lysate was then heat-denatured at 70 ^{o}C for 30 min using a water bath. All further manipulations were carried out at 4 ^{o}C. The lysate underwent centrifugation with an Optima XL-100K ultracentrifuge (Beckman Coulter, Inc.) for 1 h at 42,000 rpm. The supernatant was passed at 2 mL/min over a Toyopearl SuperQ-650M anion exchange column (Tosoh Bioscience GmbH) that had been equilibrated with buffer A. The flow-through was concentrated to ~5 mL in a Vivaspin 20 10,000 MWCO PES spin concentrator (Sartorius Stedim Biotech). The protein (~2.5 mL per run) was exchanged into buffer B (50 mM HEPES, pH 6.2, 5% glycerol) by gravity using a ~100 mL Sephadex G-25 column. The protein was then applied at 0.5 mL/min to a Toyopearl CM-650M cation exchange column (Tosoh Bioscience GmbH) that had been equilibrated with buffer B. The column was washed at 0.5 mL/min with buffer B until the absorbance at 280 nm was steady. The protein was eluted with a NaCl gradient from 0% to 40% buffer C (50 mM HEPES, pH 6.2, 500 mM NaCl, 5% glycerol) over 90 mL while 2 mL fractions were collected. Fractions 25-40 were pooled and concentrated to less than 1 mL using a 10,000 MWCO spin concentrator. Finally, the concentrated protein underwent size-exclusion chromatography with a HiLoad 26/60 Superdex 75 column (GE Healthcare) that had been equilibrated with buffer A. The protein was separated with an isocratic flow of buffer A at 0.4 mL/min while 4 mL fractions were collected. Fractions 52-58 were pooled and concentrated with a 10,000 MWCO spin concentrator. Protein was stored at –80 ^{o}C. The yield of Ru *Tt* H-NOX was ~5 mg/L of *E. coli* expression. Purity was estimated to be >90% by Coomassie stain

following SDS-PAGE. All mass spectra were recorded at the QB3/Chemistry Mass Spectrometry Facility at the University of California, Berkeley. ESI-MS for intact Ru *Tt* H-NOX Calcd. (Found): 22,012.4 (22,012). Purity of RuMP in isolated Ru *Tt* H-NOX was found to be 99% following protein denaturation by reversed phase HPLC (reported as percent of total peak area at 393 nm).

For Pd *Tt* H-NOX His_6, cell pellets were treated as described above. The supernatant following ultracentrifugation was applied to a Co column at 1-2 mL/min equilibrated with buffer A. The column was washed with ~10 column volumes of buffer A, followed by ~10 column volumes of buffer A containing 10 mM imidazole at 2 mL/min. The protein was eluted with buffer A containing 150 mM imidazole at 2 mL/min. The flow-through was concentrated using a 5,000 MWCO spin concentrator and stored in small aliquots at –80 ^{o}C. The yield of Pd *Tt* H-NOX was ~7 mg/L of *E. coli* expression. Purity was estimated to be >95% by Coomassie stain following SDS-PAGE. ESI-MS for intact *Tt* H-NOX His_6 Calcd. (Found): 23,078.0 (23,077).

For Ru Mb His_6, all manipulations were carried out at 4 ^{o}C or on ice. Cell pellets (from 9 L of *E. coli* expression) were slowly thawed and re-suspended in ~100 mL of buffer D (50 mM sodium phosphate, pH 8.0, 200 mM NaCl, 1 mM benzamidine hydrochloride), which also contained 1 mM Pefabloc and DNase I. The resuspended cells underwent homogenization and centrifugation as described above. The supernatant was applied at 0.5 mL/min to a Ni-NTA Superflow column (Qiagen) that had been equilibrated with buffer D. The column was washed at 0.5 mL/min with buffer D containing 25 mM imidazole until the absorbance at 280 nm was constant. The protein was then eluted at 0.5 mL/min with buffer D containing 250 mM imidazole. The eluate was concentrated to ~3 mL using a Vivaspin 20 3,000 MWCO PES concentrator and loaded onto the size-exclusion column described above. The protein was separated with an isocratic flow of buffer E (100 mM HEPES, pH 7.5, 50 mM NaCl) at 0.4 mL/min and 4 mL fractions were collected. Fractions 53-57 were combined and diluted ~10-fold into buffer F (20 mM Tris, pH 8.0). The protein was then flowed at 5 mL/min over a POROS HQ/20 (10 × 100) anion exchange column (Applied Biosystems) equilibrated with buffer F. The eluate was concentrated and stored at –80 ^{o}C. The yield of Ru Mb was 0.5-1.0 mg/L of *E. coli* expression. Purity was estimated to be >90% by Coomassie stain following SDS-PAGE. ESI-MS for intact Ru Mb Calcd. (Found): 17,892.5 (17,891). Purity of RuMP in isolated Ru Mb was found to be 96-99% (determined as above).

Crystallization of Ru Tt H-NOX. All crystallization experiments for Ru *Tt* H-NOX were carried out in low light. Protein was exchanged into buffer G (20 mM TEA, pH 7.5) using a PD-10 column and then concentrated to ~50-60 mg/mL using a Vivaspin 500 5,000 MWCO PES spin concentrator. Crystals were grown using sitting drop vapor diffusion in which 1 μL of the protein was mixed with 1 μL of reservoir solution and equilibrated against a 700 μL reservoir of 24% (w/v) PEG 3350 and 0.1 to 0.2 M lithium acetate at 20 ^{o}C. Crystals appeared within 24 h. Cryoprotection was achieved by titrating glycerol into the drop reservoir until a final concentration of 12.5% (v/v) was reached. The crystals were flash frozen in liquid N_2 for storage.

X-ray data collection and structure refinement of Ru Tt H-NOX. X-ray diffraction data were collected for the Ru *Tt* H-NOX crystals using synchrotron radiation at Beamline 8.3.1 at the Advanced Light Source, Lawrence Berkeley National Laboratory (Berkeley, CA). Diffraction images were collected at 100 K with 1 s exposure times and 1^{o} oscillation per frame. Data were processed using the HKL2000 suite (20) and molecular replacement was performed using Phaser (21) with PDB 1U55 as the search model. Model building was carried out using Coot (22) and refined using Phenix (23). The porphyrin ligand was refined using ruthenium mesoporphyrin as the model. The final Ru *Tt* H-NOX structure was refined to a R_{work} of 20.4% (R_{free} of 22.5%) at 2.00 Å resolution. Root mean square deviation (rmsd) was calculated using CNS (24) with Ru *Tt* H-NOX and PDB 1U55 (molecule B). Coordinates are deposited in the RCSB Protein Data Bank as entry **3M0B**.

Steady-state spectral characterization. Absorbance and emission measurements were carried out at room temperature in buffer H. UV-visible absorption spectra were acquired on a Cary 3E, 300, or 5000 spectrophotometer (Varian). Steady-state emission spectra were recorded on an automated Photon Technology International (PTI) QM 4 fluorimeter equipped with a 150-W Xe arc lamp and a Hamamatsu R928 photomultiplier tube. Sample excitation was carried out at 550 nm.

Relative quantum yields of samples, Φ_{sam}, were calculated using $[Ru^{II}(bpy)_3](PF_6)_2$ in water (for Ru *Tt* H-NOX and Ru Mb), and rhodamine 6G (R6G) or Rhodamine 101 (R101) in water (for Pd *Tt* H-NOX) as the reference according to:

$$\Phi_{sam} = \Phi_{ref}\left(\frac{A_{ref}}{A_{sam}}\right)\left(\frac{I_{sam}}{I_{ref}}\right)\left(\frac{\eta_{sam}}{\eta_{ref}}\right)^2$$

where A is the measured absorbance, η is the refractive index of the solvent, I is the integrated emission intensity, and Φ_{ref} is the emission quantum yield of the reference (25). Φ_{ref} was 0.053 for $Ru(bpy)_3^{2+}$, 0.90 for R6G, and 1.0 for R101 in water (26-28).

Time-resolved emission measurements. Time-resolved emission measurements were made with pump light provided by the third harmonic (355 nm) of a Quanta-Ray Nd:YAG laser (Spectra-Physics) running at 10 Hz. The pump light was passed through a BBO crystal yielding a visible frequency that was tuned to 550 nm and employed to excite samples. All lifetime values were collected in triplicate. Anaerobic protein samples were obtained by exchanging the protein into anaerobic buffer H using a PD-10 column while inside a glove bag (Coy Laboratory Products Inc.) maintained at 4 ^{o}C. Samples were brought into the glove bag following 2 series of the following cycles: vacuum (20-25 inHg), Ar, vacuum, Ar, vacuum, 90:10 high purity Ar:H_2 gas mixture. All gasses were purchased from Airgas. The proteins were kept anaerobic in a septum-sealed quartz cuvette. Aeration was achieved through slow addition of air to the sample followed by equilibration through careful mixing. O_2 values were quantified using a fiber optic O_2 sensing system (Ocean Optics) equipped with a ruthenium-based probe (FOXY).

Time-resolved emission data for Ru *Tt* H-NOX, Ru Mb, and Pd *Tt* H-NOX were analyzed according to the Stern-Volmer equation for O_2 quenching:

$$\frac{\tau_0}{\tau} = 1 + k_q \tau_0 [O_2]$$

where τ_0 is the excited state lifetime in the absence of O_2, τ is the excited state lifetime at a certain O_2 concentration, and k_q is the bimolecular quenching constant (25).

The precision in the O_2 measurement can be estimated from the instrument error associated with the τ_0 value (± 2.5%). The error in the measured $[O_2]$ is determined from the following equation:

$$precision = \pm [O_2] = \frac{1}{k_q}\left(\frac{1}{\tau} - \frac{1}{\tau_0}\right)$$

where τ is the lifetime with the smallest measureable difference (2.5%) from τ_0 and k_q is the quenching constant determined from the Stern-Volmer equation.

RuMP-protein stochiometry. For RuMP-protein stochiometry, porphyrin content was quantified with both UV-visible spectroscopy and reverse phase HPLC. Protein was quantified by the method of Bradford (29) and the absorbance at 280 nm (ε = 30.9 $mM^{-1}cm^{-1}$ for *Tt* H-NOX and 14.0 $mM^{-1}cm^{-1}$ for Mb).

The porphyrin molar absorptivity in Ru *Tt* H-NOX and Ru Mb was obtained with UV-visible spectroscopy following denaturation of the proteins in 10:3:17 (v/v) pyridine : 1M NaOH : H_2O. RuMP was used to generate a standard curve (ε = 195 $mM^{-1}cm^{-1}$ at 396 nm in pyridine/NaOH solution) (30).

Porphyrin content of the isolated proteins was also measured using HPLC on a System Gold chromatograph (Beckman Coulter, Inc.). The LC was equipped with a 126 NMP Solvent Module, a diode array 168 NM Detector, and a Vydac C4 column (5 μm, 4.6 mm × 250 mm). The RuMP-containing proteins (20-100 μM) were prepared in buffer H and manually injected in 20 μL volumes. Solvent A was 0.1% TFA/99.9% water and solvent B was 0.05% TFA/99.95% acetonitrile. The elution profile consisted of a linear gradient from 0% to 100% solvent B over 20 min, isocratic conditions at 100% B for 5 min, a linear gradient to 0% B over 5 min, and finally isocratic conditions at 0% B for 10 min at a flow rate of 1.0 mL/min. The peak area at 393 nm for the major eluting species (16.4 min retention time, 96-99% of total peak area) was integrated using 32 Karat software (version 7.0, Beckman Coulter, Inc.). Ru Mb was used to generate a standard curve (ε = 197 $mM^{-1}cm^{-1}$ at 397 nm in buffer) (30).

Plasma stability of Ru and Pd Tt H-NOX. Stability of Ru *Tt* H-NOX in mouse plasma was assessed by a modification of established methods (31). Purified Ru *Tt* H-NOX (1.5 mg/mL) was exchanged into DPBS using a PD-10 desalting column (GE Healthcare). The protein was incubated in equal volume mouse plasma at 37 ^oC in the

dark. Plasma control samples containing equal volume DPBS in place of Ru *Tt* H-NOX (for background absorbance correction) were prepared in parallel. Samples were centrifuged at various time points (0, 4, 10, and 24 h) at 2,800 rpm for 5 min in a Beckman GS-6R centrifuge maintained at 4 ^{o}C. An absorption spectrum was acquired of the supernatant for each sample. For Pd *Tt* H-NOX, plasma stability was conducted in a manner similar to that described above, except time points were taken at 0, 1, 3.5, 6.5, and 24 h.

Quantum dot-Pd Tt H-NOX. Experimental details for H-NOX–quantum dot (QD) conjugation and characterization of the resulting complex have been described (32).

Results and Discussion

Building Ru-porphyrin protein scaffolds. Ruthenium(II) CO mesoporphyrin IX (RuMP) (**Figure B.1**) is an ideal cofactor for protein-based sensors because it exhibits O_2-senstive phosphorescence (33) and presents a proximal axial ligation site (17) to facilitate binding to the protein scaffold. Myoglobin (Mb) and the H-NOX (Heme Nitric oxide / OXygen binding) domain from the thermophilic bacterium *Thermoanaerobacter tengcongensis* (*Tt* H-NOX) are robust proteins for RuMP sensors, as they can be readily modified with genetically-encoded affinity tags and site-directed mutagenesis (10, 34). In addition, *Tt* H-NOX is stable under extreme temperatures (>70 °C) (34).

Experimental details for preparation and characterization of RuMP-substituted Mb (Ru Mb) and *Tt* H-NOX (Ru *Tt* H-NOX) are described in the Experimental Procedures. Briefly, RuMP was synthesized in a manner similar to published methods (17) and incorporated into Mb and *Tt* H-NOX during anaerobic protein expression. The

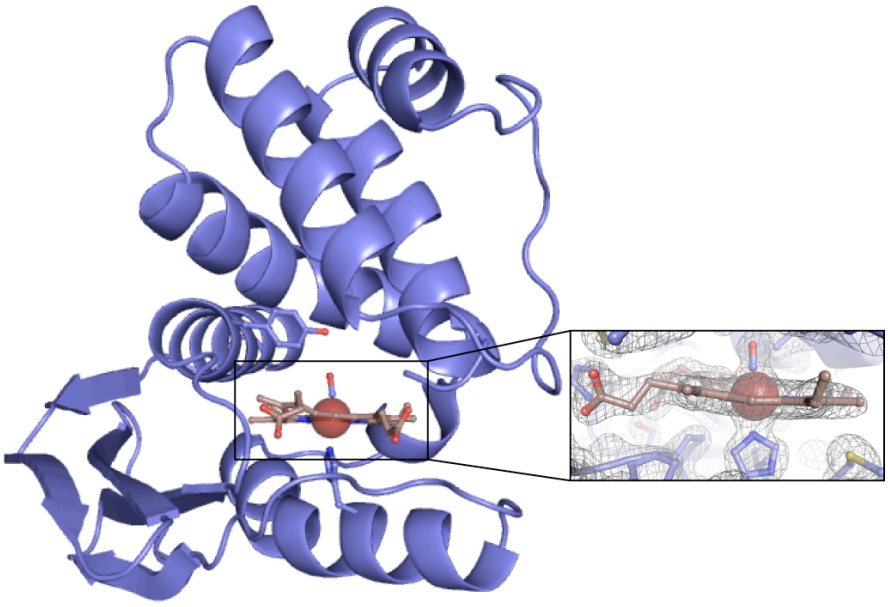

Figure 3.1 Crystal structure of *Tt* H-NOX containing RuMP solved at 2.00 Å resolution. $2F_o–F_c$ electron density map calculated by omitting RuMP and the proximal histidine side chain (inset).

RuMP-substituted proteins were isolated containing a stochiometric amount of porphyrin (**Table B.1**). Indeed, further evaluation of the stability of Ru *Tt* H-NOX indicated no detectible porphyrin loss for >24 hours under biological conditions (mouse plasma at 37 °C, **Figure B.2**).

Purified Ru *Tt* H-NOX was crystallized to verify proper porphyrin insertion and preservation of the protein fold. The high-resolution (2.00 Å) structure of Ru *Tt* H-NOX (**Figure 3.1**, **Table B.2**) is the first crystal structure of a Ru porphyrin bound to a protein and demonstrates that the unnatural porphyrin maintains key contacts with surrounding heme pocket residues. These contacts include coordination of the proximal histidine to Ru and hydrogen bonding between the distal porphyrin ligand and a tyrosine residue (**Figures 3.1 and 3.2**). In fact, comparison of heme-bound *Tt* H-NOX with its Ru analogue indicates little perturbation of the protein fold (overall rmsd 1.3 Å, **Figure B.3**).

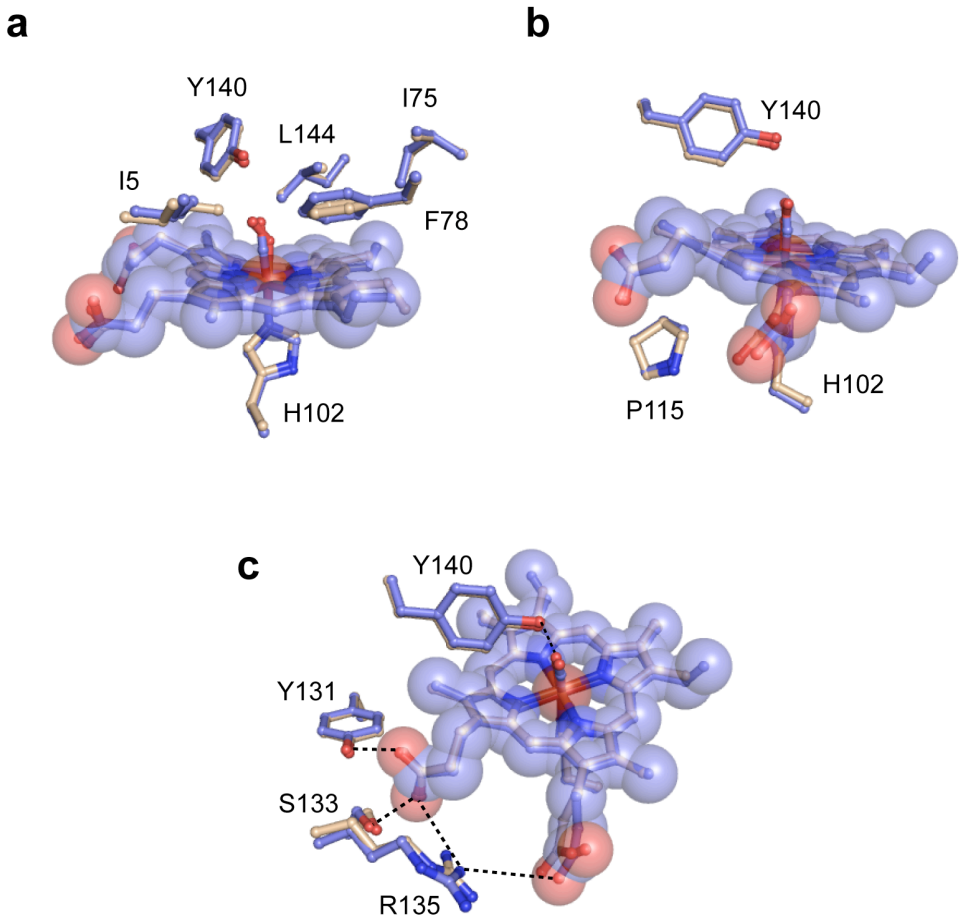

Figure 3.2 Overall alignment showing heme pocket residues of Ru *Tt* H-NOX (—) and *Tt* H-NOX bound to its native heme as an Fe^{II}–O_2 complex (molecule B, PDB 1U55) (—). Van der Waals contacts are maintained **(a)** between the unnatural porphyrin and I5, I75, F78, and L144 in the distal pocket as well as **(b)** with P115 in the proximal pocket. **(c)** Hydrogen bonding interactions (dashed lines) are conserved between Y140 and the distal porphyrin ligand (CO or O_2) as well as between the porphyrin propionate groups and Y131, S133, and R135. Only the hydrogen bonding interactions for the Ru *Tt* H-NOX structure are shown for clarity.

Steady-state and time-resolved spectroscopies were employed to examine the spectral properties of RuMP bound to the protein scaffolds. UV-visible spectra for Ru *Tt* H-NOX and Ru Mb show similar Soret band features at 400 nm and 397 nm, respectively (**Figure 3.3**, **Table 3.1**). However, the α band at ~550 nm for Ru Mb is split, as observed previously (17). Steady-state emission spectra reveal a blue-shifted emission band and decreased emission quantum yield for Ru Mb as compared to Ru *Tt* H-NOX (Table 1). Time-resolved emission spectroscopy conducted to further probe the spectral features of the porphyrin-protein complexes yielded single-exponential emission decays (following 550 nm laser excitation) under anaerobic conditions that vary widely between the two proteins (τ_o = 7.7 μs for Ru *Tt* H-NOX vs. 37.3 μs for Ru Mb, respectively). Taken together, these data indicate a substantially different conformation and/or chemical environment for RuMP in Mb and *Tt* H-NOX. Indeed, the crystal structure of Mb reveals that the heme is partially exposed to solvent (10), whereas the heme in *Tt* H-NOX is buried within the protein matrix (**Figure 3.1**).

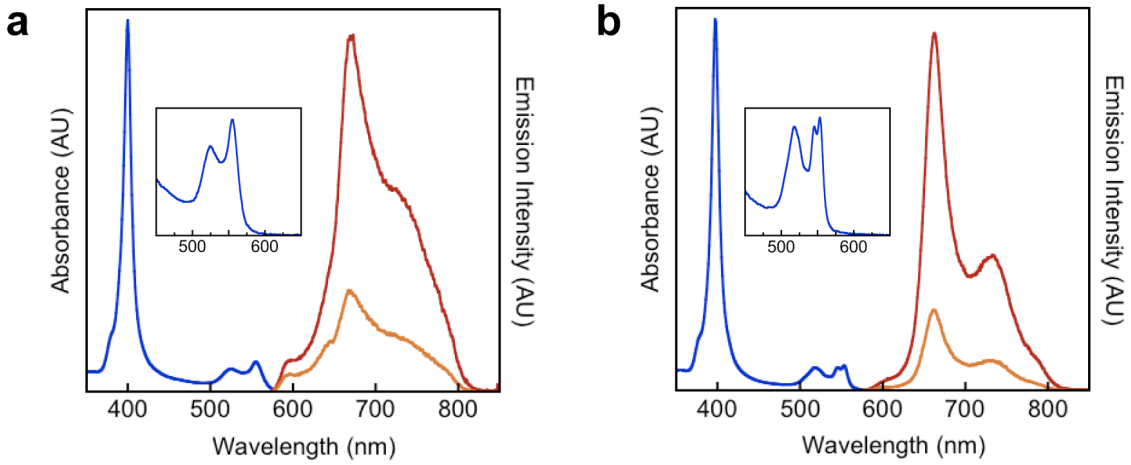

Figure 3.3 Steady-state absorbance (—) and emission spectra of Ru *Tt* H-NOX (left) and Ru Mb (right) in aqueous HEPES/NaCl buffer. Emission spectra were acquired following excitation at 550 nm in the presence (—, 256 μM) and absence (—) of O_2.

Table 3.1 Spectroscopic and photophysical properties of Ru proteins.

Ru Protein	Absorbance λ_{abs} (nm) / (ε)[a]	Emission λ_{em}[b](nm)	Quantum Yield Φ_{em}[d]	Lifetime τ_{em}[e] (μs)
Tt H-NOX	400 (173)	668	1.7 x 10^{-4}	7.7 ($-O_2$)
	524 (10.7)	~734[c]		2.9 ($+O_2$)
	555 (13.9)			
Mouse Mb	397 (197)	663	4.8 x 10^{-5}	37.3 ($-O_2$)
	518 (12.2)	~733[c]		12.2 ($+O_2$)
	553 (13.2)			

[a] $mM^{-1}cm^{-1}$. [b] λ_{ex} = 550 nm. [c] shoulder. [d] λ_{ex} = 550 nm, no O_2. [e] λ_{ex} = 550 nm, λ_{det} = 640 nm, no O_2 and 256 μM O_2.

The ability of phosphorescent molecules to sense O_2 is determined by the degree of emission quenching in the presence of O_2. Comparison of the steady-state emission spectra of Ru *Tt* H-NOX and Ru Mb measured under aerobic and anaerobic conditions reveals that O_2 appreciably quenches the emission of both proteins (**Figure 3.3**). To further evaluate the highly stable Ru *Tt* H-NOX protein as an O_2 sensor, its excited state lifetime was measured at several O_2 concentrations (**Figure 3.4**). The data were analyzed according to the Stern-Volmer (SV) equation for O_2 quenching and yielded a bimolecular quenching constant, k_q, of 1350 $mmHg^{-1}s^{-1}$ (8.2×10^8 $M^{-1}s^{-1}$). In addition to intrinsic emission properties, the precision of lifetime-based O_2 sensors is governed by the instrument error associated with the lifetime measurement. Taking our instrument error of 2.5% into account, Ru *Tt* H-NOX can be used to determine O_2 concentrations to within ±2.5 mmHg (4.2 μM) in spite of its low quantum yield. This precision is comparable to that reported for commercial O_2 sensors (**Table 3.2**) and is ideally suited for determining

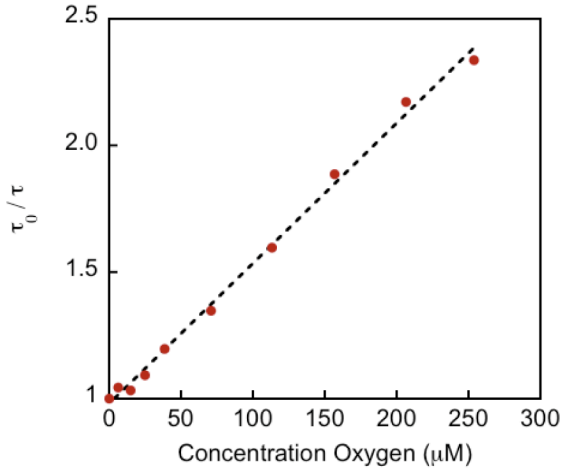

Figure 3.4 Stern-Volmer plot of the excited state lifetime of Ru *Tt* H-NOX vs. [O_2] showing linear phosphorescence quenching by O_2 from 0 to 256 μM O_2 (R^2 = 0.9957).

O_2 concentrations in biology. Indeed, emission quenching was observed to be linear across the biologically relevant range of O_2 concentrations (**Figure 3.4**).

Pd-porphyrin protein scaffolds. To improve the photophysical properties and O_2 responsiveness of the *Tt* H-NOX–based sensor, Pd(II) mesoporphyrin IX (PdMP) was incorporated into the protein scaffold during protein expression. Pd porphyrins have long emission lifetimes and high quantum yields. This allows for higher sensitivity to lower O_2 levels and decreased data acquisition times due to enhanced sensor brightness (35). Although Pd porphyrins have improved photophysical properties, they are not expected to coordinate to the protein proximal histidine residue. To decrease the likelihood of porphyrin loss during protein purification, a *Tt* H-NOX construct with a His_6 affinity tag was used for one-step purification.

Purified Pd *Tt* H-NOX was characterized with steady-state absorption and emission spectroscopies. The Pd-containing protein was found to display a Soret band feature at 395 nm and bright emission at 672 nm in the absence of O_2 (**Figure 3.5** and **Table 3.2**). Comparison to Ru *Tt* H-NOX reveals an improved quantum yield (0.025 vs. 0.00017) and steady-state emission quenching air (~30 fold vs. ~2.5 fold). Time-resolved emission spectroscopy was employed to measure the excited state lifetime of Pd *Tt* H-NOX as a function of O_2 concentration. Laser excitation of Pd *Tt* H-NOX at 550 nm resulted in a long-lived single exponential emission decay (τ_0 = 705 μs) under anaerobic conditions. A Stern-Volmer plot of the excited state lifetime versus O_2 concentration demonstrates that Pd *Tt* H-NOX displays a linear O_2 response in the physiological range (**Figure 3.5**). In addition, lifetime measurements indicate that Pd *Tt* H-NOX is capable of measuring O_2 levels with high precision (± 0.16 mmHg) (**Table 3.2**).

To evaluate the stability of Pd *Tt* H-NOX under biological conditions, the Pd-protein complex was incubated with mouse plasma for 24 h at 37 °C. No porphyrin loss was detected during this period (**Figure B.4**). Additionally, steady-state emission spectra were recorded in the presence of physiological amounts of serum albumin, which has previously been shown to modulate the emission properties of other porphyrins (35). Importantly, no change in steady-state O_2 quenching was observed up to 6% serum albumin (data not shown). Together, these findings suggest that Pd *Tt* H-NOX is a highly stable complex for measuring O_2 levels in biological environments.

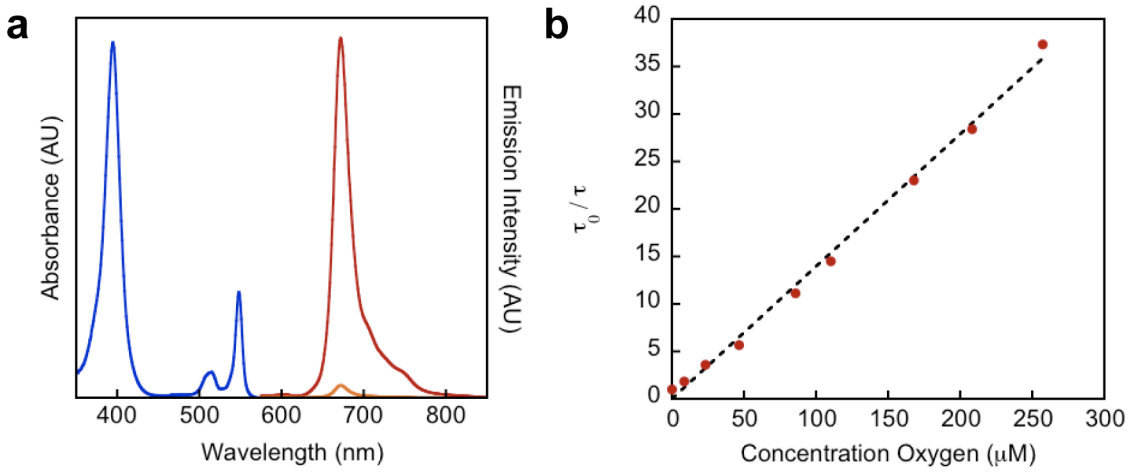

Figure 3.5 (a) Steady-state absorbance (—) and emission spectra of Pd *Tt* H-NOX in aqueous HEPES/NaCl buffer. Emission spectra were acquired following excitation at 550 nm in the presence (—, 256 μM) and absence (—) of O_2. **(b)** Stern-Volmer plot of the excited state lifetime of Pd *Tt* H-NOX vs. [O_2] showing linear phosphorescence quenching by O_2 from 0 to 256 μM O_2 (R^2 = 0.9953).

Table 3.2 Comparison of *Tt* H-NOX with select O_2 sensors.

Complex	Quenching Rate k_q ($mmHg^{-1}s^{-1}$)	Lifetime τ_0 (μs)	Precision[a] (mmHg)	Quantum Yield Φ_{em}	*Ref.*[b]
Ru *Tt* H-NOX	1350	7.7	5.0	0.00017	
Pd *Tt* H-NOX	450	705	0.16	0.025	
$Ru^{II}(bpy)_3^{2+}$	4300	0.58	21	0.053	(36)
Oxyphor	293	707	0.25	0.1	(35)
PtP-C343	150	60	5.9	0.10	(9)

[a] Determined assuming an error of 2.5% in τ_0 measurement. [b] This work unless noted.

Quantum dot-Pd Tt H-NOX. Initial efforts have been carried out in the Nocera laboratory to attach Pd *Tt* H-NOX to quantum dots (QDs) to enhance protein photophysical properties. QDs have numerous advantages for biological imaging, including high quantum yields, narrow emission line-widths, broad excitation profiles, and large two-photon absorption cross-sections (37). Energy transfer from the QD to the attached Pd *Tt* H-NOX protein allows the desirable photophysical properties of the dot to be coupled with the O_2-sensitivity of the Pd protein (**Figure 3.6**). Numerous strategies are available for protein-QD conjugation. However, for simplicity, the His_6 affinity tag of the protein was employed as an initial attachment strategy (38).

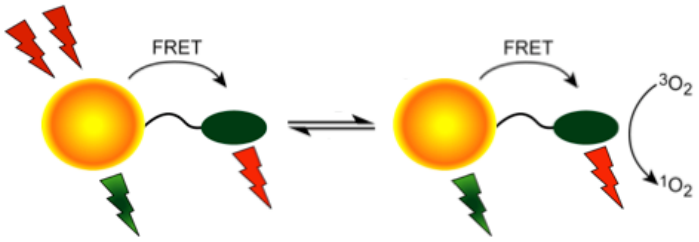

Figure 3.6 Strategy for O_2 sensing using an H-NOX–QD conjugate. Excitation of the QD (yellow) leads to energy transfer to the attached protein (green) due to its spectral overlap with the emission from the QD. The resulting excitation of the protein produces O_2-sensitive emission (phosphorescence) as described. This allows excitation of the dot to yield an O_2-sensitive response. Figure adapted from (37).

Pd *Tt* H-NOX was incubated with water-solubilized DHLA-PEG QDs (32, 39), and the protein-QD complex was purified using a desalting column. To evaluate the ability of the complex to serve as a sensor for O_2, the sample was excited at 460 nm where Pd *Tt* H-NOX minimally absorbs. In the absence of O_2, this resulted in bright emission from the quantum dot as well as enhanced protein phosphorescence (**Figure 3.7**). The phosphorescence of the protein was quenched in the presence of O_2, while the emission from the quantum dot remained unchanged, suggesting that the protein-QD conjugate may be a useful strategy for developing ratiometric O_2 sensors. The stochiometry of QD:protein was estimated to be relatively low (1:~0.1) based on the absorption spectrum of the complex (**Figure 3.7**). Therefore, improvements to QD conjugation are needed. To address this issue, we have since developed a *Tt* H-NOX His_6 construct with a C-terminal cysteine residue to facilitate conjugation using maleimide-functionalized QDs (*Tt* H-NOX has no native cysteines). The protein was purified in the presence of reducing agent (5 mM β-mercaptoethanol) and found to behave in a manner similar to the unmodified protein. This suggests that maleimide chemistry may be a viable strategy for improving the stability and stochiometry of QD conjugation.

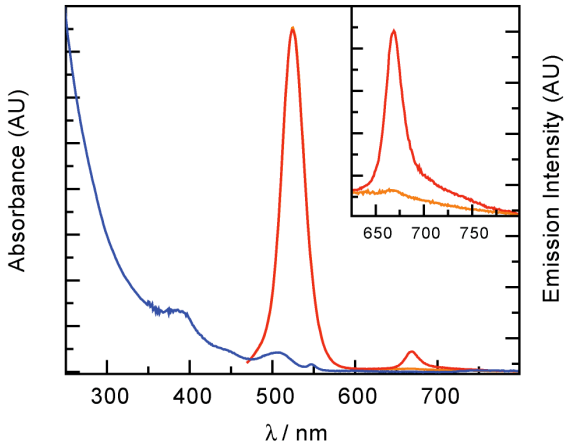

Figure 3.7 Steady-state absorbance (—) and emission spectra of QD-Pd *Tt* H-NOX. Emission spectra were acquired following excitation at 460 nm in the presence (—, 256 μM) and absence (—) of O_2. The large feature in the emission spectrum (~525 nm) is the O_2-insensitive QD emission. **(Inset)** O_2-sensitive emission from the attached Pd *Tt* H-NOX is shown. Figure courtesy of E.J.M.

Further enhancing properties for O_2 sensing. As described above, modification of the porphyrin and attachment of the protein scaffolds to imaging agents, such as QDs, are both promising strategies for improving protein photophysical properties. Additionally, the emission properties of the proteins could be tuned through structure-guided mutagenesis to change the porphyrin conformation and/or coordination environment. The biocompatibility of the sensors could be improved through modification of the protein surface with chemical means (e.g., PEGylation). Additionally, chemical and genetic strategies could be implemented to couple the proteins to various groups for targeted delivery in biological systems. Therefore, numerous approaches are available to further expand the properties of this new class of O_2 sensors. We anticipate that tuning protein properties through these strategies will facilitate the targeted and dynamic detection of dissolved O_2 in a host of complex physiological conditions.

References

1. Helmlinger G, Yuan F, Dellian M, & Jain RK (1997) Interstitial pH and pO_2 gradients in solid tumors in vivo: high-resolution measurements reveal a lack of correlation. *Nat Med* 3: 177-182.
2. Jain RK (2005) Normalization of tumor vasculature: an emerging concept in antiangiogenic therapy. *Science* 307: 58-62.
3. Mo JW & Smart W (2004) Lactate biosensors for continuous monitoring. *Front Biosci* 9: 3384-3391.
4. Guillemin K & Krasnow MA (1997) The hypoxic response: huffing and HIFing. *Cell* 89: 9-12.
5. Severinghaus JW & Astrup PB (1986) History of blood gas analysis. V. Oxygen measurement. *J Clin Monit* 2: 174-189.
6. Krause BJ, Beck R, Souvatzoglou M, & Piert M (2006) PET and PET/CT studies of tumor tissue oxygenation. *Q J Nucl Med Mol Imaging* 50: 28-43.
7. Vanderkooi JM, Maniara G, Green TJ, & Wilson DF (1987) An optical method for measurement of dioxygen concentration based upon quenching of phosphorescence. *J Biol Chem* 262: 5476-5482.
8. Berg K, Selbo PK, Weyergang A, Dietze A, Prasmickaite L, Bonsted A, Engesaeter BO, Angell-Petersen E, Warloe T, Frandsen N*, et al.* (2005) Porphyrin-related photosensitizers for cancer imaging and therapeutic applications. *J Microsc* 218: 133-147.
9. Finikova OS, Lebedev AY, Aprelev A, Troxler T, Gao F, Garnacho C, Muro S, Hochstrasser RM, & Vinogradov SA (2008) Oxygen microscopy by two-photon-excited phosphorescence. *Chemphyschem* 9: 1673-1679.
10. Dou Y, Maillett DH, Eich RF, & Olson JS (2002) Myoglobin as a model system for designing heme protein based blood substitutes. Biophys Chem 98: 127-148.
11. Gillam EM (2008) Engineering cytochrome p450 enzymes. *Chem Res Toxicol* 21: 220-231.
12. Imahori H & Fukuzumi S (2004) Porphyrin- and Fullerene-Based Molecular Photovoltaic Devices. *Adv Func Mat* 14: 525-536.

13. Vicente MG (2001) Porphyrin-based sensitizers in the detection and treatment of cancer: recent progress. Curr Med Chem Anticancer Agents 1: 175-194.
14. Chang CJ, Chng LL, & Nocera DG (2003) Proton-coupled O-O activation on a redox platform bearing a hydrogen-bonding scaffold. *J Am Chem Soc* 125: 1866-1876.
15. Teale F (1959) Cleavage of the haem-protein link by acid methylethylketone. *Biochim Biophys Acta* 35: 543.
16. Woodward JJ, Martin NI, & Marletta MA (2007) An *Escherichia coli* expression-based method for heme substitution. *Nat Methods* 4: 43-45.
17. Paulson DR, Addison AW, Dolphin D, & James BR (1979) Preparation of ruthenium(II) and ruthenium(III) myoglobin and the reaction of dioxygen, and carbon monoxide, with ruthenium(II) myoglobin. *J Biol Chem* 254: 7002-7006.
18. Cowan JA & Gray HB (1989) Synthesis and properties of metal-substituted myoglobins. *Inorg Chem* 28: 2074-2078.
19. Olea C, Boon EM, Pellicena P, Kuriyan J, & Marletta MA (2008) Probing the function of heme distortion in the H-NOX family. *ACS Chem Biol* 3: 703-710.
20. Otwinowski Z & Minor W (1997) Processing of X-ray diffraction data collected in oscillation mode. *Method Enzymol* 276: 307-326.
21. McCoy AJ, Grosse-Kunstleve RW, Storoni LC, & Read RJ (2005) Likelihood-enhanced fast translation functions. *Acta Crystallogr D Biol Crystallogr* 61: 458-464.
22. Emsley P & Cowtan K (2004) Coot: model-building tools for molecular graphics. *Acta Crystallogr D Biol Crystallogr* 60: 2126-2132.
23. Adams PD, Grosse-Kunstleve RW, Hung LW, Ioerger TR, McCoy AJ, Moriarty NW, Read RJ, Sacchettini JC, Sauter NK, & Terwilliger TC (2002) PHENIX: building new software for automated crystallographic structure determination. *Acta Crystallogr D Biol Crystallogr* 58: 1948-1954.
24. Brunger AT, Adams PD, Clore GM, DeLano WL, Gros P, Grosse-Kunstleve RW, Jiang JS, Kuszewski J, Nilges M, Pannu NS*, et al.* (1998) Crystallography & NMR system: A new software suite for macromolecular structure determination. *Acta Crystallogr D Biol Crystallogr* 54: 905-921.
25. Lakowicz JR (2006) Principles of Fluorescence Spectroscopy (Springer, New York).
26. Henderson Jr LJ & Cherry WR (1985) Selective perturbation of ligand field excited states. *J Photochem* 28: 143-151.
27. Magde D, Wong R, & Seybold PG (2002) Fluorescence quantum yields and their relation to lifetimes of rhodamine 6G and fluorescein in nine solvents: improved absolute standards for quantum yields. *Photochem Photobiol* 75: 327-334.
28. Karstens T & Kobs K (1980) Rhodamine B and rhodamine 101 as reference substances for fluorescence quantum yield measurements. *J Phys Chem* 84: 1871-1872.
29. Bradford MM (1976) A rapid and sensitive method for the quantitation of microgram quantities of protein utilizing the principle of protein-dye binding. *Anal Biochem* 72: 248-254.
30. Srivastava TS (1977) A carbon monoxide derivative of ruthenium (II) myoglobin probe of heme protein conformation. *Biochim Biophys Acta* 491: 599-604.

31. Barnikol WK, Burkhard O, Poetzschke H, Domack U, Dinkelmann S, Guth S, Fiedler B, & Manz B (2002) New artificial oxygen carriers made of pegulated polymerised pyridoxylated porcine haemoglobin (P_4Hb). C*omp Biochem Physiol A Mol Integr Physiol* 132: 185-191.
32. McLaurin EJ (2011) Dissertation in Inorganic Chemistry (Massachusetts Institute of Technology, Cambridge, MA).
33. Vanderkooi JM, Wright WW, & Erecinska M (1994) Nitric oxide diffusion coefficients in solutions, proteins and membranes determined by phosphorescence. *Biochim Biophys Acta* 1207: 249-254.
34. Boon EM & Marletta MA (2006) Sensitive and selective detection of nitric oxide using an H-NOX domain. *J Am Chem Soc* 128: 10022-10023.
35. Dunphy I, Vinogradov SA, & Wilson DF (2002) Oxyphor R2 and G2: phosphors for measuring oxygen by oxygen-dependent quenching of phosphorescence. *Anal Biochem* 310: 191-198.
36. Oter O & Ribou AC (2009) Quenching of long lifetime emitting fluorophores with paramagnetic molecules. *J Fluoresc* 19: 389-397.
37. McLaurin EJ, Greytak AB, Bawendi MG, & Nocera DG (2009) Two-photon absorbing nanocrystal sensors for ratiometric detection of oxygen. *J Am Chem Soc* 131: 12994-13001.
38. Delehanty JB, Medintz IL, Pons T, Brunel FM, Dawson PE, & Mattoussi H (2006) Self-assembled quantum dot-peptide bioconjugates for selective intracellular delivery. *Bioconjug Chem* 17: 920-927.
39. Liu W, Howarth M, Greytak AB, Zheng Y, Nocera DG, Ting AY, & Bawendi MG (2008) Compact biocompatible quantum dots functionalized for cellular imaging. *J Am Chem Soc* 130: 1274-1284.

CHAPTER 4

PROBING O_2 ACCESSIBILITY IN SOLUBLE GUANYLATE CYCLASE WITH A PHOSPHORESCENT RU PORPHYRIN*

Summary

In this chapter, the techniques developed to generate luminescent biological O_2 sensors (**Chapter 3**) are implemented to measure O_2 accessibility at the heme site in sGC. Our initial studies with a prokaryotic homologue of the sGC H-NOX domain (**Chapter 2**) have implicated the role of the protein scaffold in modulating ligand diffusion to and from the heme site in H-NOX domains. Here, these ideas are tested in the context of sGC to dissect the influence of O_2 accessibility at the heme site on the remarkable ability of the enzyme to resist oxidation in aerobic conditions.

Introduction

Nitric oxide (NO) signaling in mammals mediates numerous diverse physiological processes such as vasodilation, neurotransmission, and platelet aggregation (1-3). Soluble guanylate cyclase (sGC) is a heterodimeric hemoprotein that is ubiquitous in higher eukaryotes and a central regulator of NO signaling (4). The rapid binding of NO to the heme group of sGC increases the enzyme's rate of GTP to cGMP conversion by several hundred-fold (4). The cGMP produced by sGC initiates downstream physiological effects by binding to phosphodiesterases, cGMP-dependant protein kinases, and cGMP-gated ion channels (3).

Although sGC has the same histidyl-ligated heme cofactor as the globins with an open coordination site, sGC binds NO but has no measurable affinity for oxygen (O_2) in aerobic conditions (5). This allows sGC to efficiently trap NO in physiological contexts where O_2 is present at orders of magnitude higher concentrations (μM vs. nM) (6). Additionally, sGC is unique among histidyl-ligated heme proteins because the reduced (ferrous) oxidation state of the heme is stable in air (5). Oxidation of the sGC heme *in vitro* with chemical oxidants inhibits sGC activation by NO (7). Therefore, it has been proposed that sGC heme oxidation, under conditions of oxidative stress, contributes to NO tolerance and the development of cardiovascular disease (8-11). Thus, oxidized sGC has emerged as an important therapeutic target (8-11).

The absence of structural data on sGC has limited molecular understanding of sGC domain organization and the structural features that contribute to the unusual chemical properties of the heme. It is known that NO binding in sGC occurs at the N-

*The worked described in this chapter was done in collaboration with Emily J. McLaurin, Ph.D. in Prof. Daniel G. Nocera's laboratory (MIT). E.J.M. measured emission lifetimes.

terminus, which contains a conserved Heme Nitric oxide/OXygen binding (H-NOX) domain, and cGMP formation occurs at the C-terminal catalytic site (**Figure 4.1a**). The ability of NO to activate catalytic activity suggests that there is allosteric communication between the H-NOX and catalytic domains even though they are far apart in sequence. Indeed, converging lines of biochemical evidence have supported the hypothesis that sGC is in a closed (as exposed to extended) conformation. These data include protein footprinting studies to map domain interactions (12), the measurement of FRET distances between the sGC termini (13), and the observation of a functional interaction between the purified H-NOX and catalytic domains (14).

The full-length sGC structure has significant influence on the properties of the sGC heme. Isolable H-NOX–containing truncations (**Figure 4.1a**), for example, retain identical ligand-binding properties to full-length sGC (tight NO binding and discrimination against O_2) (15). However, these truncations have been found to rapidly oxidize in air (15). This has led to the proposal that full-length sGC provides a significant protective effect against O_2 by favoring a high redox potential and/or limiting O_2 accessibility to the heme cofactor (15-17).

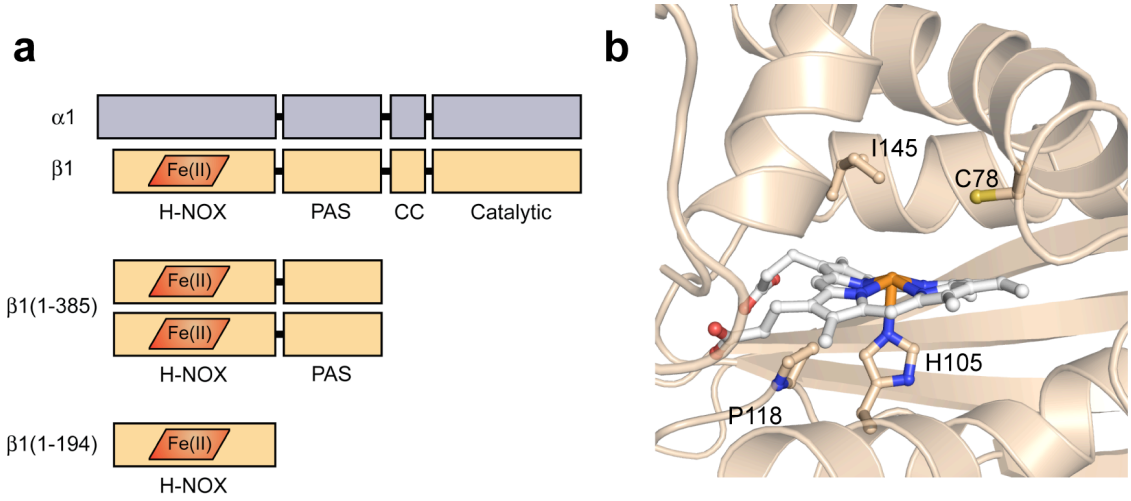

Figure 4.1 (a) Domain architecture of sGC expression constructs with the H-NOX, PAS, coiled-coil (CC), and catalytic domains shown. **(b)** Homology model of the sGC H-NOX domain. The homology model was generated using the crystal structure of *Thermoanaerobacter tengcongensis* (*Tt*) H-NOX (PDB ID 1U55). Critical residues (see **Results and Discussion**) in the predicted sGC heme pocket are labeled.

To probe the functional role of sGC structure in modulating heme properties, redox potentials and heme O_2 accessibilities were compared between the sGC H-NOX truncations and full-length sGC. Due to the inability of sGC to bind or be oxidized by O_2, Ru^{II}(CO) mesoporphyrin IX (RuMP) was encapsulated in the heme pocket in place of the native heme. RuMP displays O_2-sensitive emission, allowing the porphyrin to serve as an internal sensor for O_2 diffusion that functions independently of ligand binding (18). Together, the data support a model in which the sGC heme pocket is significantly buried in the full-length protein. We propose that this functions to decrease heme oxidation by

maintaining a high potential and hindering O_2 diffusion. These findings have broad implications for the allosteric influence of protein structure on modulating the diverse chemical properties of heme proteins.

Experimental Procedures

Plasmids for protein expression. The genes for the rat sGC heme domain constructs β1(1-194) (19) and β1(1-385) (20) were PCR amplified for insertion into the pCW plasmid. β1(1-194) contained a C-terminal His_6 tag with an RGS linker and β1(1-385) was non-tagged. Sequencing of the final constructs was carried out by Elim Biopharmaceuticals, Inc. DNA primers for PCR amplification were synthesized by Integrated DNA Technologies.

Expression of heme-containing proteins. Plasmids for protein expression were transformed into RP523 *E. coli* cells in the presence of hemin (21). Overnight cultures were grown aerobically in Luria Broth in the presence of 30 μg/mL hemin (from an ~200X stock in DMSO) and 75-100 μg/mL ampicillin (22). Expression cultures were grown at 37 °C under identical conditions, except in TB media, until an OD_{600} of ~0.6 was reached (22). Expression was induced with 1 mM IPTG, and induction was allowed to occur for 18-22 h at room temperature. *E. coli* pellets were harvested and stored at –80 °C following centrifugation (22).

Expression of RuMP-containing proteins. RuMP was prepared and incorporated into β1(1-194) and β1(1-385) during anaerobic protein expression using previously described methods (18).

Protein purification. All manipulations were carried out at 4 °C. For RuMP-containing proteins, all purification steps were also performed in the dark and/or behind aluminum foil.

For His_6-tagged β1(1-194), cell pellets were slowly thawed on ice and re-suspended in ~100 mL of buffer A (50 mM sodium phosphate, pH 8.0, 300 mM NaCl, 5% glycerol, 5 mM BME, 1 mM benzamidine), which also contained 1 mM Pefabloc and DNase I. The resuspended cells were lysed 3 times with an EmulsiFlex-C5 homogenizer (Avestin, Inc.) at 4 ^{o}C between 5,000 and 15,000 psi. The lysate underwent centrifugation with an Optima XL-100K ultracentrifuge (Beckman Coulter, Inc.) for 1 h at 42,000 rpm. The supernatent was applied to an ~5 mL Ni-NTA Superflow column (Qiagen) that had been equilibrated with buffer A. The column was washed with ~10 column volumes of buffer A, followed by ~10 column volumes of buffer A containing 25 mM imidazole. Elution was carried out with buffer A containing either 150 mM or 250 mM imidazole. The eluate was concentrated to <5 mL using a Vivaspin 20 10,000 MWCO PES spin concentrator (Sartorius Stedium Biotech). The protein then underwent size-exclusion chromatography with a HiLoad 16/60 Superdex 75 column (GE Healthcare) that had been equilibrated with buffer B (50 mM TEA, pH 7.5, 150 mM NaCl, 5% glycerol, 5 mM DTT). The protein was separated with an isocratic flow at ~0.4 mL/min while

fractions were collected. Fractions containing the highest purity protein were pooled and concentrated with a 10,000 MWCO spin concentrator. Protein was stored at –80 °C. Purity was estimated to be >90% by Coomassie stain following SDS-PAGE. All mass spectra were recorded at the QB3/Chemistry Mass Spectrometry Facility at the University of California, Berkeley. ESI-MS for intact His_6-tagged β1(1-194) Calcd. (Found): 23,501.5 (23,501).

For β1(1-385), cell pellets were slowly thawed on ice and re-suspended in ~100 mL of buffer C (50 mM DEA, pH 8.5, 25 mM NaCl, 5% glycerol, 5 mM DTT, 1 mM benzamidine), which also contained 1 mM Pefabloc and DNase I. Cell lysis and centrifugation were carried out as described above. The supernatant was loaded at 1.5 mL/min onto a ~100 mL Toyopearl SuperQ-650M anion exchange column (Tosoh Bioscience GmbH) that had been equilibrated with buffer C. The column was washed with 200 mL buffer C at 1.5 mL/min and the protein was eluted with a NaCl gradient from 0% to 100% buffer D (50 mM DEA, pH 8.5, 500 mM NaCl, 5% glycerol, 5 mM DTT) at 1.5 mL/min over 800 mL while 5 mL fractions where collected. Fractions with the highest purity β1(1-385) were pooled and concentrated in a Vivaspin 20 30,000 MWCO PES spin concentrator to ~5 mL. The protein then underwent size-exclusion chromatography with a HiLoad 16/60 or 26/60 Superdex 200 column (GE Healthcare) that had been equilibrated with buffer E (50 mM TEA, pH 7.5, 150 mM NaCl, 5% glycerol, mM DTT). The protein was separated with an isocratic flow at 0.4 mL/min while fractions were collected. Fractions containing highest purity β1(1-385) were pooled and concentrated with a 30,000 MWCO spin concentrator. The concentrated protein was diluted >5 fold in buffer F (50 mM TEA, pH 7.5, 25 mM NaCl, 5% glycerol, 5 mM DTT) and passed at 1-2 mL/min over a CM-650M cation exchange column (Tosoh Bioscience GmbH). The flow-through was collected and concentrated with 30,000 MWCO spin concentrator. If further purification of β1(1-385) was deemed necessary, the flow-through was loaded at 5 mL/min onto a POROS HQ/20 (10 x 100) anion exchange column (Applied Biosystems) that had been equilibrated with buffer F. The protein was eluted at 5 mL/min with a gradient from 0% to 100% buffer G (50 mM TEA, pH 7.5, 500 mM NaCl, 5% glycerol, 5 mM DTT) over 100 mL while fractions were collected. Fractions containing the highest purity β1(1-385) were pooled and concentrated. Protein was stored at –80 °C. Purity was estimated to be >90% by Coomassie stain following SDS-PAGE. ESI-MS for intact β1(1-385) Calcd. (Found): 44,233.5 (44,233).

Preparation of RuMP-containing sGC. Recombinant full-length sGC mutants were expressed using an Sf9/baculovirus system and purified as described previously (23). Both the β1 C78S and P118A full-length sGC mutants have been reported to be isolated with low quantities of heme (15, 24). In order to reconstitute apo sGC with RuMP, ~5 mM DTT was added to the purified sGC mutants and samples were incubated on ice in the dark for >4 h with sub-stochiometric quantities of RuMP dissolved in DMSO (final DMSO concentrations were less than 4%). RuMP incorporation was monitored by UV-visible spectroscopy at 4 °C.

Porphyrin stochiometry. For RuMP stochiometry of the purified proteins, porphyrin content was quantified with both UV-visible spectroscopy and reverse phase HPLC, and protein was quantified by the method of Bradford as described previously (18).

Heme autoxidation rates. Rates of heme oxidation (k_{ox}) for β1(1-194) and β1(1-385) were determined with UV-visible spectroscopy at 37 °C in aerobic buffer in the presence and absence of an SOD/catalase trap (25). Prior to data acquisition, the proteins were fully reduced with excess dithionite for ~10 min at 4 °C in an anaerobic chamber (Coy Laboratory Products) flushed with a 10:90 H_2/N_2 gas mixture (Praxair, Inc). Dithionite was removed by desalting on a PD10 column (GE Healthcare) with anaerobic buffer H (50 mM HEPES, pH 7.4, 20 mM NaCl, 10% glycerol). Ferrous protein (~10 μM by heme) was mixed with varying equivalents of anaerobically prepared SOD/catalase in a septum-sealed quartz cuvette. Autoxidation reactions were initiated by 10-fold dilution of the samples into aerobic buffer H (~21% O_2; 256 μM) that had been pre-equilibrated at 37 °C. UV-visible spectra were immediately recorded following equilibration of the samples through mixing (~15 s). For β1(1-194), scans were taken in the absence of trap every 1 min for 60 min or in the presence of trap every 1 min for 90 min. For β1(1-385), scans were taken in the absence of trap every 1 min for 100 min. In the presence of trap, scans were taken every 1 min for 50 min then every 2 min for an additional 150 min. Autoxidation rates were determined by fitting the change in absorbance, (dA435 –dA408) for β1(1-194) or (dA436 – dA466) for β1(1-385), versus time to a single exponential equation using Igor Pro and averaged for 3-4 independently prepared samples. Rates were found to be independent of SOD/catalase concentration in the presence of at least 0.01 molar equivalents trap (calculated based on fraction of heme-bound protein) but are reported using 5-fold higher trap concentrations (0.05 molar equivalents) to ensure full saturation of oxidation kinetics.

Redox potentials. Oxidative titrations for β1(1-385) were performed at 25 °C as described previously but with some modifications (17). Heme oxidation of a 3.5 mL solution of protein was carried out under Ar in buffer I (50 mM HEPES, pH 7.5, 50 mM KCl, 5% ethylene glycol) using anaerobically prepared 1H-(1,2,4)oxadiazolo(4,3-a)quinoxalin-1-one (ODQ) (Cayman Chemical). The spectral transition was followed from 450-750 nm with UV-visible spectroscopy, and the potential of the solution was simultaneously recorded using a platinum electrode (Ag/AgCl reference) from Radiometer Analytical (MC3051Pt-9). The protein solution contained the following redox mediators: methyl viologen (7.5 μM); anthraquinone-2-sulfonic acid (10 μM); 2-hydroxy-1,4-napthoquinone (10 μM); $Ru(NH_3)_6Cl_3$ (16.5 μM); toluylene blue (5 μM); 3'-chloroindophenol (10 μM); and *p*-benzoquinone (16.5 μM). Prior to oxidative titrations, β1(1-385) was fully reduced in the cuvette under Ar with excess anaerobically prepared sodium dithionite. Oxidative titrations were typically carried out with 1-10 μL additions of 1 or 10 mM ODQ prepared in anaerobic buffer and DMSO, respectively. A reductive titration was carried out to verify reversibility. Here, β1(1-385) was oxidized with excess ODQ and the titration was performed with dithionite prepared in anaerobic buffer as described above for ODQ. For all titrations, the potential of the solution was allowed to

stabilize for >15 min at each potential that was recorded. The midpoint potential was determined by fitting the fraction of reduced protein versus potential (volts) to the Nernst equation using Igor Pro. Data were averaged from 3 oxidative titrations carried out on different days from independently prepared samples.

Emission measurements. Steady-state emission spectra, quantum yields, and lifetime measurements were recorded at room temperature in buffer J (50 mM HEPES, pH 7.4, 50 mM NaCl) following 550 nm excitation as described previously (18). For anaerobic samples, the Ru-containing proteins were deoxygenated via desalting into buffer J in an anaerobic chamber using a PD-10 column. Aeration was achieved through slow addition of air to the samples followed by equilibration through mixing. For Stern–Volmer plots showing O_2-dependant emission quenching, varying amounts of air-saturated buffer (256 μM O_2) were added via a gas-tight syringe to anaerobically prepared protein in a septum-sealed quartz cuvette. Samples were excited at 400 nm due to limitations in protein amounts. Steady-state emission data for Stern–Volmer plots were collected in duplicate using independently prepared samples.

Results and Discussion

Autoxidation rates of the sGC heme domain constructs. The ability of the full-length sGC heme to resist oxidation in air is critical for enzyme function in aerobic cellular conditions. However, as mentioned previously, sGC H-NOX–containing truncations readily oxidize in air (15). These constructs are termed β1(1-194) (19), which contains the H-NOX domain alone, and β1(1-385) (20), which contains the H-NOX and PAS domains (**Figure 4.1a**). Due to their propensity to oxidize, these domain truncations

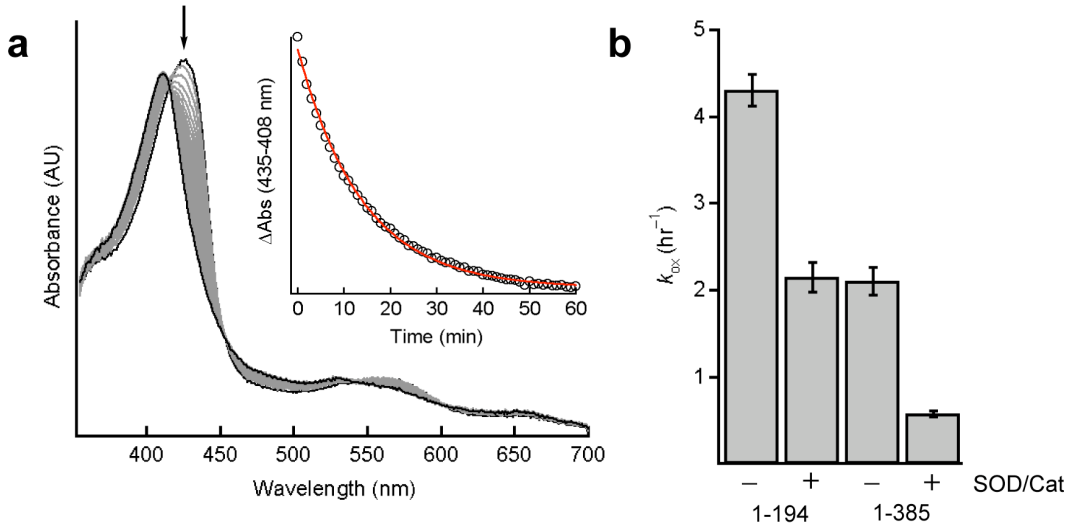

Figure 4.2 (a) Reaction of sGC heme domain constructs with O_2. **(a)** Time-resolved UV-visible spectra of β1(1-194) autoxidation in air-saturated buffer at 37 °C. **(Inset)** Change in absorbance versus time fit to a single exponential equation. **(b)** Autoxidation rates of β1(1-194) and β1(1-385) in air-saturated buffer at 37 °C in the absence and presence of a saturating SOD/catalase trap (5 %). Full-length sGC has no measurable oxidation during this time period (data not shown).

were used to probe the influence of sGC domain architecture on determinants of heme oxidation in the full-length protein. To better quantify oxidation in the presence of O_2, autoxidation rates (k_{ox}) were measured for β1(1-194) and β1(1-385) in the absence and presence of a superoxide dismutase (SOD)/catalase trap (25). An SOD/catalase trap was employed to scavenge solution reactive oxygen species (ROS) generated from the autoxidation reaction that can influence heme oxidation kinetics. Exposure of the reduced proteins to aerobic buffer (~256 μM or 21% O_2) resulted in two-state oxidation, $Fe^{II} \rightarrow Fe^{III}$, with no detectable O_2 binding (**Figure 4.2a**). As reported previously, the shorter β1(1-194) construct was found to oxidize more rapidly than β1(1-385) (15). However, the SOD/catalase trap significantly slowed the autoxidation rates of both proteins by 2–3 fold (**Figure 4.2b**). The observation that β1(1-194) oxidizes more quickly than β1(1-385) in the presence of trap confirms that differences in autoxidation kinetics between the constructs are not due to a differential effect of the oxidation products.

Table 4.1 Autoxidation rates of selected heme proteins.

Protein	**Oxidation Rate**[a] k_{ox} (hr^{-1})	***Ref.***[b]
β1(1-194)	2.15 ± 0.17[c]	
β1(1-385)	0.57 ± 0.03[c]	
sGC	n.o.	(15)
Mb[e]	0.055	(25)
Hb[f] (α chain)	0.032	(35)
Hb (β chain)	0.0037	(35)
Cyt c[g]	< 0.042[d]	(36)

[a] Measured at 37 ºC unless noted. [b] This work unless noted. [c] Measured with a 5% SOD/catalase trap. [d] Rate at 20 ºC. [e] Myoglobin. [f] Hemoglobin. [g] Cytochrome c.

Redox potential measurements. Makino and colleagues recently reported that the redox potential of full-length sGC is high (187 mV vs. SHE), consistent with the stability of the enzyme in air (17). To compare to full-length sGC, the redox potential of the sGC heme domain construct β1(1-385) was determined. The potential of β1(1-385) was obtained using a spectroelectrochemical titration under similar conditions to the full-length protein (see Experimental Procedures). Here, heme reduction and oxidation were titrated using dithionite or the heme oxidant 1H-(1,2,4)oxadiazolo(4,3-a)quinoxalin-1-one (ODQ), respectively, and the spectral transition (normalized to the fraction of reduced heme) was fit to the Nernst equation (**Figure 4.3**). Using this technique, the midpoint potential of β1(1-385) was found to be 120 ± 2 mV vs. SHE (**Table 4.2**). As a control, the potential of myoglobin was recorded under the same conditions and found to match

the previously reported value (**Table 4.2**). The reduction potential of β1(1-385) is lower than full-length sGC (Δ67 mV), and therefore, oxidation of β1(1-385) is more favorable. However, the potentials of β1(1-385) and full-length sGC are well above the O_2/O_2^- redox couple (–160 mV) (26), indicating that heme oxidation by O_2 to generate O_2^- is thermodynamically disfavored in both cases. The tendency of β1(1-385) to oxidize without binding O_2 suggests that differences in O_2 accessibility likely help contribute to the divergent heme autoxidation properties of the sGC constructs.

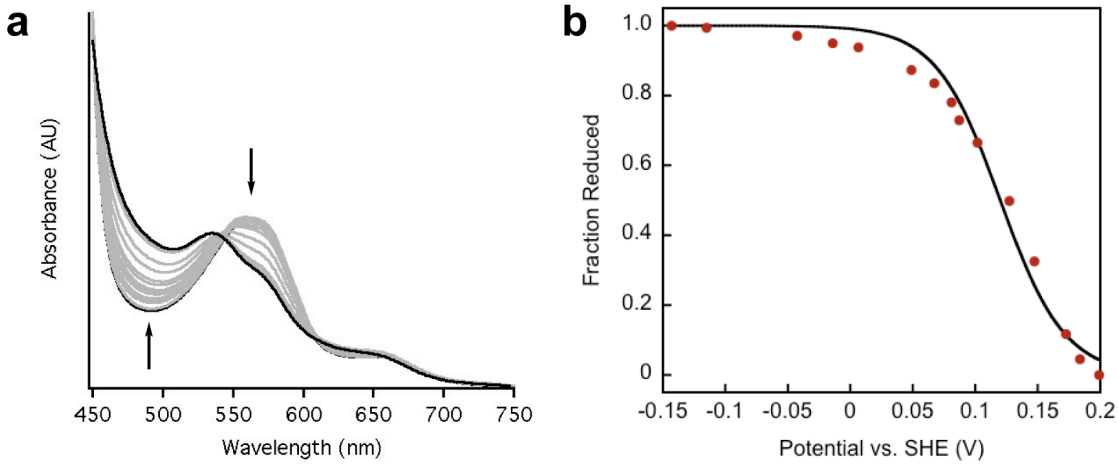

Figure 4.3 Reduction potential determination of the β1(1-385) heme Fe^{II}/Fe^{III}–OH(H) redox couple. **(a)** UV-visible spectral transition associated with heme oxidation. **(b)** Oxidative titration curve fit to the Nernst equation. Reduction potentials are reported relative to the standard hydrogen electrode (SHE). Data were collected in both the reductive and oxidative directions to demonstrate reversibility. N = 3.

Table 4.2 Reduction potentials of selected heme proteins.

Protein	Midpoint Potential $E°$ (mV)	*Ref.*[a]
β1(1-194)	N/D	
β1(1-385)	120 ± 2	
sGC[b]	187	(17)
Ms sGC-NT1[c]	241 ± 2	(37)
Mb	54	(38)
Hb	168	(39)
Cyt c	271	(36)

[a] This work unless noted. N/D = not determined due to poor sample equilibration during the titration. [b] Mammalian sGC. [c] *Manduca sexta* sGC construct (α 1–471, β 1–401).

Ru porphyrin incorporation and steady-state emission quenching. To directly measure O_2 accessibility at the sGC heme site, we sought to incorporate Ru^{II}(CO) mesoporphyrin IX (RuMP) into the sGC heme pocket (18). RuMP exhibits bright phosphorescence that is collisionally quenched by O_2, allowing the porphyrin to provide a dynamic measurement for O_2 diffusion through the protein scaffold (27, 28). As described in **Chapter 3**, RuMP was previously incorporated into the homologous H-NOX domain from *Thermoanaerobacter tengcongensis* (*Tt* H-NOX) using the expression-based strategy developed in our laboratory (**Chapter 1**) (18). A high-resolution (2.00 Å) crystal structure of RuMP-containing *Tt* H-NOX was solved (18). The structure demonstrated that RuMP incorporation did not perturb the protein fold and that RuMP bound in a manner similar to the native heme (18). Together, these observations suggest that RuMP is an ideal O_2-sensitive mimic for heme that will not significantly alter the native sGC structure.

RuMP was incorporated into β1(1-194) and β1(1-385) using the expression-based approach. The proteins were purified as described (see Experimental procedures) and isolated with a stochiometric amount of porphyrin (**Table C.1**). UV-visible spectral characterization was carried out on purified RuMP-containing β1(1-194) and β1(1-385), herein referred to as Ru β1(1-194) and Ru β1(1-385). UV-visible spectra show identical Soret band features at ~400 nm and splitting in the α/β region (~530 nm) (blue traces), indicating that the porphyrin is likely bound in a similar fashion in the two proteins (**Figure 4.4 and Table 4.3**).

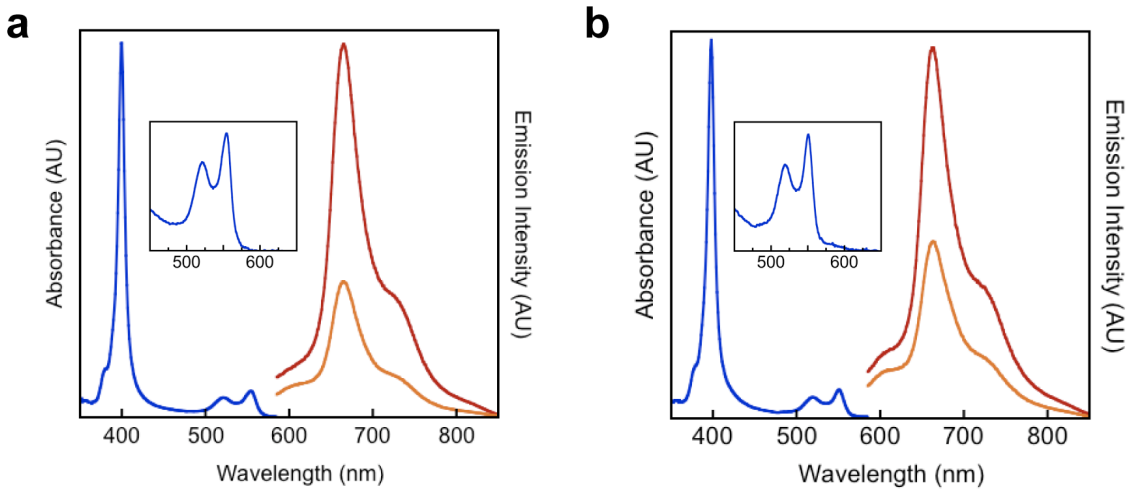

Figure 4.4 Steady-state absorbance (—) and emission spectra of RuMP–substituted **(a)** β1(1-194) and **(b)** β1(1-385). Emission spectra were acquired in the presence (—, 256 μM) and absence (—) of O_2.

Table 4.3 Spectroscopic and photophysical properties of Ru sGC constructs.

Protein	Absorbance λ_{abs} (nm)	Emission λ_{em} [a] (nm)	Lifetime τ_0 [c] (μs)
Ru β1(1-194)	399	664	12.9
	521	~725 [b]	
	553		
Ru β1(1-385)	398	663	8.2 [d]
	520	~725 [b]	24.2, [e] 3.6 [e]
	551		
Ru sGC [f]	399	664	~50
	515	~725 [b]	
	551		

[a] λ_{ex} = 550 nm. [b] shoulder. [c] λ_{ex} = 550 nm, λ_{det} = 640 nm, no O_2. [d] Single exponential fit. [e] Double exponential fit with fractional amplitudes of 26 ± 1% and 74 ± 1%, respectively. [f] C78S mutant shown. P118A had similar steady-state properties but lifetime data were not acquired due to limited protein amounts.

To provide an initial measure of O_2 accessibility in the sGC constructs, emission spectra were acquired of Ru β1(1-194) and Ru β1(1-385) in the presence and absence of O_2 (**Figure 4.4 and Table 4.4**). The emission of both constructs was quenched by O_2,

although less emission quenching was observed in Ru β1(1-385). Emission intensity was measured as a function of O_2 concentration to generate a Stern-Volmer plot (**Figure 4.5**). Quenching was found to be linear up to at least 256 μM (21%) O_2, suggesting that O_2 can diffuse near the heme sites of both constructs at physiological concentrations.

The observation of significant O_2 quenching in the sGC heme domains was not unexpected because heme-bound β1(1-194) and β1(1-385) have measurable autoxidation rates (**Table 4.1**). Therefore, it was of interest to measure O_2 accessibility in full-length sGC. However, unlike β1(1-194) and β1(1-385), full-length sGC is expressed using an Sf9/baculovirus system, which is not compatible with our heme-substitution method. Previous attempts to remove the native heme from sGC using denaturing conditions, followed by reconstitution with heme, were found to alter the properties of the native enzyme (29). Intriguingly, sGC mutants in the predicted heme pocket (P118A and C78S) (**Figure 4.1b**) have been reported (15, 24) that are expressed with low heme stochiometry but retain native sGC properties when they are reconstituted with heme (15, 29). Using this approach, sub-stochiometric quantities of RuMP were incubated with the apo full-length sGC mutants, and steady-state emission spectra were recorded in the presence and absence of O_2 following desalting to remove weakly bound porphyrin. Significantly decreased O_2 quenching was observed in full-length sGC compared to Ru β1(1-194) and Ru β1(1-385) (**Table 4.4** and **Figure 4.5**).

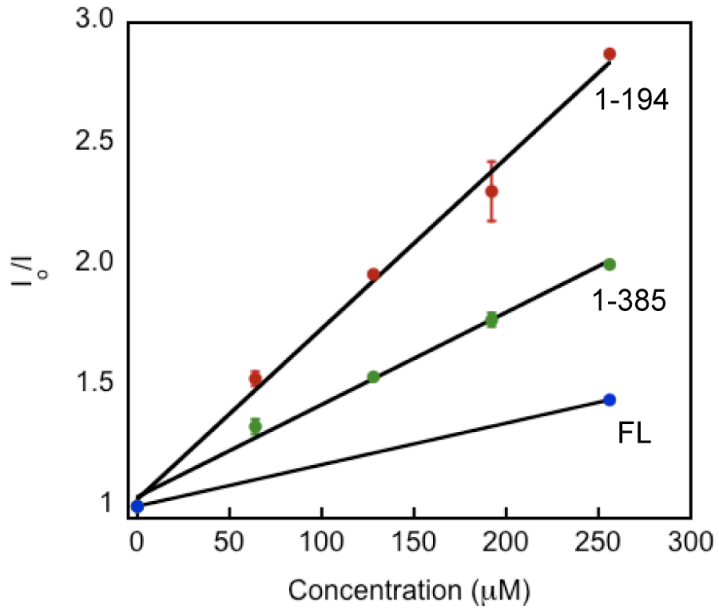

Figure 4.5 Stern-Volmer plot of steady-state emission quenching by O_2 for Ru β1(1-194), Ru β1(1-385), and Ru sGC. Data for the reconstituted C78S full-length sGC mutant is shown.

Table 4.4 Emission quenching of the Ru sGC constructs with O_2.

Protein	Steady-State	Time-Resolved	
	I_0/I	τ_0/τ	k_q (10^8 $M^{-1}s^{-1}$)[d]
Ru β1(1-194)	2.9	2.4	4.2
Ru β1(1-385)	2.0	1.7[a]	3.3[a]
		2.0,[b] 1.6[c]	1.6,[b] 6.5[c]
Ru sGC (C78S)	1.4	~1.2	~0.16
Ru sGC (P118A)	1.2	N/D	N/D

[a] Single exponential fit. [b] Double exponential fit (longer component). [c] Double exponential fit (shorter component). [d] Calculated from lifetime data. N/D = not determined due to limited protein amounts.

Time-resolved emission quenching in the sGC constructs. Time-resolved emission spectroscopy was carried out on the sGC constructs to provide a kinetic measure for O_2 diffusion near the heme site and probe the local heme coordination environment. Laser excitation at 550 nm yielded emission decays in the absence of O_2 that varied significantly between the sGC constructs. Ru β1(1-194) and Ru full-length sGC both displayed single exponential emission decays with significantly different lifetimes (τ_0 = 12.9 μs and ~50 μs, respectively) (**Table 4.3**). The longer lifetime in Ru full-length sGC suggests that RuMP may be in a more nonpolar environment (30). In Ru β1(1-385), double exponential emission decays were observed (τ_0 = 24.2 μs and 3.6 μs) (**Table 4.3**), indicating that the porphyrin is likely in at least two different conformations and/or coordination environments. The β1(1-385) construct is an unnatural homodimer (**Figure 4.1b**), which may display complex lifetime data due to the presence of non-equivalent heme sites.

Time-resolved emission data were collected in the presence of O_2 to monitor emission quenching. Lifetime-based data were found to parallel steady-state emission quenching data – Ru β1(1-194) exhibited the most quenching, followed by Ru β1(1-385) and Ru full-length sGC (**Table 4.4**). Emission lifetimes were used to calculate bimolecular quenching constants, k_q, for each of the sGC constructs using the Stern-Volmer equation (**Chapter 3**). Ru full-length sGC had a calculated bimolecular quenching constant approximately an order of magnitude lower than the domain truncations (**Table 4.4**). Together, the steady-state and time-resolved emission data indicate that O_2 diffusion to the heme site is more hindered in the full-length protein.

Implications for sGC structure and signaling. Results reported here support a model for sGC in which the heme pocket is appreciably buried. Steady-state and time-resolved emission quenching in RuMP-substituted full-length sGC suggests that the heme is ~10-fold less accessible to O_2 than in sGC truncations that display heme oxidation. Emission from RuMP in the absence of O_2 is a sensitive probe of local heme pocket

environment (18) and supports our O_2 quenching data. The longer excited-state lifetime in full-length sGC (τ_0) suggests that the heme pocket could be more nonpolar than in the truncations (30). Decreased solvent accessibility is expected to increase emission lifetime by suppressing the rate of nonradiative emission decay (30).

In addition to emission data, differences in heme redox potentials also suggest that the heme pocket is more buried in full-length sGC. Decreasing solvent accessibility in heme proteins has been shown to increase redox potentials by to 500 mV due to stabilization of the charge-neutral ferrous form of the heme (31). Importantly, the sGC truncations, unlike full-length sGC, form six-coordinate ferric complexes following binding of a –OH(H) ligand (19, 20). Lack of –OH(H) binding to the full-length sGC ferric heme (resulting in a five-coordinate complex) both favors a higher potential and provides evidence for decreased solvent accessibility to the heme site (5).

Burying of the sGC heme cofactor in the protein matrix appears to have important mechanistic consequences on sGC oxidation properties. The bimolecular quenching constant for full-length sGC is up to 1000X slower than values measured for diffusion-limited O_2 quenching (10^7 vs. 10^{10} $M^{-1}s^{-1}$) in which there is no kinetic barrier between the quencher and phosphor (28). The redox potential of the sGC truncation β1(1-385) measured here argues against heme electronics as the sole determinant for the ability of full-length sGC to resist oxidation in air. The redox potentials of both full-length sGC and β1(1-385) are much higher than the O_2/O_2^- redox couple. However, unlike full-length sGC, β1(1-385) exhibits measurable autoxidation kinetics in the presence of O_2. This implicates a difference in heme pocket accessibility as an important diverging feature between the sGC constructs. Comparison of the redox potential of full-length sGC with other heme proteins provides evidence for the role of accessibility in modulating oxidation. For example, cytochrome c has a potential much higher than sGC (Δ84 mV) (**Table 4.2**) but displays measurable oxidation kinetics in air (**Table 4.1**). Cytochrome c is a small protein with a solvent-exposed porphyrin that mediates rapid electron transfer in the mitochondrial electron transport chain (32). Therefore, heme accessibility and facile redox chemistry are intimately connected with its biological function.

The buried heme site in sGC may help to better trap NO under physiological O_2 tensions. Hindering ligand flux through sGC could enhance NO capture in the heme pocket and potentiate sGC activation. The affinity of NO for the sGC heme is extraordinarily high (pM) (33). Therefore, it is possible that the sGC scaffold could partially shield the heme to permit NO binding but disfavor reaction with O_2. Intriguingly, the bimolecular rate constant for NO binding (k_{on}) to the ferrous heme has been estimated to be >1.4 x 10^8 $M^{-1}s^{-1}$ at 4 °C (34), which is over 10-fold faster than the bimolecular quenching constant (k_q) measured for O_2 diffusion (~1.6 x 10^7 $M^{-1}s^{-1}$). This leaves open the possibility that NO and O_2 may have somewhat different accessibilities to the heme pocket. Future work will address this point by comparing NO and O_2 diffusion directly.

sGC function in aerobic contexts requires protection from O_2. Therefore, burying the heme cofactor in the protein matrix appears to serve as an important evolutionary strategy to protect the ferrous iron through maintaining a high potential and hindering O_2 diffusion. Our findings support the allosteric influence of protein structure on the chemistry of heme proteins. Fully elucidating heme protein mechanisms requires a detailed knowledge of the heme coordination environment as well as the influence of architectural features beyond the heme site.

References

1. Warner TD, Mitchell JA, Sheng H, & Murad F (1994) Effects of cyclic GMP on smooth muscle relaxation. *Adv Pharmacol* 26: 171-194.
2. Sanders KM & Ward SM (1992) Nitric oxide as a mediator of nonadrenergic noncholinergic neurotransmission. *Am J Physiol* 262: G379-392.
3. Munzel T, Feil R, Mulsch A, Lohmann SM, Hofmann F, & Walter U (2003) Physiology and pathophysiology of vascular signaling controlled by guanosine 3',5'-cyclic monophosphate-dependent protein kinase [corrected]. *Circulation* 108: 2172-2183.
4. Derbyshire ER & Marletta MA (2009) Biochemistry of soluble guanylate cyclase. *Handb Exp Pharmacol*: 17-31.
5. Stone JR & Marletta MA (1994) Soluble guanylate cyclase from bovine lung: activation with nitric oxide and carbon monoxide and spectral characterization of the ferrous and ferric states. *Biochemistry* 33: 5636-5640.
6. Boon EM & Marletta MA (2005) Ligand discrimination in soluble guanylate cyclase and the H-NOX family of heme sensor proteins. *Curr Opin Chem Biol* 9: 441-446.
7. Zhao Y, Brandish PE, DiValentin M, Schelvis JP, Babcock GT, & Marletta MA (2000) Inhibition of soluble guanylate cyclase by ODQ. *Biochemistry* 39: 10848-10854.
8. Stasch JP, Pacher P, & Evgenov OV (2011) Soluble guanylate cyclase as an emerging therapeutic target in cardiopulmonary disease. *Circulation* 123: 2263-2273.
9. Priviero FB & Webb RC (2010) Heme-dependent and independent soluble guanylate cyclase activators and vasodilation. *J Cardiovasc Pharmacol* 56: 229-233.
10. Gladwin MT (2006) Deconstructing endothelial dysfunction: soluble guanylyl cyclase oxidation and the NO resistance syndrome. *J Clin Invest* 116: 2330-2332.
11. Evgenov OV, Pacher P, Schmidt PM, Hasko G, Schmidt HH, & Stasch JP (2006) NO-independent stimulators and activators of soluble guanylate cyclase: discovery and therapeutic potential. *Nat Rev Drug Discov* 5: 755-768.
12. Underbakke E (2011) Unpublished results.
13. Haase T, Haase N, Kraehling JR, & Behrends S (2010) Fluorescent fusion proteins of soluble guanylyl cyclase indicate proximity of the heme nitric oxide domain and catalytic domain. *PLoS One* 5: e11617.

14. Winger JA & Marletta MA (2005) Expression and characterization of the catalytic domains of soluble guanylate cyclase: interaction with the heme domain. *Biochemistry* 44: 4083-4090.
15. Derbyshire ER, Winter MB, Ibrahim M, Deng S, Spiro TG, & Marletta MA (2011) Probing domain interactions in soluble guanylate cyclase. *Biochemistry* 50: 4281-4290.
16. Tsai AL, Berka V, Martin F, Ma X, van den Akker F, Fabian M, & Olson JS Is *Nostoc* H-NOX a NO sensor or redox switch? *Biochemistry* 49: 6587-6599.
17. Makino R, Park SY, Obayashi E, Iizuka T, Hori H, & Shiro Y (2011) Oxygen binding and redox properties of the heme in soluble guanylate cyclase: implications for the mechanism of ligand discrimination. *J Biol Chem* 286: 15678-15687.
18. Winter MB, McLaurin EJ, Reece SY, Olea C, Jr., Nocera DG, & Marletta MA (2010) Ru-porphyrin protein scaffolds for sensing O_2. *J Am Chem Soc* 132: 5582-5583.
19. Karow DS, Pan D, Davis JH, Behrends S, Mathies RA, & Marletta MA (2005) Characterization of functional heme domains from soluble guanylate cyclase. *Biochemistry* 44: 16266-16274.
20. Zhao Y & Marletta MA (1997) Localization of the heme binding region in soluble guanylate cyclase. *Biochemistry* 36: 15959-15964.
21. Woodward JJ, Martin NI, & Marletta MA (2007) An *Escherichia coli* expression-based method for heme substitution. *Nat Methods* 4: 43-45.
22. Winter MB, Herzik MA, Jr., Kuriyan J, & Marletta MA (2011) Tunnels modulate ligand flux in a heme nitric oxide/oxygen binding (H-NOX) domain. *Proc Natl Acad Sci U S A* 108: 17577-17578, E881-E889.
23. Derbyshire ER & Marletta MA (2007) Butyl isocyanide as a probe of the activation mechanism of soluble guanylate cyclase. Investigating the role of non-heme nitric oxide. *J Biol Chem* 282: 35741-35748.
24. Friebe A, Wedel B, Harteneck C, Foerster J, Schultz G, & Koesling D (1997) Functions of conserved cysteines of soluble guanylyl cyclase. *Biochemistry* 36: 1194-1198.
25. Brantley RE, Jr., Smerdon SJ, Wilkinson AJ, Singleton EW, & Olson JS (1993) The mechanism of autooxidation of myoglobin. *J Biol Chem* 268: 6995-7010.
26. Sawyer D & Valentine J (1981) How super is superoxide? *Acc Chem Res* 14: 393-400.
27. Vanderkooi JM, Wright WW, & Erecinska M (1994) Nitric oxide diffusion coefficients in solutions, proteins and membranes determined by phosphorescence. *Biochim Biophys Acta* 1207: 249-254.
28. Lakowicz JR (2006) Principles of Fluorescence Spectroscopy (Springer, New York).
29. Derbyshire ER (2011) Unpublished result.
30. Casper J & Meyer T (1983) Photochemistry of $Ru(bpy)_3^{2+}$. Solvent effects. *J Am Chem Soc* 105: 5583-5590.
31. Tezcan F, Winkler J, & Gray H (1998) Effects of ligation and folding on reduction potentials of heme proteins. *J Am Chem Soc* 120: 13383-13388.

32. Tollin G, Hanson LK, Caffrey M, Meyer TE, & Cusanovich MA (1986) Redox pathways in electron-transfer proteins: correlations between reactivities, solvent exposure, and unpaired-spin-density distributions. *Proc Natl Acad Sci U S A* 83: 3693-3697.
33. Winger JA, Derbyshire ER, & Marletta MA (2007) Dissociation of nitric oxide from soluble guanylate cyclase and heme-nitric oxide/oxygen binding domain constructs. *J Biol Chem* 282: 897-907.
34. Zhao Y, Brandish PE, Ballou DP, & Marletta MA (1999) A molecular basis for nitric oxide sensing by soluble guanylate cyclase. *Proc Natl Acad Sci U S A* 96: 14753-14758.
35. Mansouri A & Winterhalter KH (1973) Nonequivalence of chains in hemoglobin oxidation. *Biochemistry* 12: 4946-4949.
36. Wallace CJ & Tanaka Y (1994) Improving cytochrome c function by protein engineering?: studies of site-directed mutants of the human protein. *J Biochem* 115: 693-700.
37. Fritz BG, Hu X, Brailey JL, Berry RE, Walker FA, & Montfort WR (2011) Oxidation and loss of heme in soluble guanylyl cyclase from *Manduca sexta*. *Biochemistry* 50: 5813-5815.
38. Dou Y, Admiraal SJ, Ikeda-Saito M, Krzywda S, Wilkinson AJ, Li T, Olson JS, Prince RC, Pickering IJ, & George GN (1995) Alteration of axial coordination by protein engineering in myoglobin. Bisimidazole ligation in the His64-->Val/Val68-->His double mutant. *J Biol Chem* 270: 15993-16001.
39. Santucci R, Ascoli F, & Antonini E (1984) Redox potentials of normal and SH(beta 93)-modified human hemoglobin. Effect of pH and D-glycerate 2,3-bisphosphate. *Biochim Biophys Acta* 789: 20-25.

CHAPTER 5

NEW FRONTIERS: HIGH-RELAXIVITY AND HIGH-STABILITY PORPHYRIN-SUBSTITUTED H-NOX PROTEINS FOR MAGNETIC RESONANCE IMAGING (MRI)*

Summary

In this chapter, the porphyrin substitution method is used to generate H-NOX proteins for use as magnetic resonance imaging (MRI) contrast agents, expanding the functionality of the H-NOX family of molecular sensors. Heme protein-based MRI contrast agents represent a novel platform to both rationally tune metalloporphyrin properties for enhanced relaxivities and provide tightly coordinating frameworks for more effective delivery in biological systems. The proteins described in this chapter display improved properties over commercial small molecule MRI contrast agents and are promising candidates for future biological imaging applications.

Introduction

Magnetic resonance imaging has emerged as a powerful technique to profile mammalian physiology (1). MRI is widely used in medicine, for example, to distinguish between normal and healthy tissue in patients to improve diagnosis and therapy (1). MRI has numerous advantages over other imaging strategies: it is non-invasive, able to differentiate between soft tissues, and has high lateral and depth resolution (1 mm to 1 m) (2). These features allow for the construction of detailed images that provide a dynamic picture of changing physiological conditions.

The MRI signal is derived from the relaxation of water molecule protons (2). Relaxation rates vary across diverse tissues, which allows for tissue differentiation in MRI images. Significant investments have been made to improve MRI signal through the implementation of contrast agents containing paramagnetic metals (e.g., Mn^{II}, Mn^{III}, Fe^{III}, and Gd^{III}) (2). These agents increase the longitudinal ($1/T_1$) and transverse ($1/T_2$) relaxation rates of nearby water molecule protons via dipole interactions (2, 3). A parameter termed relaxivity ($r_{n=1,2}$) is used to quantify the concentration dependence of contrast agents on proton relaxation rates ($mM^{-1}s^{-1}$) (2). The relaxivities displayed by MRI contrast agents have been rationally enhanced by **(a)** increasing the number of

*The worked described in this chapter was done in collaboration with Piper J. Klemm in Prof. Kenneth N. Raymond's laboratory (UC Berkeley) and Christine M. Phillips-Piro, Ph.D. in Prof. Michael A. Marletta's laboratory (UC Berkeley). P.J.K. conducted relaxivity measurements. C.M.P.P collected X-ray diffraction data and solved the Mn *Tt* H-NOX crystal structure. Anthony T. Iavarone, Ph.D. collected the native MS of the intact Mn *Tt* H-NOX protein.

inner-sphere water molecules (q), **(b)** increasing inner-sphere water exchange rates ($1/\tau_M$) with bulk solvent, and **(c)** slowing the molecular tumbling rate ($1/\tau_R$) (2). Numerous and diverse chemical strategies have been implemented to optimize these parameters with the end goal of improving agent relaxivity (2). However, a persistent and paradoxical challenge has been the design of paramagnetic complexes that are kinetically inert in aqueous, biological conditions but maximize inner-sphere water interactions (2). Gd^{III}-containing complexes, in particular, display the highest ionic relaxivities due to the large number of unpaired electrons (e.g., seven versus one in Fe^{III}) (2). However, leaching of toxic aqueous Gd^{III} upon biological delivery has been linked to incurable conditions, such as nephrogenic systemic fibrosis, and remains a continuing patient safety challenge (4).

Here, hemoprotein-based scaffolds are used as a platform for the development of novel MRI contrast agents. Heme proteins represent readily modifiable frameworks for tuning the properties of metalloporphyrins and enhancing porphyrin bioavailability (5). As described in **Chapter 3**, the Heme Nitric oxide/OXygen-binding (H-NOX) domain from the thermophilic bacterium *Thermoanaerobacter tengcongensis* (*Tt* H-NOX) is an ideal scaffold for hemoprotein-based agents. *Tt* H-NOX is readily modifiable with site-directed mutagenesis and genetically encoded tags (6, 7). Additionally, *Tt* H-NOX is stable under extreme temperatures (>70 °C) (6). Using the expression-based method for porphyrin-substitution (**Chapter 1**), the *Tt* H-NOX scaffold was implemented to design a new class of high-relaxivity, high-stability MRI contrast agents.

Experimental Procedures

Porphyrin preparation. All manipulations of the porphyrins were carried out in low light. Mn^{III} protoporphyrin IX (MnPP) was purchased from Frontier Scientific. Initial synthesis attempts of Gd^{III} protoporphyrin IX (GdPP) were carried out through modification of established methods (8). Briefly, water was removed from a solution of $GdCl_3$ (6 mL, 0.3 mmol, 3 *eq*.) through rotary evaporation. $GdCl_3$ and protoporphyrin IX (50 mg, 0.09 mmol, 1 *eq*.) were refluxed under N_2 in a 2.0 g imidazole melt at 215 °C for 4 h. Reaction progress was monitored by UV-vis spectroscopy.

Plasmids for protein expression. The gene for *Tt* H-NOX (residues 1-188 of *Tt*Tar4H from *Thermoanaerobacter tengcongensis*) was used in the pCW vector with and without a C-terminal His_6 tag as described (7, 9).

Protein expression and porphyrin incorporation. Myoglobin (sperm whale skeletal muscle) was purchased from Sigma. Heme-containing *Tt* H-NOX His_6 was expressed as described previously (7). MnPP and GdPP were incorporated into *Tt* H-NOX constructs during anaerobic protein expression in the RP523 *E. coli* strain as described previously (5) with the following exceptions: Final concentrations of up to 30 μg/mL MnPP and 100 μM $MnCl_2$ were added to *E. coli* cultures to decrease Fe contamination in purified Mn *Tt* H-NOX. A modify recipe for TB media was used for Gd *Tt* H-NOX expression that contained 50 mM HEPES (pH 7.4), instead of phosphate

buffer, to prevent metal coordination. The crude GdPP reaction was dissolved in DMSO (~30 mL) and added to the culture immediately prior to induction.

Purification of Mn and Gd Tt H-NOX. Cell pellets (from 9 L of *E. coli* expression) were slowly thawed using warm water and re-suspended in ~100 mL of buffer A (50 mM TEA or HEPES, pH 7.5, 50 mM NaCl), which also contained 1 mM Pefabloc and DNase I. TEA was used for Mn *Tt* H-NOX, and HEPES was used for Gd *Tt* H-NOX. The resuspended cells were lysed 3 times with an EmulsiFlex-C5 homogenizer (Avestin, Inc.) at 4 ^{o}C between 50,000 and 150,000 psi. The lysate was then heat-denatured at 70 ^{o}C for 30 min using a water bath. All further manipulations were carried out at 4 ^{o}C. The lysate underwent centrifugation with an Optima XL-100K ultracentrifuge (Beckman Coulter, Inc.) for 1 h at 42,000 rpm.

For His_6-tagged Mn and Gd *Tt* H-NOX, the supernatant following ultracentrifugation was applied to a Co column at 1-2 mL/min equilibrated with buffer A. The column was washed with ~10 column volumes of buffer A, followed by ~10 column volumes of buffer A containing 10 mM imidazole at 2 mL/min. The protein was eluted with buffer A containing 150 mM imidazole at 2 mL/min. The flow-through was concentrated using a 5,000 MWCO spin concentrator and stored in small aliquots at –80 ^{o}C. Purity was estimated to be >95% by Coomassie stain following SDS-PAGE.

For non-tagged Mn *Tt* H-NOX, the supernatant was concentrated (~10 mL) and exchanged into buffer B (50 mM HEPES, pH 6.2, 5% glycerol) by gravity using a ~100 mL Sephadex G-25 column. The protein was then applied to a Toyopearl CM-650M cation exchange column (Tosoh Bioscience GmbH) that had been equilibrated with buffer B. The column was washed with 100 mL buffer B, and the protein was eluted with a NaCl gradient from 0% to 100% buffer C (50 mM HEPES, pH 6.2, 500 mM NaCl, 5% glycerol) over 800 mL while 5 mL fractions were collected. The Mn-containing protein was concentrated using a 5,000 MWCO spin concentrator and exchanged into buffer D (50 mM TEA, pH 7.5, 50 mM NaCl, 5% glycerol). Mn *Tt* H-NOX was then stored in small aliquots at –80 ^{o}C. Purity was estimated to be >95% by Coomassie stain following SDS-PAGE.

Mn Tt H-NOX His_6 native nanoelectrospray ionization mass spectrometry and tandem mass spectrometry. Mass spectra were acquired using an orthogonal acceleration quadrupole time-of-flight (Q-Tof) mass spectrometer equipped with a Z-spray electrospray ionization (ESI) source (Q-Tof Premier, Waters, Milford, MA). Ions were formed directly from aqueous solutions containing micromolar analyte and 50 mM ammonium bicarbonate, using positive-ion nanoelectrospray ionization (nanoESI). NanoESI emitters were pulled from borosilicate glass capillary tubes (1.0 mm outer diameter/0.78 mm inner diameter, Sutter Instruments, Novato, CA) using a Flaming/Brown micropipette puller (Model P-87, Sutter). Approximately 10 μL of the sample solution was added into a nanoESI emitter using a 10 μL microsyringe (Hamilton, Reno, NV). The nanoESI tip was positioned approximately 2 mm from the sample cone aperture. The electrospray was initiated by gradually increasing the DC potential applied to a platinum wire (0.127 mm diameter, Sigma-Aldrich, St. Louis, MO), which was

inserted into the nanoESI emitter to within approximately 2 mm of the tip, until the onset of mass spectral signal. No back pressure or cone gas was used. Instrument parameters during data acquisition were as follows: nanoESI voltage 1.8 kV, sample cone voltage 20 V, extraction cone and ion guide voltages both 4.0 V, source block temperature 80 ºC, accelerating voltage into the argon-filled cell 3 V, first pumping stage (backing) pressure 2 mbar, ion transfer stage pressure 6×10^{-3} mbar, argon-filled cell pressure 8×10^{-3} mbar, Tof analyzer pressure 8×10^{-7} mbar. The Tof analyzer was operated in "V" mode. For tandem mass spectrometry (MS/MS) measurements using collisionally activated dissociation (CAD), the precursor ion of interest was mass-selected using the quadrupole filter and the accelerating voltage into the argon-filled cell was gradually increased, to a final value of 25 V, to achieve precursor ion dissociation. Mass spectra and MS/MS spectra were recorded over a period of 3 min using a 0.95 s scan integration and 0.05 s interscan delay. External mass calibration of the Tof analyzer was performed immediately prior to measurements. Mass spectra were processed using MassLynx software (version 4.1, Waters).

Crystallization of Mn Tt H-NOX. Crystallization experiments were carried out using Mn^{III} *Tt* H-NOX (non-tagged), and all manipulations were carried out in low light. Protein was exchanged into buffer F (20 mM TEA, pH 7.5) using a PD-10 column and then concentrated to 30 mg/mL using a Vivaspin 500 5,000 MWCO PES spin concentrator. Crystals were grown using sitting drop vapor diffusion in which 1 μL of the protein was mixed with 1 μL of reservoir solution and equilibrated against a 500 μL reservoir of 40% to 42.5% (w/v) polypropylene glycol P400 and 0.1 M BIS-TRIS (pH 6.5) at 20 ^{o}C. Crystals appeared within 24 h and were cryoprotected by soaking them in the precipitant solution supplemented with 10% (v/v) glycerol. The crystals were flash frozen in liquid N_2 for storage.

X-ray data collection and structure solution. X-ray data for Mn *Tt* H-NOX were collected using synchrotron radiation at beamline 8.3.1 at the Advanced Light Source (ALS), Lawrence Berkeley National Laboratory (Berkeley, CA). Diffraction images were collected at 100 K with exposure times of 2.5 s to 3 s with 1º oscillations per frame at a wavelength of $\lambda = 0.97$ Å. Data integration and scaling were performed using the HKL2000 (10) suite. Phases were determined by molecular replacement with Phaser (11) using wild-type *Tt* H-NOX (PDB ID 1U55, molecule A), with water molecules and heme removed, as the search model.

X-ray absorption spectroscopy. To confirm the presence of Mn in the *Tt* H-NOX crystals (and lack of Fe contamination), X-ray absorption spectra were collected at the Mn and Fe K-edges (1.90 and 1.74 Å, respectively) at 100 K using synchrotron radiation as described above.

UV-visible spectroscopy. Steady-state absorbance measurements were carried out at room temperature in buffer G (50 mM HEPES, pH 7.4, 50 mM NaCl) on a Cary 3E 300 spectrophotometer (Varian).

Protein autoxidation. The autoxidation rate of Mn^{II} *Tt* H-NOX His_6 was

determined in air-saturated buffer G at 22 °C. Mn^{III} *Tt* H-NOX was reduced with excess sodium dithionite in an anaerobic chamber (Coy) and desalted into buffer G using a PD10 column. Autoxidation was initiated by aeration of the protein through two-fold dilution into aerobic buffer followed by gentle mixing. UV-visible spectra were recorded every 1 min for 60 min followed by every 10 min for an additional 20 min. Data were fit to a single-exponential equation.

Inductively coupled plasma-optical emission spectroscopy (ICP-OES). ICP-OES was performed on a Perkin Elmer Optima 7000 DV. Proteins for analysis were digested and diluted in 2% (v/v) nitric acid in Millipore water in plastic or EDTA washed glassware. Gd, Mn, and Fe standards were prepared (in EDTA washed glassware) in 2% (v/v) nitric acid/Millipore water from commercial ICP standards with concentrations between 0.01 and 10.0 μg/mL. Exact Gd, Mn, and Fe concentration was measured in six times and used for relaxivity analysis (μm).

Relaxivity studies. T_1 and T_2 measurements were performed on a Bruker mq60 minispec relaxometer in buffer H (50 mM HEPES, pH 7.4, 50 mM NaCl, 5% glycerol). T_1 and T_2 were determined at 60 MHz (1.41 T) using an inversion recovery pulse sequence. Temperature of the samples, in Millipore water (pH 6), was controlled at 37.0 °C using a Julabo F25 circulating water bath. Each sample was analyzed by ICP-OES for exact Gd, Mn and Fe concentration. The inverse of the longitudinal relaxation time of each sample ($1/T_1$, s^{-1}) was plotted against Gd, Mn, and Fe concentration (μM) and fit by linear regression ($R^2 > 0.99$) to determine the relaxivity (r) according to the following equation:

$$\frac{1}{T_{n=1,2}} = \frac{1}{T_{(solvent)n=1,2}} + r_{n=1,2}[agent]$$

Relaxivity analyses were performed in triplicate (3 samples, 3 times to report experimental and instrument error) and averages reported. Instrument Parameters: Scans: 4; Recycle Delay: 18.5 s; Gain: 53; Dummy Shots: 0; Detection mode: real; Bandwidth: Broad, 20,000 kHz; Monoexponential Curve Fitting, Phase Cycling. First Pulse Separation: 5 ms; Final Pulse separation: 18,500 ms, Number of data points for fitting: 20; Delay sample window: 0.05 ms; Sampling Window: 0.02 ms; Time for Saturation Curve Display: 6 s.

Plasma stability. The stability of Fe^{III}, Mn^{III}, and Gd^{III} *Tt* H-NOX His_6 were measured in plasma at 37 °C over 24 h using previously described methods (5). Briefly, the proteins were exchanged into DPBS using a PD10 column. An equal volume of protein (~5 mg/mL by A280) and plasma were incubated at 37 °C, and time points were taken after 0, 1, 3, 6, and 24 h. For each time point, the aliquots were centrifuged for 2 min at 3,000 rpm (665 x *g*), and UV-visible spectra were acquired of the supernatant in DPBS.

Results and Discussion

Relaxivities of ferric proteins. Iron is an inexpensive, abundant earth metal (12). Although Fe displays lower relaxivities compared to lanthanides, the lower cost and environmental impact of Fe make it a promising candidate for more sustainable contrast agent development (12, 13). In an effort to enhance the relaxivity of Fe, we first evaluated native heme-containing *Tt* H-NOX and myoglobin as potential protein scaffolds for MRI.

UV-visible spectral characterization of ferric Mb and *Tt* H-NOX was carried out to probe the influence of the protein scaffolds on heme electronic properties. The ferric proteins were found to have distinct UV-visible spectra. The spectrum of ferric Mb has a sharp Soret band at 408 nm, whereas *Tt* H-NOX has a broad Soret band at 413 nm and distinct splitting in the α/β region (~500-600 nm) (**Figure 5.1a and Table D.1**). These data suggest that the protein scaffolds provide unique porphyrin coordination environments. Indeed, examination of the crystal structures of both proteins demonstrates that they have diverse heme pocket architectures, and the heme groups are in different protein-bound conformations (**Figure 5.2**).

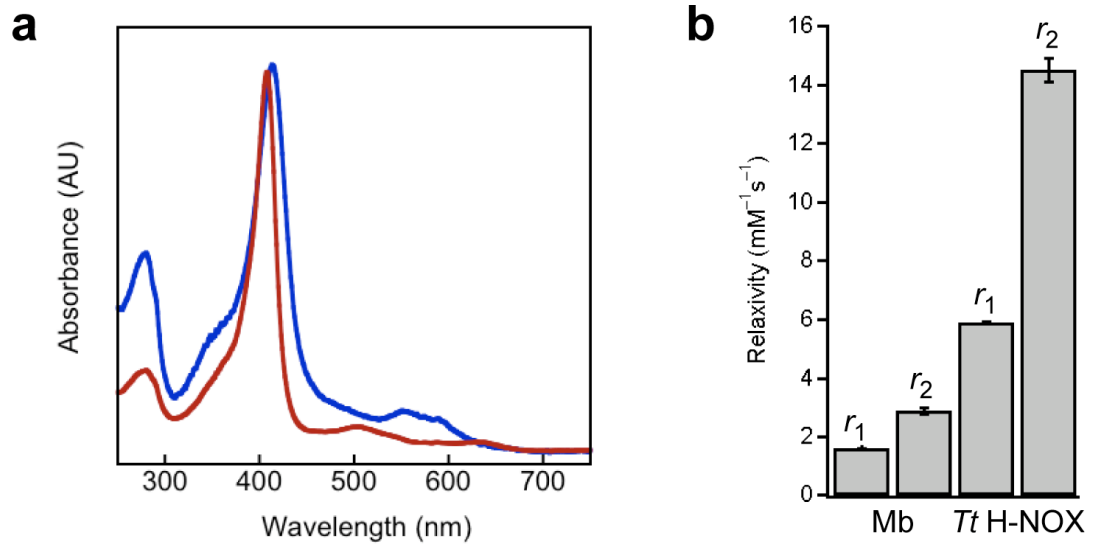

Figure 5.1 (a) UV-visible spectra of ferric myoglobin (—) and *Tt* H-NOX (—). **(b)** Relaxivities of ferric myoglobin and *Tt* H-NOX at 37 °C and 60 MHz.

To assess the influence of protein structure on relaxivity, T_1 and T_2 measurements were carried out on the ferric proteins. Mb was found to have T_1 and T_2 relaxivities of 1.6 and 2.9 $mM^{-1}s^{-1}$, respectively. Surprisingly, *Tt* H-NOX displayed much higher T_1 and T_2 relaxivities of 5.9 and 14.5 $mM^{-1}s^{-1}$ (**Figure 5.1b and Table 5.1**). *Tt* H-NOX is a larger protein (~22 kDa vs. ~17 kDa), which could enhance relaxivity by decreasing protein tumbling in solution (2, 14). Additionally, comparison of reported pK_a values of the heme –OH(H) ligand suggests that it has different protonation states at physiological pH in the proteins (pK_a = 6.8 and 8.95 for *Tt* H-NOX (15) and Mb (16), respectively). In *Tt* H-

NOX, the more labile water ligand is favored, which likely enhances relaxivity by undergoing more facile exchange with solvent.

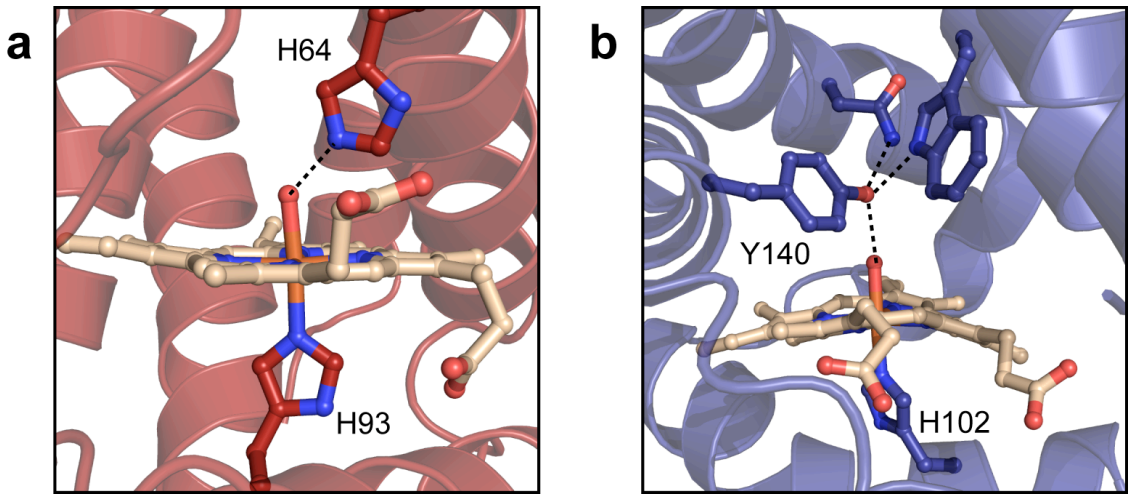

Figure 5.2 Crystal structures of the ferric forms of **(a)** myoglobin (PDB ID 1A6K) and **(b)** *Tt* H-NOX (PDB ID 1U56). Proximal histidine ligands, –OH(H) ligands, and hydrogen bonding residues are shown.

Relaxivities of Mn Tt H-NOX. Due to the enhanced relaxivity of *Tt* H-NOX, we decided to incorporate other metals into the protein scaffold to improve its imaging properties. Mn complexes have been evaluated as potential MRI contrast agents (17). However, Mn-based complexes have seen only limited clinical use because they suffer from high kinetic lability under physiological conditions (17, 18). Although Mn complexes display lower relaxivities, they have emerged as an important alternative for lanthanide-based agents due to the decreased toxicity of Mn as an endogenous metal ion (17).

Mn^{III} protoporphyrin IX (MnPP) was incorporated into *Tt* H-NOX during protein expression. Heme contamination was observed by UV-visible spectroscopy following longer induction times, and during expressions with high protein yields (data not shown). However, Mn and Fe-bound protein was readily separated with cation-exchange chromatography using standard protocols (see Experimental Procedures). A UV-visible spectrum of the purified protein shows two characteristic Mn-based absorption features (376 nm and 474 nm) (**Figure 5.3a** and **Table D.1**) that are similar to those reported previously (19). To further characterize purified Mn *Tt* H-NOX, native ionization mass spectrometry was performed on the intact protein complex. A mass corresponding to the holoprotein was observed (23,695 ± 3 Da; calc: 23,693 Da) (**Figure D.1a**), and collisionally activated dissociation (CAD) confirmed that the protein was purified MnPP-bound (obs: 615.18 Da; calc: 615.18) (**Figure D.1b**). Further ICP-OES analysis carried out on the purified protein verified the presence of Mn and no detectible Fe (to pM concentrations).

T_1 and T_2 relaxivity measurements were performed on Mn *Tt* H-NOX. The Mn^{II} oxidation state was found to not be stable in air (k_{ox} = ~0.069 min^{-1} at 22 °C) (**Figure**

5.3a), and therefore, relaxivity measurements for Mn^{II} *Tt* H-NOX were conducted under anaerobic conditions. The T_1 and T_2 relaxivities of Mn^{III} *Tt* H-NOX (12.0 and 16.9 $mM^{-1}s^{-1}$, respectively) are much higher than those of the Mn^{II} protein (**Figure 5.3b** and **Table 5.1**). Notably, the relaxivities of the protein in both oxidation states are higher than MnDPDP, which is the only current clinical Mn-based agent (**Table 5.1**) (20).

To provide a molecular understanding for the high relaxivity in Mn^{III} *Tt* H-NOX, we pursued a crystal structure of the protein. Crystals were obtained of Mn^{III} *Tt* H-NOX using sitting-drop vapor diffusion and were found to diffract to 2.15 Å. X-ray absorption spectra collected at the Mn and Fe K-edges confirmed the presence of Mn and no detectable Fe in the protein crystals (**Figure D.2**). A preliminary crystal structure of Mn *Tt* H-NOX was solved in the C_2 space group using molecular replacement with the structure of wild-type *Tt* H-NOX as the search model (PDB ID 1U55) (**Table D.2**). Initial electron density corresponding to Mn was observed in the protein heme pocket (data not shown), and the structure is now undergoing further rounds of refinement.

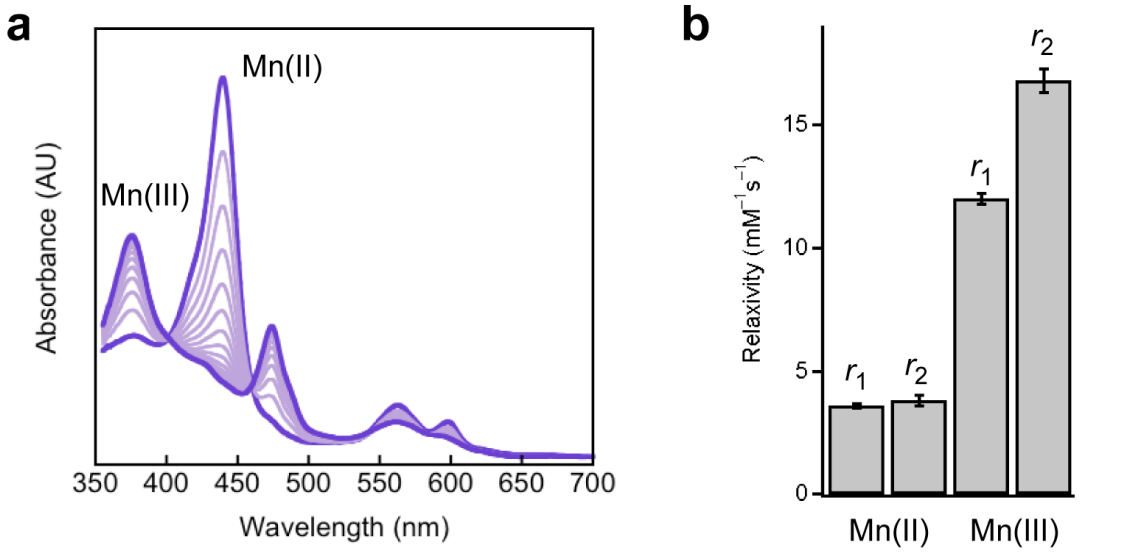

Figure 5.3 (a) Time-resolved UV-visible spectra of Mn^{II} to Mn^{III} *Tt* H-NOX oxidation in air. **(b)** Relaxivities of Mn^{II} and Mn^{III} *Tt* H-NOX at 37.0 °C and 60 MHz.

Relaxivities of Gd Tt H-NOX. The high relaxivities displayed by lanthanide(III) complexes are ideally suited for MRI applications (3). However, as discussed above, lanthanide complexes are kinetically labile under biological conditions, and aqueous lanthanide(III) ions are highly toxic (4). To address this issue, we have also sought to incorporate Gd^{III} protoporphyrin IX into the *Tt* H-NOX scaffold in an effort to create a kinetically inert, protein-based contrast agent.

Gd^{III} protoporphyrin IX was synthesized using an imidazole melt in a manner similar to published methods (8). However, initial mass spectrometry analysis suggests that the porphyrin macrocycle was adducted by imidazole during reflux conditions (data not shown). To test the feasibility of generating Gd *Tt* H-NOX, initial Gd porphyrin

incorporation studies were pursued. UV-visible spectroscopy conducted on the purified protein suggests at least two different species are present (**Figure 5.4a**). ICP analysis confirmed the presence Gd in the purified protein and absence of Fe contamination. This suggests that the *Tt* H-NOX sample may contain either different Gd-bound species or a mixture of Gd and metal-free porphyrin. Importantly, no significant Gd loss was observed by UV-visible spectroscopy during protein purification, providing initial evidence that Gd is not readily labile when protein-bound. Preliminary T_1 and T_2 relaxivity measurements were performed on the Gd protein. Gd *Tt* H-NOX was found to have relaxivities of 19 and 27 $mM^{-1}s^{-1}$ (**Figure 5.4b**, which are greatly enhanced compared to small molecule Gd complexes measured under identical conditions (**Table 5.1**).

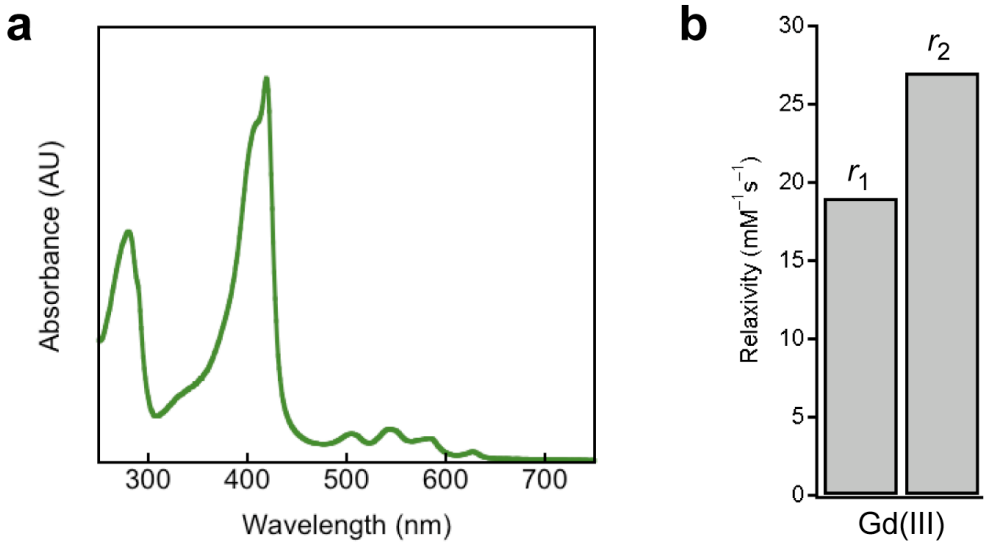

Figure 5.4 (a) UV-visible spectrum of Gd^{III} *Tt* H-NOX. **(b)** Preliminary relaxivity measurements of Gd^{III} *Tt* H-NOX at 37.0 °C and 60 MHz.

Table 5.1 Relaxivities of selected complexes acquired at 60 mHz and 37 °C using micromolar concentrations of agent.

Complex	r_1 ($mM^{-1}s^{-1}$)	r_2 ($mM^{-1}s^{-1}$)	*q* value	*Ref.*[a]
Fe^{III} Mb	1.60 ± 0.01	2.9 ± 0.1	1	
Fe^{III} *Tt* H-NOX	5.90 ± 0.03	14.5 ± 0.4	1	
Mn^{II} *Tt* H-NOX	3.6 ± 0.1	3.8 ± 0.2		
Mn^{III} *Tt* H-NOX	12.0 ± 0.2	16.8 ± 0.5		
Gd^{III} *Tt* H-NOX	19	27		
MnDPDP	2.8[b]	N/D		(20)
Gd-DTPA (Magnevist)	3.3 ± 0.3	3.9 ± 0.3	1	(21)
Gd-DOTA (Dotarem)	3.0 ± 0.3	3.5 ± 0.3	1	(21)
Gd-HP-DO3A (Prohance)	2.9 ± 0.3	3.4 ± 0.3	1	(21)

[a] This work unless noted. [b] 10 MHz and 25 °C. N/D = not determined.

Plasma stability of H-NOX complexes. To evaluate the stability of the Fe^{III}, Mn^{III}, and Gd^{III} *Tt* H-NOX complexes under biological conditions, stability time courses were conducted in plasma at 37 °C. UV-visible spectra were acquired over 24 h to record any changes in porphyrin absorbance. Importantly, no porphyrin loss or demetalation was observed in any of the protein complexes under the assay conditions (**Figure 5.5**). These data confirm that *Tt* H-NOX provides a highly stable framework for coordinating metals under biological conditions.

Enhancing protein properties for MRI. Numerous strategies are available to rationally tune the properties of the protein-based agents for improved imaging and biological delivery. The relaxivities of the proteins could be enhanced through the encapsulation of other metalloporphyrins or complexes in the heme pocket. Additionally, structure-guided mutagenesis could be used to modify the metal coordination environment to tune relaxivity and/or further enhance metal binding affinity. These changes could include the incorporation of amino acids providing oxygen ligands (since lanthanides in particular are oxophilic) or opening the heme pocket for improved water exchange with bulk solvent. As described in **Chapter 3**, targeting groups could be appended to the protein scaffold through genetic or chemical means to enhance biological retention. Additionally, the biocompatibility of the agents could be improved and the size modulated through modification of the protein surface (e.g., through PEGylation). These strategies will allow the protein-based agents to be uniquely tailored for desired imaging applications.

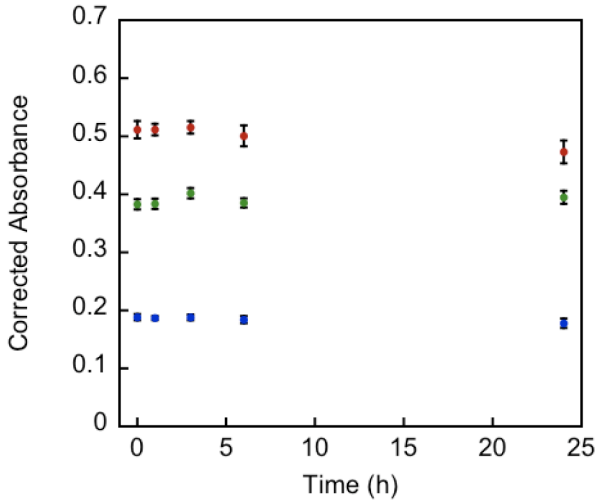

Figure 5.5 Plasma stability of Fe^{III} (—), Gd^{III} (—), and Mn^{III} (—) *Tt* H-NOX complexes (~2.5 mg/mL by A280) in DPBS at 37 °C over 24 h. Absorbance is plotted at 414 nm, 420 nm, and 474 nm, respectively, and corrected for the plasma background. N = 3.

References

1. Moonen CT, van Zijl PC, Frank JA, Le Bihan D, & Becker ED (1990) Functional magnetic resonance imaging in medicine and physiology. *Science* 250: 53-61.
2. Datta A & Raymond KN (2009) Gd-hydroxypyridinone (HOPO)-based high-relaxivity magnetic resonance imaging (MRI) contrast agents. *Acc Chem Res* 42: 938-947.
3. Caravan P, Ellison JJ, McMurry TJ, & Lauffer RB (1999) Gadolinium(III) chelates as MRI contrast agents: Structure, dynamics, and applications. *Chem Rev* 99: 2293-2352.
4. Hasebroock KM & Serkova NJ (2009) Toxicity of MRI and CT contrast agents. *Expert Opin Drug Metab Toxicol* 5: 403-416.
5. Winter MB, McLaurin EJ, Reece SY, Olea C, Jr., Nocera DG, & Marletta MA (2010) Ru-porphyrin protein scaffolds for sensing O_2. *J Am Chem Soc* 132: 5582-5583.
6. Boon EM & Marletta MA (2006) Sensitive and selective detection of nitric oxide using an H-NOX domain. *J Am Chem Soc* 128: 10022-10023.
7. Weinert EE, Plate L, Whited CA, Olea C, Jr., & Marletta MA (2010) Determinants of ligand affinity and heme reactivity in H-NOX domains. *Angew Chem Int Ed Engl* 49: 720-723.
8. Srivastava T (1980) Gadolinium(III) myoglobin: interaction of Gd(III) mesoporphyrin IX with apomyoglobin. *Current Science* 49: 429-430.
9. Karow DS, Pan D, Davis JH, Behrends S, Mathies RA, & Marletta MA (2005) Characterization of functional heme domains from soluble guanylate cyclase. *Biochemistry* 44: 16266-16274.

10. Otwinowski Z & Minor W (1997) Processing of X-ray diffraction data collected in oscillation mode. *Method Enzymol* 276: 307-326.
11. McCoy AJ, Grosse-Kunstleve RW, Storoni LC, & Read RJ (2005) Likelihood-enhanced fast translation functions. *Acta Crystallogr D Biol Crystallogr* 61: 458-464.
12. Humphries M (2010) Rare earth elements: The global supply chain (Congressional Research Service).
13. Kummerer K & Helmers E (2000) Hospital effluents as a source of gadolinium in the aquatic environment. *Environ Sci Technol* 34: 573-577.
14. Strauch RC, Mastarone DJ, Sukerkar PA, Song Y, Ipsaro JJ, & Meade TJ (2011) Reporter protein-targeted probes for magnetic resonance imaging. *J Am Chem Soc* 133: 16346-16349.
15. Olea C, Jr., Kuriyan J, & Marletta MA (2010) Modulating heme redox potential through protein-induced porphyrin distortion. *J Am Chem Soc* 132: 12794-12795.
16. Brunori M, Amiconi G, Antonin E, Wyman J, Zito R, & Fanelli AR (1968) The transition between 'acid' and 'alkaline' ferric heme proteins. *Biochim Biophys Acta* 154: 315-322.
17. Tan M, Ye Z, Jeong EK, Wu X, Parker DL, & Lu ZR (2011) Synthesis and evaluation of nanoglobular macrocyclic Mn(II) chelate conjugates as non-gadolinium(III) MRI contrast agents. *Bioconjug Chem* 22: 931-937.
18. Drahos B, Kubicek V, Bonnet CS, Hermann P, Lukes I, & Toth E (2011) Dissociation kinetics of Mn^{2+} complexes of NOTA and DOTA. *Dalton Trans* 40: 1945-1951.
19. Woodward JJ, Martin NI, & Marletta MA (2007) An *Escherichia coli* expression-based method for heme substitution. *Nat Methods* 4: 43-45.
20. Elizondo G, Fretz CJ, Stark DD, Rocklage SM, Quay SC, Worah D, Tsang YM, Chen MC, & Ferrucci JT (1991) Preclinical evaluation of MnDPDP: new paramagnetic hepatobiliary contrast agent for MR imaging. *Radiology* 178: 73-78.
21. Port M, Idee JM, Medina C, Robic C, Sabatou M, & Corot C (2008) Efficiency, thermodynamic and kinetic stability of marketed gadolinium chelates and their possible clinical consequences: a critical review. *Biometals* 21: 469-490.

CHAPTER 6

FUTURE DIRECTIONS

Summary

In this final chapter, suggestions for future experiments are provided. The projects developed in this dissertation expand upon the ideas and experiments of others. Therefore, it is my hope that this study also influences the work of future investigators in the lab.

Future Directions

Measuring ligand diffusion in H-NOX proteins. Initial efforts have been presented to understand the functional influence of H-NOX protein structure on modulating ligand diffusion. These studies have pointed to previously uncharacterized roles for H-NOX protein scaffolds in tuning gas-sensing properties.

In **Chapter 2**, X-ray crystallography with xenon was used to map a tunnel network in a prokaryotic H-NOX domain with similar ligand-binding properties to sGC. The tunnels in the H-NOX domain are lined with hydrophobic residues and contain no ordered water molecules, providing initial evidence that they could be favorable routes for gas diffusion. Xenon occupancy was observed in the tunnel network during pressurization experiments, confirming that the tunnels are accessible to gases. Our experimental work agreed with a recent molecular dynamics (MD) study, which identified the tunnels as the most favorable routes for CO escape from the heme pocket (1).

Future work in this area should further consider the role of protein dynamics in modulating ligand diffusion to and from the heme site. It is possible that protein dynamics could provide additional pathways for ligand migration in H-NOX proteins. This is evident in O_2-binding H-NOX proteins, which do not appear to have preformed routes of ligand entry and exit. Computationally, new transient pathways could be identified through MD simulations conducted on long timescales. In addition, these simulations paired with a technique termed Implicit Ligand Sampling (ILS) could be used to map areas in the protein structure that are favorable for gas binding (2). This technique has been applied extensively in the globins and other protein families to identify internal ligand migration pathways (2). Experimental approaches also could be used to detect dynamics in H-NOX proteins. For example, hydrogen/deuterium (H/D) exchange with mass spectrometry would be useful to characterize protein dynamics in solution (3). This technique is currently being applied successfully in the laboratory to map higher-order domain architecture in mammalian NOS and sGC (4). In addition to H/D exchange, room temperature crystal structures of H-NOX proteins could be obtained. The Alber laboratory has used this approach with much success to indentify packing and side chain

differences in proteins for which datasets have been collected at both room and cryogenic temperatures (5). A room temperature structure of the H-NOX protein from *Thermoanaerobacter tengcongensis* (*Tt* H-NOX) was solved and there were no major structural differences compared to the cryogenic structure (6). However, it is possible that changes could be observed in other H-NOX proteins that are not from thermophilic organisms.

To provide functional information about the role of H-NOX tunnels in modulating diatomic gas affinity, structure-guided tryptophan mutants were engineered in an attempt to block the tunnel network. The kinetic changes that were observed – increased CO association rates combined with decreased CO dissociation rates – suggested that hindering gas diffusion through the tunnels results in increased ligand trapping near the heme, potentially due to blocking routes for gas escape. The kinetic changes observed are modest but in agreement with what others have found upon blocking interior tunnels in truncated globins (7, 8). Crystal structures of many of the tryptophan variants were solved and no significant structural changes were observed. However, it is possible that incorporation of the tryptophan residues could have unintended effects on protein dynamics that are not evident in the structural data. The computational and experimental techniques described above could be used to further assess the effects of the mutations on protein structure. To provide additional experimental evidence for our "trapping" hypothesis, photolysis experiments could be conducted on short timescales (ps to μs). This would generate a more complete kinetic picture of ligand diffusion by providing rates of ligand recombination and escape (9). In addition to solution kinetic experiments, laser photolysis could be combined with crystallography, potentially allowing CO migration to be observed directly in the WT and mutant structures (10, 11).

Our initial work on characterizing the tunnel network provided the first experimental evidence that H-NOX proteins have discrete pathways for ligand diffusion. Due to this finding, we were interested in assessing the broader influences of protein structure on gas migration in the H-NOX family. Unlike isolated H-NOX domains, sGC is a more structurally complex, multi-domain protein with particularly unusual heme properties. In addition to not binding O_2, the heme in full-length sGC exhibits no measureable oxidation in air. It has been speculated that the ability of the sGC heme to resist oxidation is due to a high redox potential and/or limited O_2 accessibility to the heme site. To measure O_2 diffusion in sGC, a phosphorescent Ru porphyrin was incorporated in the heme pocket in place of the native heme (**Chapter 4**). Emission quenching experiments with O_2 suggested that the sGC heme is ~1000X more protected from O_2 than in bulk solvent. However, it is unclear from these data if ligand access is broadly limited to the buried heme site or if gases have differential accessibilities. Although NO, O_2, and CO are small and relatively nonpolar, studies in globins have demonstrated that these gases can partition differently into proteins and that they can have non-overlapping ligand migration pathways (12). Computationally, this idea could be tested using the ILS technique described above in H-NOX proteins for which structures are available. Additionally, emission quenching experiments could be used to compare the accessibilities of NO and O_2 directly in sGC because NO is also an effective

phosphorescence quencher (13). Preliminary studies using H-NOX constructs containing RuMP indicated that the porphyrin was not stable in the presence of NO. This could be due to NO displacing the Ru–CO ligand. Future quenching experiments with NO should utilize substitution-inert porphyrins (e.g., Pd or Pt) or less labile phosphorescent Ru porphyrin complexes.

Based on our initial work with sGC, O_2 quenching experiments also could be implemented to study gas diffusion in the H-NOX tunnel-blocking variants. This line of investigation would provide a simple measure of gas accessibility that is independent of ligand binding and may be a viable strategy to confirm our ligand "trapping" hypothesis.

Building H-NOX imaging agents. Initial interest in measuring O_2 accessibility in sGC led to the development of H-NOX sensors containing unnatural porphyrins for biological use (**Chapters 3 and 5**). Heme protein scaffolds are particularly advantageous for porphyrin-based imaging agents because heme proteins have evolved to bind porphyrins with high fidelity and specificity under biological conditions. Therefore, protein scaffolds present unique opportunities to tune porphyrin properties and target porphyrins for biological delivery. The work presented in this dissertation is to be regarded as only a starting point in the development of this new family of heme protein-based agents. Future work should focus on both ***(1)*** assessment of protein function in physiological conditions and ***(2)*** improvement of protein properties. Heme-containing H-NOX proteins have already seen promise in preclinical studies as a platform for O_2 delivery to tumors (Omniox, Inc.). However, the biological utility of the imaging agents described here remains to be tested. Experiments to evaluate protein pharmacokinetics and biological function will undoubtedly inform future modifications to improve protein properties. However, several long-term design goals have been broadly defined below.

For optical O_2 sensors, improved sensitivity to O_2 is facilitated by longer emission lifetimes (14, 15). Therefore, incorporation of metalloporphyrins displaying long-lived excited states should be a continued objective. In addition to longer emission lifetimes, enhancing O_2 accessibility to the porphyrin via mutagenesis could be used to increase O_2 responsiveness. To facilitate detection in biological conditions and decrease acquisition times, the protein sensors should have high quantum yields. Quantum yields could be improved through the choice of porphyrin or by modification of the porphyrin coordination environment (e.g., by increasing hydrophobicity) (16). Additionally, appending the proteins to imaging agents, such as quantum dots (QDs), has proven to be a promising strategy to improve sensor brightness. QDs also have the advantage of providing a large two-photon absorption cross-section (17). This allows for excitation with longer wavelength light to enhance penetration in tissues. For biological imaging, a continued goal should be to develop sensors that absorb and emit light within the therapeutic window (600-1000 nm) (18). This could be achieved through modification of the porphyrin (e.g. by increasing π conjugation) and/or through two-photon imaging techniques (19).

For MRI contrast agents, relaxivity can be rationally enhanced through facilitating interactions between the porphyrin and inner-sphere water molecules, as previously

described (20). Potential changes to the protein to increase water accessibility need to be balanced with the importance of maintaining a kinetically inert metal site (20). For example, mutagenesis could be used to increase solvent accessibility in the heme pocket, but it is possible that this may need to be coupled with modification of the metal coordination environment. As mentioned, amino acids containing oxygen ligands (e.g., glutamate or aspartate) could be used to decrease metal lability because lanthanides in particular are oxophilic (21). In addition to increasing interactions with water, slowing molecular tumbling is a viable strategy to enhance relaxivity (20, 22). This could be carried out through modification of the protein surface (e.g., via PEGylation). An additional approach to decrease tumbling could be to cross-link multiple proteins together via their C-termini or surfaces. This strategy also would be useful for increasing the number of metal sites in the protein-based agent.

Concluding Remarks

The work in this dissertation provides new insight into the influence of protein structure on the chemistry of heme proteins. In addition to structural and electronic factors at the heme site, protein architectural features beyond the immediate heme coordination environment often exhibit unexpected effects on heme protein function. Here, for example, we have seen that modulating gas diffusion through H-NOX protein scaffolds has important consequences on reversible gas binding and heme oxidization. Therefore, H-NOX protein structure helps control diverse gas-mediated signaling pathways. Keeping these design principles in mind, heme proteins can be engineered to have new functions. Tailoring H-NOX protein properties through both modification of the porphyrin and protein scaffold supports new chemistry. Through this approach, we can better probe biological function and ultimately build new protein-based tools for applications such as improved cancer diagnosis and therapy.

References

1. Zhang Y, Lu M, Cheng Y, & Li Z (2010) H-NOX domains display different tunnel systems for ligand migration. *J Mol Graph Model* 28: 814-819.
2. Cohen J, Olsen KW, & Schulten K (2008) Finding gas migration pathways in proteins using implicit ligand sampling. *Methods Enzymol* 437: 439-457.
3. Konermann L, Pan J, & Liu YH (2011) Hydrogen exchange mass spectrometry for studying protein structure and dynamics. *Chem Soc Rev* 40: 1224-1234.
4. Underbakke ES (2011) Unpublished results.
5. Fraser JS, van den Bedem H, Samelson AJ, Lang PT, Holton JM, Echols N, & Alber T (2011) Accessing protein conformational ensembles using room-temperature X-ray crystallography. *Proc Natl Acad Sci U S A* 108: 16247-16252.
6. Herzik MA (2011) Unpublished results.
7. Salter MD, Nienhaus K, Nienhaus GU, Dewilde S, Moens L, Pesce A, Nardini M, Bolognesi M, & Olson JS (2008) The apolar channel in *Cerebratulus lacteus* hemoglobin is the route for O_2 entry and exit. *J Biol Chem* 283: 35689-35702.

8. Pesce A, Nardini M, Dewilde S, Capece L, Marti MA, Congia S, Salter MD, Blouin GC, Estrin DA, Ascenzi P*, et al.* (2011) Ligand migration in the apolar tunnel of *Cerebratulus lacteus* mini-hemoglobin. *J Biol Chem* 286: 5347-5358.
9. Olson JS, Soman J, & Phillips GN, Jr. (2007) Ligand pathways in myoglobin: a review of Trp cavity mutations. *IUBMB Life* 59: 552-562.
10. Schlichting I, Berendzen J, Phillips GN, Jr., & Sweet RM (1994) Crystal structure of photolysed carbonmonoxy-myoglobin. *Nature* 371: 808-812.
11. Schotte F, Lim M, Jackson TA, Smirnov AV, Soman J, Olson JS, Phillips GN, Jr., Wulff M, & Anfinrud PA (2003) Watching a protein as it functions with 150-ps time-resolved x-ray crystallography. *Science* 300: 1944-1947.
12. Cohen J, Arkhipov A, Braun R, & Schulten K (2006) Imaging the migration pathways for O_2, CO, NO, and Xe inside myoglobin. *Biophys J* 91: 1844-1857.
13. Vanderkooi JM, Wright WW, & Erecinska M (1994) Nitric oxide diffusion coefficients in solutions, proteins and membranes determined by phosphorescence. *Biochim Biophys Acta* 1207: 249-254.
14. Finikova OS, Lebedev AY, Aprelev A, Troxler T, Gao F, Garnacho C, Muro S, Hochstrasser RM, & Vinogradov SA (2008) Oxygen microscopy by two-photon-excited phosphorescence. *Chemphyschem* 9: 1673-1679.
15. Dunphy I, Vinogradov SA, & Wilson DF (2002) Oxyphor R2 and G2: phosphors for measuring oxygen by oxygen-dependent quenching of phosphorescence. *Anal Biochem* 310: 191-198.
16. Casper J & Meyer T (1983) Photochemistry of $Ru(bpy)_3^{2+}$. Solvent effects. *J Am Chem Soc* 105: 5583-5590.
17. McLaurin EJ, Greytak AB, Bawendi MG, & Nocera DG (2009) Two-photon absorbing nanocrystal sensors for ratiometric detection of oxygen. *J Am Chem Soc* 131: 12994-13001.
18. Richards-Kortum R & Sevick-Muraca E (1996) Quantitative optical spectroscopy for tissue diagnosis. *Annu Rev Phys Chem* 47: 555-606.
19. Berg K, Selbo PK, Weyergang A, Dietze A, Prasmickaite L, Bonsted A, Engesaeter BO, Angell-Petersen E, Warloe T, Frandsen N*, et al.* (2005) Porphyrin-related photosensitizers for cancer imaging and therapeutic applications. *J Microsc* 218: 133-147.
20. Datta A & Raymond KN (2009) Gd-hydroxypyridinone (HOPO)-based high-relaxivity magnetic resonance imaging (MRI) contrast agents. *Acc Chem Res* 42: 938-947.
21. Caravan P, Ellison JJ, McMurry TJ, & Lauffer RB (1999) Gadolinium(III) chelates as MRI contrast agents: Structure, dynamics, and applications. *Chem Rev* 99: 2293-2352.
22. Strauch RC, Mastarone DJ, Sukerkar PA, Song Y, Ipsaro JJ, & Meade TJ (2011) Reporter protein-targeted probes for magnetic resonance imaging. *J Am Chem Soc* 133: 16346-16349.

APPENDIX A

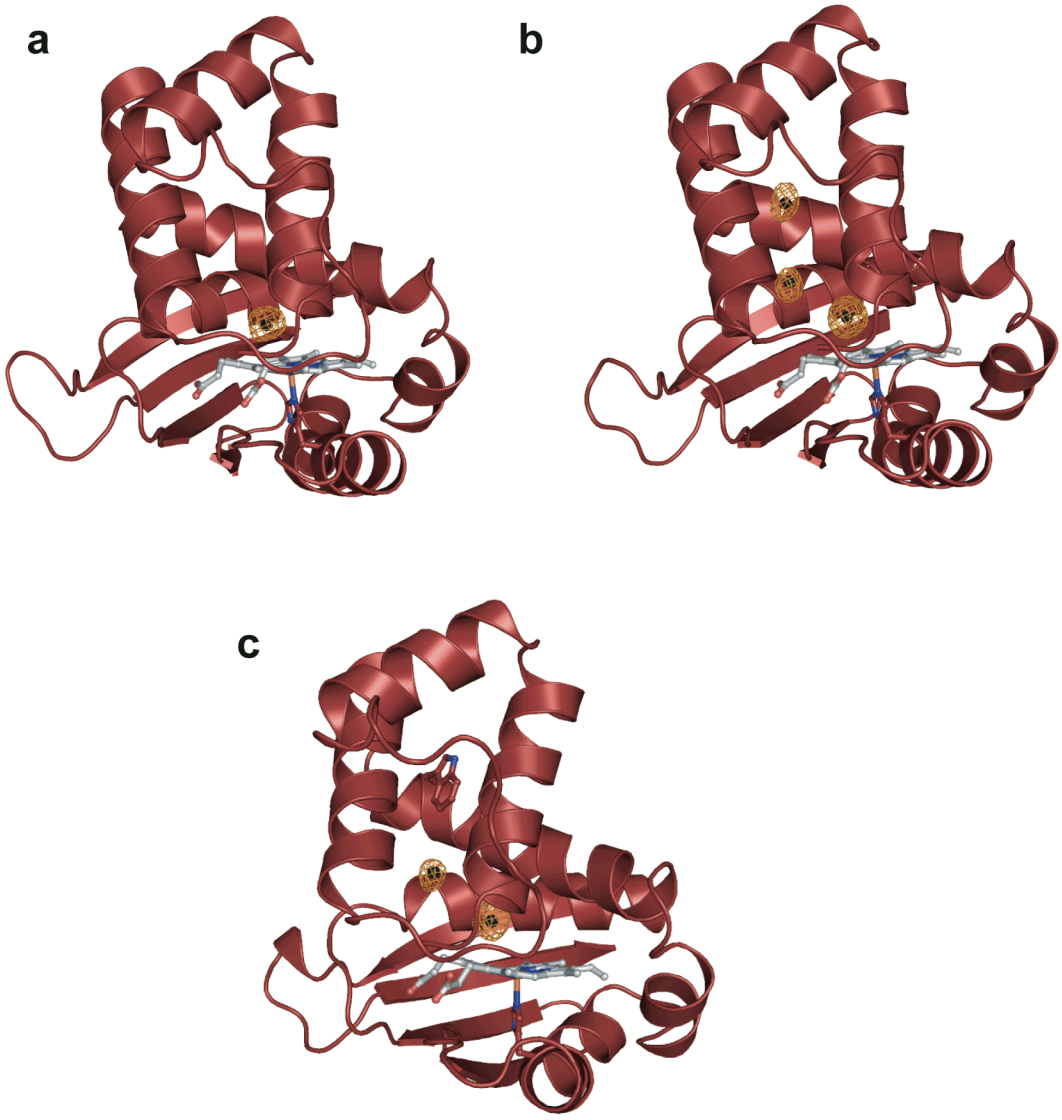

Figure A.1 Crystal structures of WT *Ns* H-NOX following pressurization with **(a)** 1 atm of xenon and **(b)** 6 atm of xenon. **(c)** Crystal structure of L66W *Ns* H-NOX following pressurization with 6 atm of xenon. Anomalous density (mesh surface) for xenon atoms is contoured at 5σ.

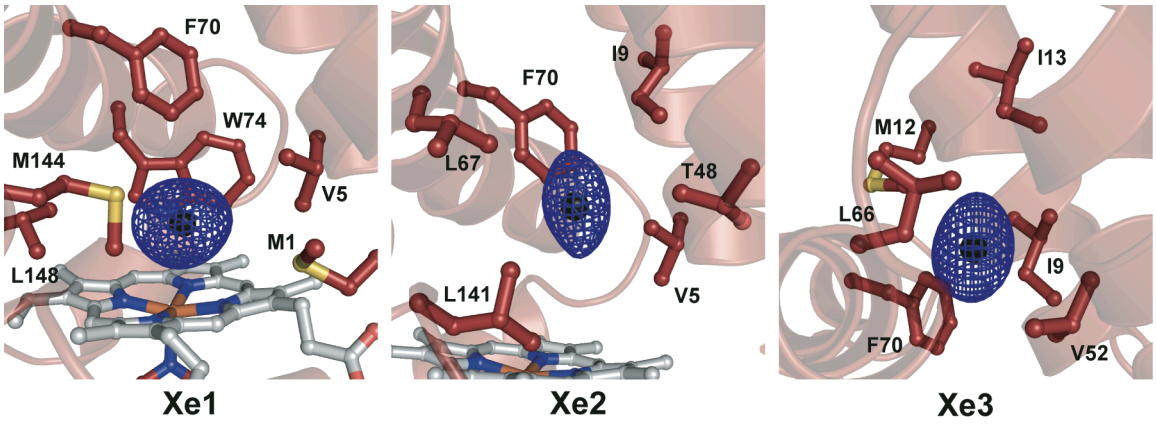

Figure A.2 Xenon binding sites in the crystal structure of WT *Ns* H-NOX pressurized with 6 atm of xenon. The Xe1, Xe2, and Xe3 sites are depicted individually with surrounding tunnel residues. $2mF_o–DF_c$ map (mesh surface) is contoured at 1σ.

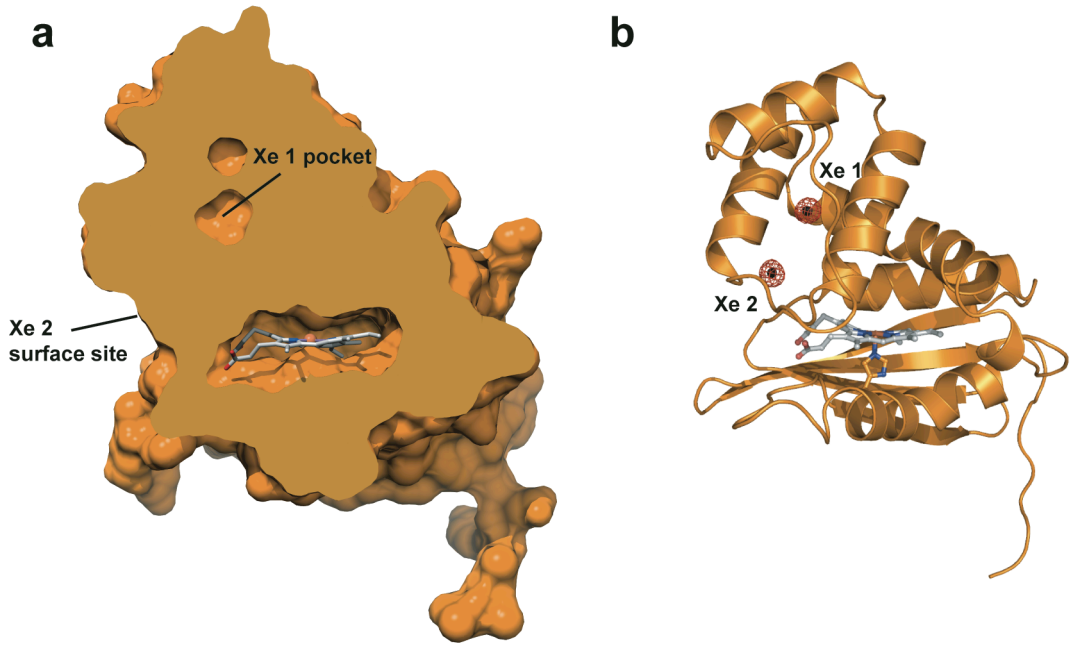

Figure A.3 Crystal structure of *Tt* H-NOX pressurized with 6 atm of xenon for 1 min. **(a)** Surface representation of *Tt* H-NOX showing a cross-sectional view with xenon binding sites labeled. **(b)** Cartoon representation of *Tt* H-NOX with anomalous density (mesh surface) for xenon atoms contoured at 5σ. See **Table A.2** for crystallography data collection and refinement statistics.

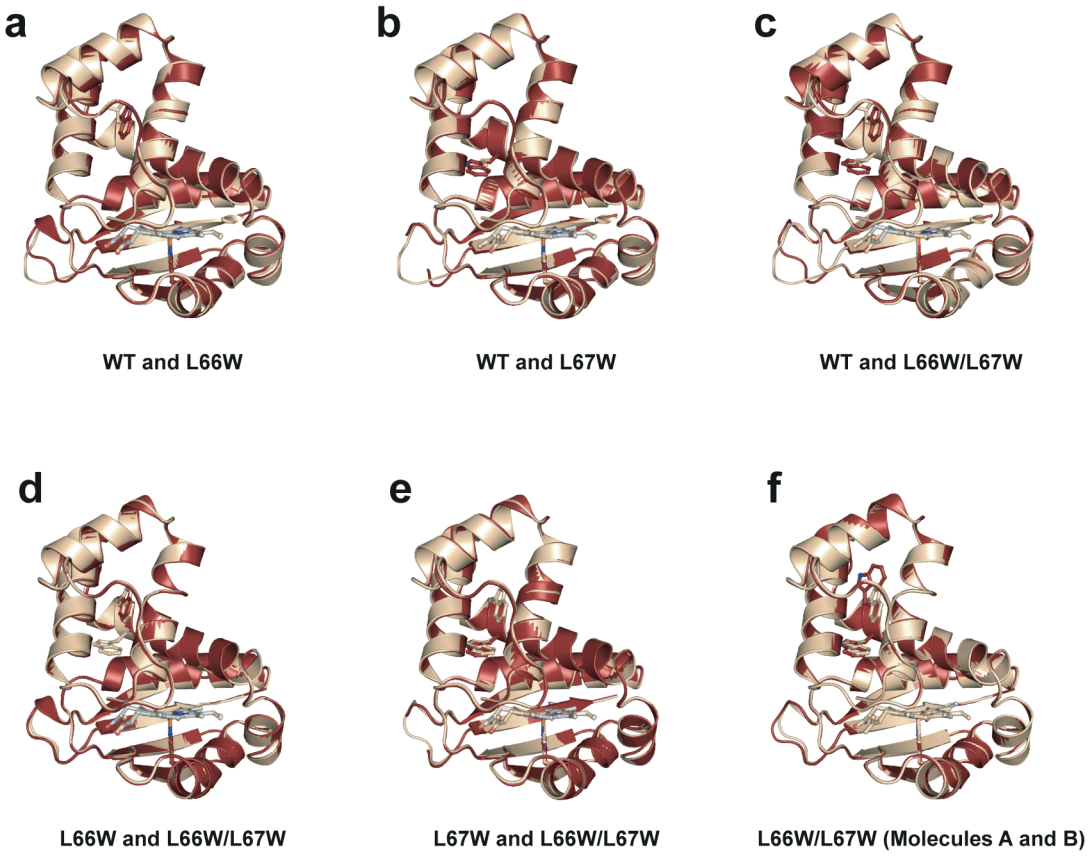

Figure A.4 Overall structural alignments for *Ns* H-NOX variants. Alignments are shown for WT *Ns* H-NOX with **(a)** L66W, **(b)** L67W, and **(c)** L66W/L67W. Alignments are also shown for L66W/L67W with **(d)** L66W, **(e)** L67W, and **(f)** L66W/L67W (molecule B). Molecule A was utilized for all alignments except where noted.

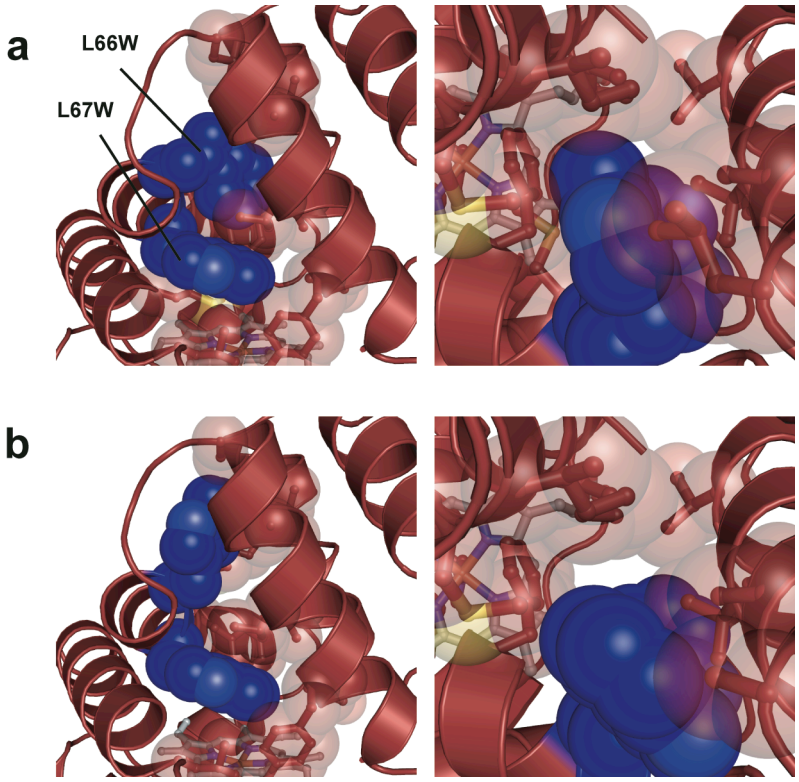

Figure A.5 L66W rotamers in the L66W/L67W double mutant crystal structure. **(a)** Molecule A from **(left)** "side" and **(right)** "top-down" views. **(b)** Molecule B from **(left)** "side" and **(right)** "top-down" views. The tryptophan side chains in molecule A of the double mutant structure are positioned similarly to the side chains in the L66W and L67W single mutant structures. The alternate L66W rotamer in molecule B appears to not be as effective in sterically blocking tunnel 1 (see "top-down" view). Molecules A and B superimpose to a high degree overall (see **Figure A.4F**).

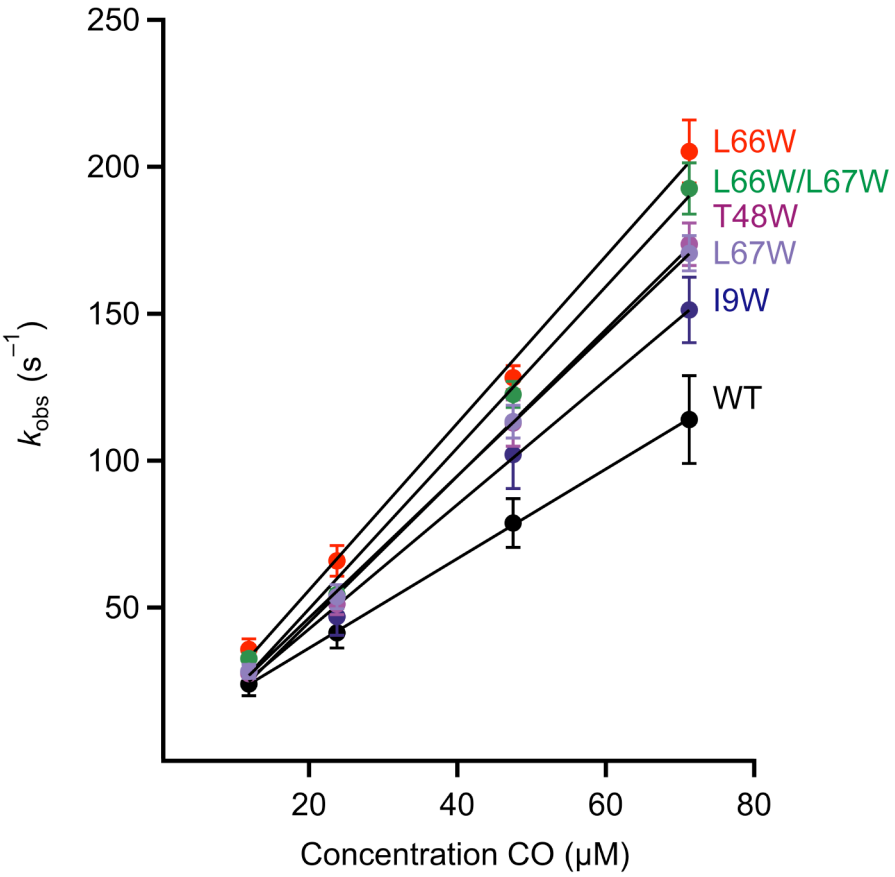

Figure A.6 Observed CO binding rates (k_{obs}) for *Ns* H-NOX variants determined with stopped flow spectroscopy. Final CO concentrations of 11.9, 23.8, 47.5, and 71.3 μM were utilized. N = 3-5. Error bars represent the standard deviation.

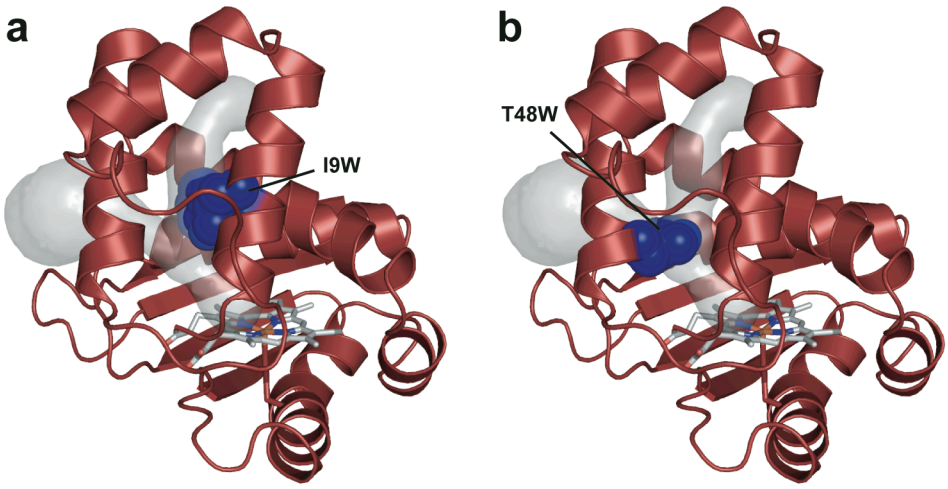

Figure S.7 *In silico* representations of **(a)** I9W and **(b)** T48W. Mutagenesis and modeling of allowed rotamers was carried out in Coot. The most favorable rotamer for each side chain is shown. The tunnel network was modeled using CAVER on the WT *Ns* H-NOX structure with the heme iron as the point of origin.

Table A.1 WT *Ns* H-NOX crystallography data collection and refinement statistics.

	WT *Ns* H-NOX		
	Native	**1 atm Xe**	**6 atm Xe**
Wavelength (Å)	0.97	1.40	1.40
Space group	$P2_13$	$P2_13$	$P2_13$
Cell dimensions			
$a = b = c$ (Å)	123.7	124.4	123.9
$\alpha = \beta = \gamma$ (°)	90	90	90
Resolution (Å)	50.00-2.13 (2.17-2.13)	50.00-2.59 (2.63-2.59)	50.00-2.27 (2.31-2.27)
Redundancy	5.6 (5.6)	6.3 (6.1)	6.3 (5.9)
Completeness[a] (%)	99.9 (100.0)	99.5 (100.0)	99.5 (97.9)
R_{sym} (%)	6.5 (63.4)	7.3 (61.6)	5.4 (28.1)
I / σ	23.6 (3.2)	20.4 (2.78)	30.2 (5.76)
No. of reflections	38528	40549	55256
R_{work}/R_{free} (%)	16.4/20.0	17.7/21.4	16.2/19.0
Molecules in AU	2	2	2
No. atoms			
Protein[b]	2886	2819	2779
Heme	96	96	96
Xenon	0	2	6
Solvent	224	20	90
Rms deviation			
Bond lengths (Å)	0.010	0.021	0.010
Bond angles (°)	1.233	1.881	1.267
Xenon Occupancy			
Molecule A		0.3[c]	0.6,[c] 0.3,[d] 0.4[e]
Molecule B		0.3[c]	0.7,[c] 0.4,[d] 0.5[e]

[a] Overall completeness. [b] Non-hydrogen atoms. [c] Xe1. [d] Xe2. [e] Xe3.

Table A.2 Mutant *Ns* H-NOX crystallography data collection and refinement statistics.

	L66W		**L67W**	**L66W/ L67W**
	Native	**6 atm Xe**	**Native**	**Native**
Wavelength (Å)	0.97	1.40	0.97	0.97
Space group	$P2_13$	$P2_13$	$P2_13$	$P2_13$
Cell dimensions				
$a = b = c$ (Å)	123.2	123.3	123.2	123.1
$\alpha = \beta = \gamma$ (°)	90	90	90	90
Resolution (Å)	50.00-1.96 (1.99-1.96)	50.00-1.99 (2.02-1.99)	50.00-1.94 (1.97-1.94)	50.00-1.90 (1.93-1.90)
Redundancy	5.5 (5.6)	6.8 (6.5)	6.8 (6.8)	6.8 (6.8)
Completeness[a] (%)	100.0 (100.0)	100.0 (100.0)	100.0 (100.0)	100.0 (100.0)
R_{sym} (%)	4.9 (64.6)	5.6 (68.3)	5.5 (61.5)	6.2 (62.5)
I / σ	29.9 (2.28)	28.7 (2.91)	29.8 (3.70)	28.2 (3.32)
No. of reflections	43497	79661	48228	51187
R_{work}/R_{free} (%)	16.3/18.7	15.6/17.3	16.5/18.8	16.0/18.3
Molecules in AU	2	2	2	2
No. atoms				
Protein[b]	2890	2875	3038	3022
Heme	96	96	96	96
Xenon	0	4	0	0
Solvent	205	191	247	262
Rms deviation				
Bond lengths (Å)	0.009	0.009	0.009	0.018
Bond angles (°)	1.290	1.227	1.251	1.661
Xenon Occupancy				
Molecule A		0.3,[c] 0.1[d]		
Molecule B		0.4,[c] 0.1[d]		

[a] Overall completeness. [b] Non-hydrogen atoms. [c] Xe1. [d] Xe2.

Table A.3 *Tt* H-NOX crystallography data collection and refinement statistics.

	WT *Tt* H-NOX	
	Native	**6 atm Xe**
Wavelength (Å)	0.977	1.23
Space group	$P2_12_12$	$P2_12_12$
Cell dimensions		
a, *b*, *c* (Å)	80.5, 130.7, 42.7	80.1, 130.2, 42.8
$\alpha = \beta = \gamma$ (°)	90	90
Resolution (Å)	50.00-1.74 (1.77-1.74)	50.00-2.03 (2.07-2.03)
Redundancy	6.6 (6.3)	4.2 (4.0)
Completeness[a] (%)	95.4 (89.5)	99.8 (99.1)
R_{sym} (%)	6.7 (55.1)	7.9 (62.4)
I / σ	23.39 (2.43)	17.11 (2.16)
No. of reflections	44302	52372
R_{work}/R_{free} (%)	20.2/22.9	17.9/21.9
Molecules in AU	2	2
No. atoms		
Protein[b]	3059	3003
Heme	96	96
O_2	2	2
Xenon	0	4
Solvent	111	145
Rms deviation		
Bond lengths (Å)	0.008	0.017
Bond angles (°)	0.992	1.482
Xenon Occupancy		
Molecule A		0.8,[c] 0.5[d]
Molecule B		0.7,[c] 0.4[d]

[a] Overall completeness. [b] Non-hydrogen atoms. [c] Xe1. [d] Xe2.

Table A.4 UV-visible spectral features of *Ns* H-NOX variants.

	Absorbance (nm)				
Protein	**Unligated**	**Fe^{II}–CO**	**Fe^{II}–NO**	**Fe^{II}–O_2**	***Ref.*[b]**
***Ns* H-NOX** (Wild-type)	431 558	424 539 565	399[a] / 417 545 573	n.o	
L67W	431 558	423 541 566	399[a] / 417 544 573	n.o.	
L66W	430 558	424 541 566	399[a] / 417 544 573	n.o.	
L66W/L67W	431 560	423 541 569	399[a] / 417 544 573	n.o.	
T48W	430 558	423 539 567	399[a] / 418 544 573	n.o.	
I9W	431 557	424 538 566	399[a] / 417 544 574	n.o.	
***Tt* H-NOX**	431 565	424 544 565	420 547 575	416 556 591	(44)
sGC	431 555	423 541 567	398 537 572	n.o.	(55)

[a] Shoulder. [b] This work unless otherwise noted. n.o. = not observed.

APPENDIX B

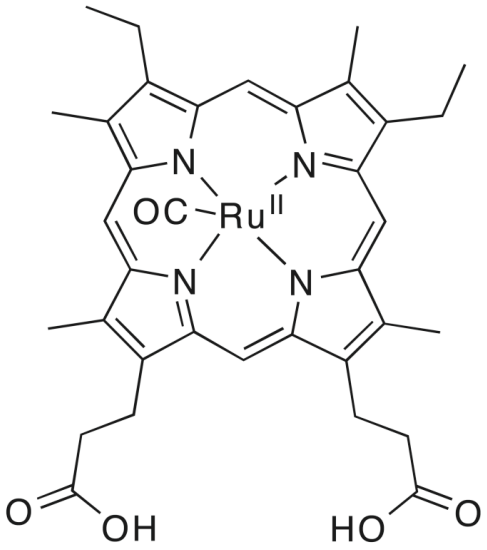

Figure B.1 Chemical structure of ruthenium(II) CO mesoporphyrin IX (RuMP).

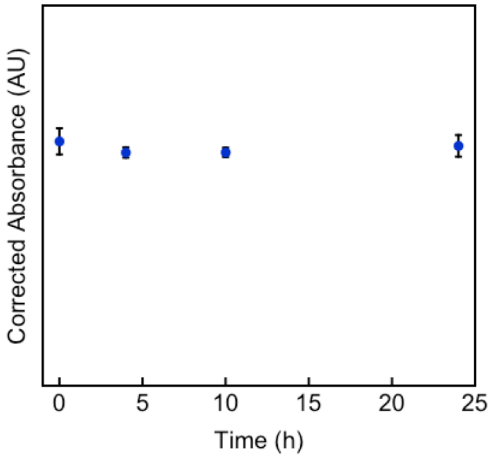

Figure B.2 Stability of Ru *Tt* H-NOX in mouse plasma at 37 ^{o}C. Soret absorbance of Ru *Tt* H-NOX at 400 nm (corrected for plasma background) is plotted versus time. N = 3 using independently prepared samples.

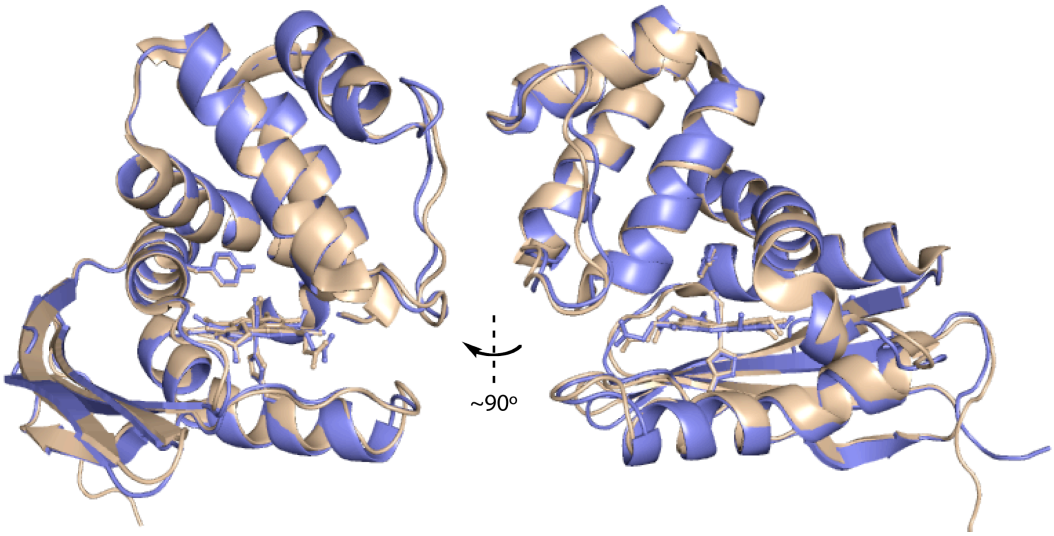

Figure B.3 Overall alignment showing secondary structural elements of Ru *Tt* H-NOX (—) and heme-bound *Tt* H-NOX (molecule B, PDB 1U55) (—).

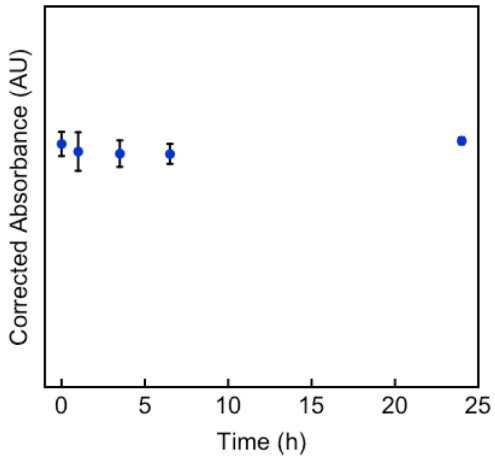

Figure B.4 Stability of Pd *Tt* H-NOX in mouse plasma at 37 ^{o}C. Soret absorbance of Pd *Tt* H-NOX at 393 nm (corrected for plasma background) is plotted versus time. N = 3 using independently prepared samples.

Table B.1 RuMP stochiometry for Ru *Tt* H-NOX and Ru Mb.

Ru Protein	HPLC		UV-vis	
	A280	Bradford	A280	Bradford
Tt H-NOX	1.03 ± 0.04	1.17 ± 0.06	0.88 ± 0.01	1.13 ± 0.13
Mouse Mb	0.67 ± 0.01	0.85 ± 0.05	0.61 ± 0.01	0.96 ± 0.12

Table B.2 Ru *Tt* H-NOX crystallography data collection and refinement statistics.

	Ru *Tt* H-NOX
Space group	$P6_122$
Cell dimensions	
a, *b*, *c* (Å)	61.183, 61.183, 245.116
α, β, γ (°)	90, 90, 120
Resolution (Å)	50.00-2.00 (2.07-2.00)
Redundancy[a]	19.4 (19.4)
Completeness (%)[a]	99.0 (96.0)
R_{merge} (%)[a]	7.6 (30.7)
I / σ[a]	26.7 (10.1)
No. of reflections	19295
R_{work}/R_{free}[b] (%)	20.4/22.5
Molecules in AU	1
No. atoms	
Protein	1504
Porphyrin	43
Ru	1
CO	1
Solvent	97
Rms deviation	
Bond lengths (Å)	0.013
Bond angles (°)	1.002

[a] The values in parentheses are for the highest resolution shells. [b] R_{free} is calculated for a randomly chosen 5% of reflections.

APPENDIX C

Table C.1 RuMP stochiometry of purified Ru β1(1-194) and Ru β1(1-385)

Protein	HPLC (eq.)	UV-vis (eq.)
Ru β1(1-194)	0.89 ± 0.03	0.93 ± 0.02
Ru β1(1-385)	0.78 ± 0.01	0.88 ± 0.03

APPENDIX D

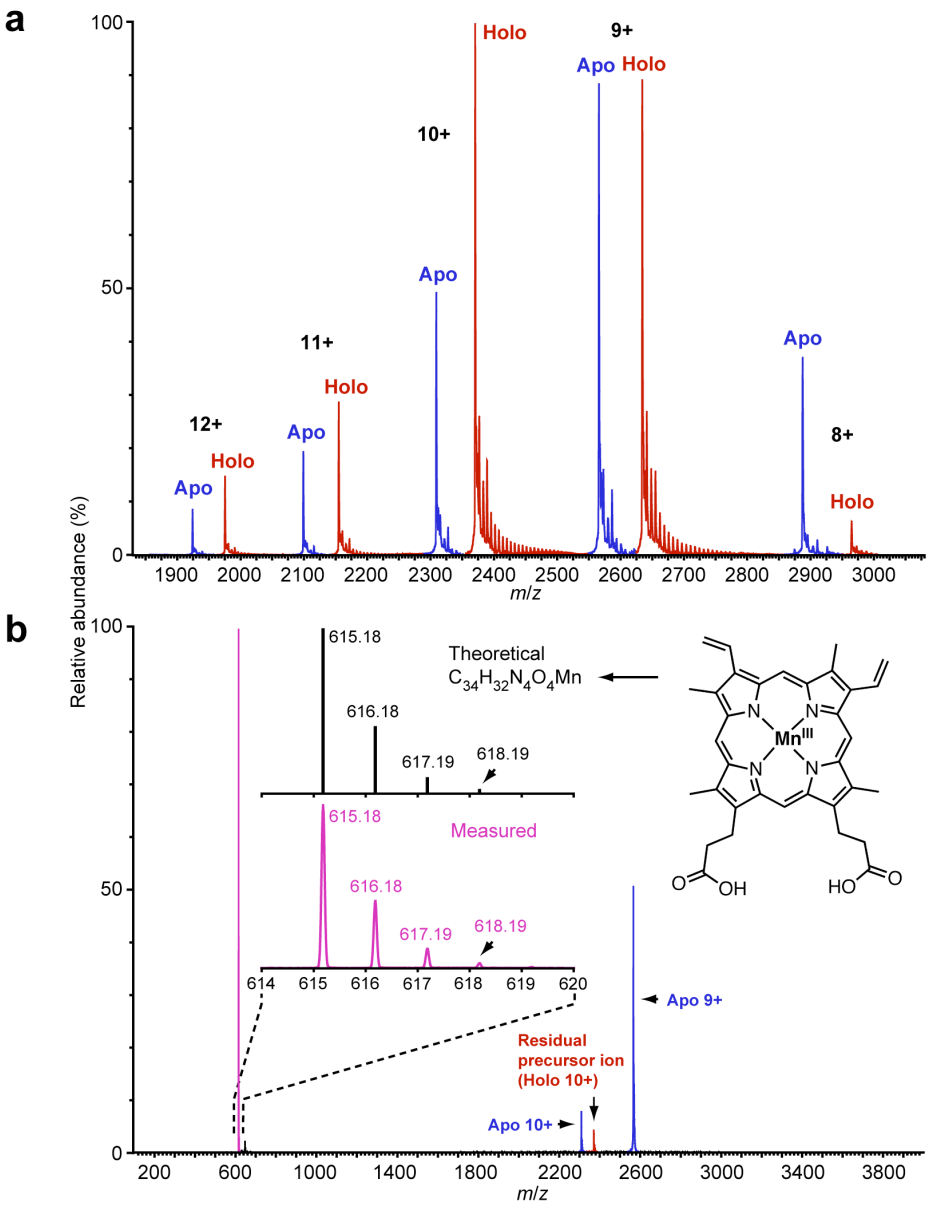

Figure D.1 (a) Native nanoelectrospray ionization mass spectrum of Mn *Tt* H-NOX His_6, exhibiting charge states 8+ to 12+ of the apo (—) and holo (—) forms of the protein. **(b)** Tandem mass (MS/MS) spectrum resulting from collisionally activated dissociation (CAD) of the precursor ion at m/z = 2370.5, which corresponds to the $[M + 10H]^{10+}$ ion of the holo protein. The inset in **(b)** compares the measured isotopic distribution of the singly charged fragment ion at m/z = 615.18 with the theoretical isotopic distribution of the Mn-porphyrin ligand, calculated from the natural abundances of the isotopes.

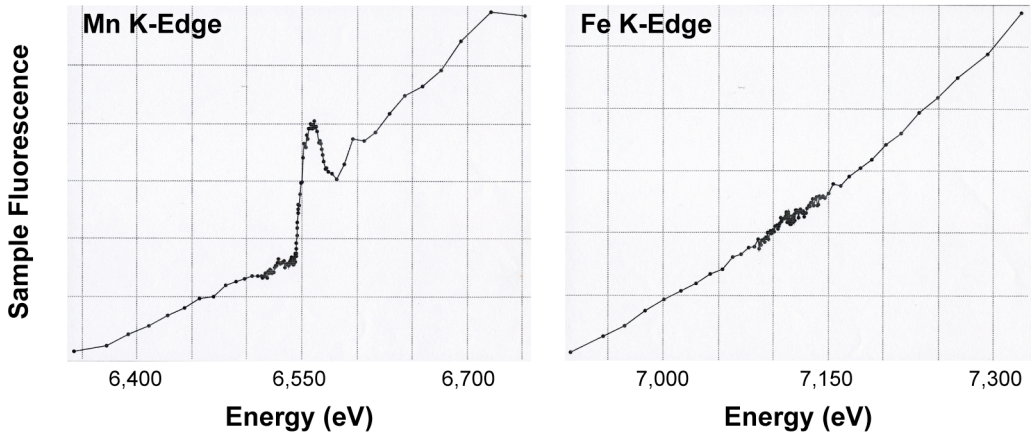

Figure D.2 X-ray absorption of a Mn *Tt* H-NOX crystal at 100 K scanning at the Mn and Fe K-edges to verify specific metal incorporation.

Table D.1 UV-visible spectral features of the protein complexes.

Protein	Absorbance λ_{abs} (nm)
Fe^{III} Mb	**408**[a]
	505
	630
Fe^{III} *Tt* H-NOX	**413**
	551
	588
Mn^{III} *Tt* H-NOX	**376**
	474
	560
	~595
Mn^{II} *Tt* H-NOX	**440**
	564
	598
Gd^{III} *Tt* H-NOX	**419**
	506
	544
	584
	627

[a] Bold indicates the major peak.

Table D.2 Mn *Tt* H-NOX crystallography data collection.

	Mn *Tt* H-NOX[a]
Space group	C_2
Cell dimensions	
a, *b*, *c* (Å)	119.9, 45.3, 95.6
α, β, γ (^{o})	90.0, 122.9, 90.0
Resolution (Å)	50 – 2.15 (2.19 – 2.15)
Redundancy	2.8 (2.8)
Completeness (%)	99.3 (99.9)
R_{sym} (%)	5.4 (38.5)
I / σ	22.4 (3.0)
No. of reflections	24146 (1207)
Molecules in AU	2
Mn	2

[a] Numbers in parentheses refer to the highest resolution bin.